CFD Analysis of Fluid, Heat, and Impurity Flows in DUNE FAR Detector to Address Additional Design Considerations

April 6, 2017

Co-PIs: Gregory J. Michna
gregory.michna@sdstate.edu
Stephen P. Gent
stephen.gent@sdstate.edu

Graduate Research Assistant: Aaron Propst
aaron.propst@jacks.sdstate.edu

Mechanical Engineering Department
South Dakota State University

ABSTRACT

The purpose of this manuscript is to provide a comprehensive overview of the computational fluid dynamics (CFD) modeling efforts being conducted by the Department of Mechanical Engineering at South Dakota State University (SDSU) pertaining to the Deep Underground Neutrino Experiment (DUNE). The goal of these efforts is to determine the effects of the placement of pump suction and discharge ports in the detector on the flow patterns, thermal profiles, impurity concentration, and electron lifetime in the liquid argon around and through the field cage. This information will be used to guide the design of the long-range detectors as well as understand how they are expected to perform.

To date, the SDSU team has conducted CFD analyses of the following detector designs: 1) the 35 Ton Cryostat, which was validated with the CFD modeling efforts by Erik Voirin at Fermilab, 2) the LBNF Cryostat V1 design, which included the full model and symmetric half model, and 3) the latest LBNF Cryostat design, which has a total of 12 pump discharge ports evenly spaced along the bottom corner of each side of the cryostat and a total of seven pump suction ports evenly spaced along the bottom centerline of the cryostat running lengthwise. The SDSU team was able to validate their modeling methodology by comparing the 35 Ton simulation results with the Fermilab CFD results and available experimental data . In addition, the SDSU team has shown that the full model results of the LBNF are generally symmetric in nature and moving forward with symmetric half models is appropriate. Also, the latest design consideration provides more uniform flows and impurity concentrations within the detector.

The modeling efforts and results this far provide a foundation for analyzing additional design considerations for the LBNF detector. These considerations include the assessment of partial pump shutdown scenarios and evaluating the liquid/vapor interface in the ullage, among others.

TABLE OF CONTENTS

ABSTRACT ii
BACKGROUND 1
35 TON CRYOSTAT MODELING APPROACH AND VALIDATION 3
Geometry Cases 3
Boundary Conditions (Operational Parameters) 5
Using Porous Membranes to Simulate Field Cage 6
Physics Continua 7
Computational Mesh Settings 8
Convergence Criteria 10
Passive Scalar Calculations 10
Impurity Levels 10
Electron Lifetime 10
35 TON CRYOSTAT SIMULATION RESULTS 12
Bottom (Original) Pump Discharge Location 12
Top Pump Discharge Location 17
DUNE LBNF MODELING APPROACH 24
Geometry Cases 24
Common Geometry Features: 24
V1: 25
Latest Configuration: 26
Boundary Conditions 27
Common Conditions: 27
V1: 29
Latest Configuration: 29
Using Porous Membranes to Simulate APA and Field Cage Planes 29
APA Plane 29
Field Cage Plane 34
Physics Continua 35
Mesh Settings 36
New Mesh Settings for Latest Design 37

Convergence Criteria 39
Passive Scalar Calculations 40
DUNE LBNF SIMULATION RESULTS 41
Comparison of New Meshes for Latest Design 42
Impurity Scaled with Velocity Vectors 42
Temperature with Velocity Vectors 57
Streamlines 71
Latest Design with Electronics Turned Off 74
Impurity and Temperature with Velocity Vectors 75
Streamlines 87
Latest Design with 50% LAr Flow Rate (NOT UPDATED) 87
Streamlines 103
Impurity Level Statistics 103
Average Volume Temperature Comparison 104
REMARKS TO DATE 106
REFERENCES 108
APPENDIX A I
APPENDIX B II

LIST OF FIGURES

Figure 1: 35 Ton geometry view showing inlet locations. 4
Figure 2: 35 Ton geometry view showing outlet and field cage. 5
Figure 3: Fermilab simulation of 12.5% open slot representative of field cage geometry. 6
Figure 4: Simulation geometry used to find inertial resistance coefficient. 7
Figure 5: 35 Ton mesh section view through pump suction (outlet). 9
Figure 6: Fermilab simulation results for electron lifetime and velocity fields at the mid-plane of the 35 Ton prototype detector. 12
Figure 7: SDSU simulation results for electron lifetime and velocity fields at the mid-plane of the 35 Ton prototype detector. 13
Figure 8: Locations of purity monitors in the 35 Ton cryostat. 14
Figure 9: Comparison of experimental electron lifetime measurement at the purity monitor locations. 15
Figure 10: Streamline view from SDSU simulation. 16
Figure 11: Streamline view from SDSU simulation. 17
Figure 12: Fermilab electron lifetime results for 35 Ton cryostat with top inlet location. 18
Figure 13: SDSU electron lifetime results for 35 Ton cryostat with top inlet location. 19
Figure 14: Streamline view from Fermilab simulation of top inlet at an angle of 45 degrees. 20
Figure 15: Streamline view from SDSU simulation of top inlet at an angle of 45 degrees. 21
Figure 16: Additional streamline view from SDSU simulation of top inlet at an angle of 45 degrees. 22
Figure 17: Electron Lifetime vs Elevation with Top Inlet at 45 Degrees. 23
Figure 18: Cross section showing APA, CPA, and Field Cage planes. 25
Figure 19: Cross Section showing Field Cage planes. 25
Figure 20: Cross section showing inlet and outlet locations in V1 configuration. 26
Figure 21: Cross section showing inlet (green) and outlet (red) locations in latest configuration. 26
Figure 22: Geometry view with electronic surfaces highlighted. 28
Figure 23: APA plane layer geometry view used in pressure drop simulation. 30
Figure 24: Full View of APA pressure drop simulation geometry. 31
Figure 25: Plot of pressure drop vs. velocity, with coefficients used to determine resistance values. 32
Figure 26: Geometry view of APA resistance coefficients verification simulation. 33
Figure 27: Plot of pressure drop vs. velocity, with results of the coefficient verification simulation (red). 34
Figure 28: Field cage plane geometry for pressure drop simulation. 35
Figure 29: Mesh cross section of full LBNF simulation. 36
Figure 30: Mesh cross section of CPA and field cage planes. 37
Figure 31: Mesh cross section views of original and new polyhedral meshes, respectively. 38
Figure 32: Mesh cross section views of new trimmed (hexahedral) mesh. 39
Figure 33. Impurity and velocity vectors at x = 0.1 m for latest design with original poly, new poly, and new trimmed meshes. 42
Figure 34. Impurity and velocity vectors at x = 1 m for latest design with original poly, new poly, and new trimmed meshes. 43

Figure 35. Impurity and velocity vectors at x = 2 m for latest design with original poly, new poly, and new trimmed meshes. 44
Figure 36. Impurity and velocity vectors at x = 3 m for latest design with original poly, new poly, and new trimmed meshes. 45
Figure 37. Impurity and velocity vectors at x = 4 m for latest design with original poly, new poly, and new trimmed meshes. 46
Figure 38. Impurity and velocity vectors at x = 5 m for latest design with original poly, new poly, and new trimmed meshes. 47
Figure 39. Impurity and velocity vectors at x = 6 m for latest design with original poly, new poly, and new trimmed meshes. 48
Figure 40. Impurity and velocity vectors at x = 7 m for latest design with original poly, new poly, and new trimmed meshes. 49
Figure 41. Impurity and velocity vectors at x = 7.4 m for latest design with original poly, new poly, and new trimmed meshes. 50
Figure 42. Impurity and velocity vectors at z = -25 m for latest design with original poly, new poly, and new trimmed meshes. 51
Figure 43. Impurity and velocity vectors at z = -20 m for latest design with original poly, new poly, and new trimmed meshes. 52
Figure 44. Impurity and velocity vectors at z = 0.0 m for latest design with original poly, new poly, and new trimmed meshes. 53
Figure 45. Impurity and velocity vectors at z = 10 m for latest design with original poly, new poly, and new trimmed meshes. 54
Figure 46. Impurity and velocity vectors at z = 20 m for latest design with original poly, new poly, and new trimmed meshes. 55
Figure 47. Impurity and velocity vectors at z = 30.5 m for latest design with original poly, new poly, and new trimmed meshes. 56
Figure 48. Temperature and velocity vectors at x = 0.1 m for latest design with original poly, new poly, and new trimmed meshes. 57
Figure 49. Temperature and velocity vectors at x = 1 m for latest design with original poly, new poly, and new trimmed meshes. 58
Figure 50. Temperature and velocity vectors at x = 2 m for latest design with original poly, new poly, and new trimmed meshes. 59
Figure 51. Temperature and velocity vectors at x = 3 m for latest design with original poly, new poly, and new trimmed meshes. 60
Figure 52. Temperature and velocity vectors at x = 4 m for latest design with original poly, new poly, and new trimmed meshes. 61
Figure 53. Temperature and velocity vectors at x = 5 m for latest design with original poly, new poly, and new trimmed meshes. 62
Figure 54. Temperature and velocity vectors at x = 6 m for latest design with original poly, new poly, and new trimmed meshes. 63
Figure 55. Temperature and velocity vectors at x = 7 m for latest design with original poly, new poly, and new trimmed meshes. 64
Figure 56. Temperature and velocity vectors at x = 7.4 m for latest design with original poly, new poly, and new trimmed meshes. 65
Figure 57. Temperature and velocity vectors at z = -25 m for latest design with original poly, new poly, and new trimmed meshes. 66

Figure 58. Temperature and velocity vectors at z = -20 m for latest design with original poly, new poly, and new trimmed meshes. 67
Figure 59. Temperature and velocity vectors at z = 0.0 m for latest design with original poly, new poly, and new trimmed meshes. 68
Figure 60. Temperature and velocity vectors at z = 10 m for latest design with original poly, new poly, and new trimmed meshes. 69
Figure 61. Temperature and velocity vectors at z = 20 m for latest design with original poly, new poly, and new trimmed meshes. 70
Figure 62. Temperature and velocity vectors at z = 30.5 m for latest design with original poly, new poly, and new trimmed meshes. 71
Figure 63. Streamline view 1 for latest design with original polyhedral mesh. 72
Figure 64. Streamline view 1 for latest design with new polyhedral mesh. 72
Figure 65. Streamline view 1 for latest design with new trimmed mesh. 73
Figure 66. Streamline view 2 for latest design with original polyhedral mesh. 73
Figure 67. Streamline view 2 for latest design with new polyhedral mesh. 74
Figure 68. Streamline view 2 for latest design with new trimmed mesh. 74
Figure 69. Plot of average temperature with the electronics shut off at 100,000 iterations. 74
Figure 70. Impurity and temperature with velocity vectors at x = 0.1 m for latest design with electronics turned off (trimmed mesh). 75
Figure 71. Impurity and temperature with velocity vectors at x = 1 m for latest design with electronics turned off (trimmed mesh). 76
Figure 72. Impurity and temperature with velocity vectors at x = 2 m for latest design with electronics turned off (trimmed mesh). 77
Figure 73. Impurity and temperature with velocity vectors at x = 3 m for latest design with electronics turned off (trimmed mesh). 78
Figure 74. Impurity and temperature with velocity vectors at x = 4 m for latest design with electronics turned off (trimmed mesh). 79
Figure 75. Impurity and temperature with velocity vectors at x = 5 m for latest design with electronics turned off (trimmed mesh). 80
Figure 76. Impurity and temperature with velocity vectors at x = 6 m for latest design with electronics turned off (trimmed mesh). 81
Figure 77. Impurity and temperature with velocity vectors at x = 7 m for latest design with electronics turned off (trimmed mesh). 82
Figure 78. Impurity and temperature with velocity vectors at x = 7.4 m for latest design with electronics turned off (trimmed mesh). 83
Figure 79. Impurity and temperature with velocity vectors at z = -25 m for latest design with electronics turned off (trimmed mesh). 84
Figure 80. Impurity and temperature with velocity vectors at z = -20 m for latest design with electronics turned off (trimmed mesh). 84
Figure 81. Impurity and temperature with velocity vectors at z = 0.0 m for latest design with electronics turned off (trimmed mesh). 85
Figure 82. Impurity and temperature with velocity vectors at z = 10 m for latest design with electronics turned off (trimmed mesh). 85
Figure 83. Impurity and temperature with velocity vectors at z = 20 m for latest design with electronics turned off (trimmed mesh). 86

Figure 84. Impurity and temperature with velocity vectors at z = 30.5 m for latest design with electronics turned off (trimmed mesh). 86
Figure 85. Streamline view 1 for latest design with electronics turned off. 87
Figure 86. Streamline view 2 for latest design with electronics turned off. 87
Figure 87. Impurity and temperature with velocity vectors at x = 0.1 m for latest design with 50% LAr flow rate (trimmed mesh). 88
Figure 88. Impurity and temperature with velocity vectors at x = 1 m for latest design with 50% LAr flow rate (trimmed mesh). 89
Figure 89. Impurity and temperature with velocity vectors at x = 2 m for latest design with 50% LAr flow rate (trimmed mesh). 90
Figure 90. Impurity and temperature with velocity vectors at x = 3 m for latest design with 50% LAr flow rate (trimmed mesh). 91
Figure 91. Impurity and temperature with velocity vectors at x = 4 m for latest design with 50% LAr flow rate (trimmed mesh). 92
Figure 92. Impurity and temperature with velocity vectors at x = 5 m for latest design with 50% LAr flow rate (trimmed mesh). 93
Figure 93. Impurity and temperature with velocity vectors at x = 6 m for latest design with 50% LAr flow rate (trimmed mesh). 94
Figure 94. Impurity and temperature with velocity vectors at x = 7 m for latest design with 50% LAr flow rate (trimmed mesh). 95
Figure 95. Impurity and temperature with velocity vectors at x = 7.4 m for latest design with 50% LAr flow rate (trimmed mesh). 96
Figure 96. Impurity and temperature with velocity vectors at z = -25 m for latest design with 50% LAr flow rate (trimmed mesh). 97
Figure 97. Impurity and temperature with velocity vectors at z = -20 m for latest design with 50% LAr flow rate (trimmed mesh). 98
Figure 98. Impurity and temperature with velocity vectors at z = 0.0 m for latest design with 50% LAr flow rate (trimmed mesh). 99
Figure 99. Impurity and temperature with velocity vectors at z = 10 m for latest design with 50% LAr flow rate (trimmed mesh). 100
Figure 100. Impurity and temperature with velocity vectors at z = 20 m for latest design with 50% LAr flow rate (trimmed mesh). 101
Figure 101. Impurity and temperature with velocity vectors at z = 30.5 m for latest design with 50% LAr flow rate (trimmed mesh). 102
Figure 102. Streamline view 1 for latest design with half flow rate. 103
Figure 103. Streamline view 2 for latest design with half flow rate. 103
Figure 104. Average concentration at current solution. 104
Figure 105. Plot of average volume temperature for each mesh and scenario. 105

LIST OF TABLES

Table 1: 35 Ton simulation boundary conditions. 5
Table 2: 35 Ton simulation physics continua. 7
Table 3: LAr properties assumed in simulations. 8
Table 4: List of inlet and outlet locations of the latest configuration. 27
Table 5: Description of LBNF boundary conditions. 27
Table 6: Number of pumps running in each simulation. 28
Table 7: Physics models used in solid continua..... 35
Table 8: Stainless steel 302 properties used in solid continua..... 35
Table 9. Impurity ranges for each mesh and operating condition..... 103
Table 10. Impurity ranges with half initial concentration for each mesh and operating condition. 104

BACKGROUND

The Deep Underground Neutrino Experiment (DUNE) is an international experiment that is focused on neutrino science and proton decay study. DUNE seeks to answer questions about the nature of matter, the origins and evolution of the universe, and black hole formations, to name a few.

This project consists of placing near- and far-range detectors in the path of the world's most intense neutrino beam, which originates at the Fermi National Accelerator Laboratory in Batavia, Illinois. The focus of this paper is the long-range detector, which is to be located approximately a mile underground at the Sanford Underground Research Facility in Lead, South Dakota. The long-range detectors will contain 70,000 tons of liquid argon and will be the largest neutrino detectors in the world. As the neutrinos interact with the argon at a temperature of 87 K, they create a shower of particles and light, which will be detected by arrays of electronics within the cryostat.

The design goal of the detector itself is to operate without incident, e. g., requiring evacuation of the liquid argon, replacing electronic arrays, etc., for up to 30 years. The cryostat is designed to work alongside a cryogenics facility where the liquid argon will be filtered and circulated through the cryostat. As the liquid argon flows within the detector, it interacts with the electronic arrays and the ullage interface at the top of the detector. These interactions cause the argon to lose its purity, thus affecting the electron lifetime.

One of the primary design considerations of the DUNE long range detector is the placement of the pump discharge and suction ports. The locations in which the liquid argon is supplied to and removed from the detector, as well as the flow rates, affect the flow profiles, residence time, and ultimately the electron lifetime throughout the detector.

In an effort to better understand the fluid mechanics, heat transfer, and impurity concentrations within the detector, computational fluid dynamics (CFD) simulation tools have been employed to predict what is occurring within the detector. CFD is a finite volume computational solver that uses numerical approaches to solve viscous flows. The argon flows within the DUNE long range

detector are going to be influenced primarily through thermal gradients, i.e., fluid buoyancy, while locations near pump suctions and discharges will be influenced by the argon flows entering/exiting these respective locations. Fermi Lab has conducted CFD analyses of the proposed long range detectors in-house with Erik Voirin's expertise.

The fluid, heat, and impurity flows of the liquid argon in the LBNF cryostat have been analyzed by Erik Voirin (FNAL) for different configurations of pumps using computational fluid dynamics (CFD) simulations.

The simulations results were reviewed by a group of experts on December 15, 2015, via teleconference. The reviewers found the CFD modeling efforts to date to be quite credible and useful, but several reviewers found there to be a need for additional CFD simulations to be performed based on presented design considerations. Because Erik Voirin has finite time available to devote to this project, our team was asked to work in parallel on additional simulations of interest to the project.

35 TON CRYOSTAT MODELING APPROACH AND VALIDATION

The first task of the SDSU team was to simulate the fluid, heat, and impurity flows in the 35 Ton prototype cryostat. This was done in order to validate that our analysis is obtaining similar results to that performed by Erik Voirin at Fermilab using ANSYS CFX at FNAL. In addition, unlike the LBNF cryostat, limited experimental data from the 35 Ton cryostat is available for model validation. Like the LBNF cryostat, the flows in the 35 Ton cryostat are primarily buoyancy-driven, and many features, including the presence of the APA and CPA planes, must be accounted for. The 35 Ton cryostat was chosen for validation of our modeling approach because of the similarities with the LBNF detector coupled with the fact that it is smaller. Due to its small size, the computational time required for the simulation was significantly reduced. Therefore, changes to our modeling practices could be implemented more efficiently.

Geometry Cases

Two inlet locations for the 35 Ton cryostat were simulated. The first location is the original inlet location located near the bottom of the cryostat, as illustrated in Figure 1. The second location is along the same pipe as before, but is located 0.25 m from the top surface of the cryostat and is pointed toward the wall at a 45 degree angle toward the center of the cryostat (in the z direction).

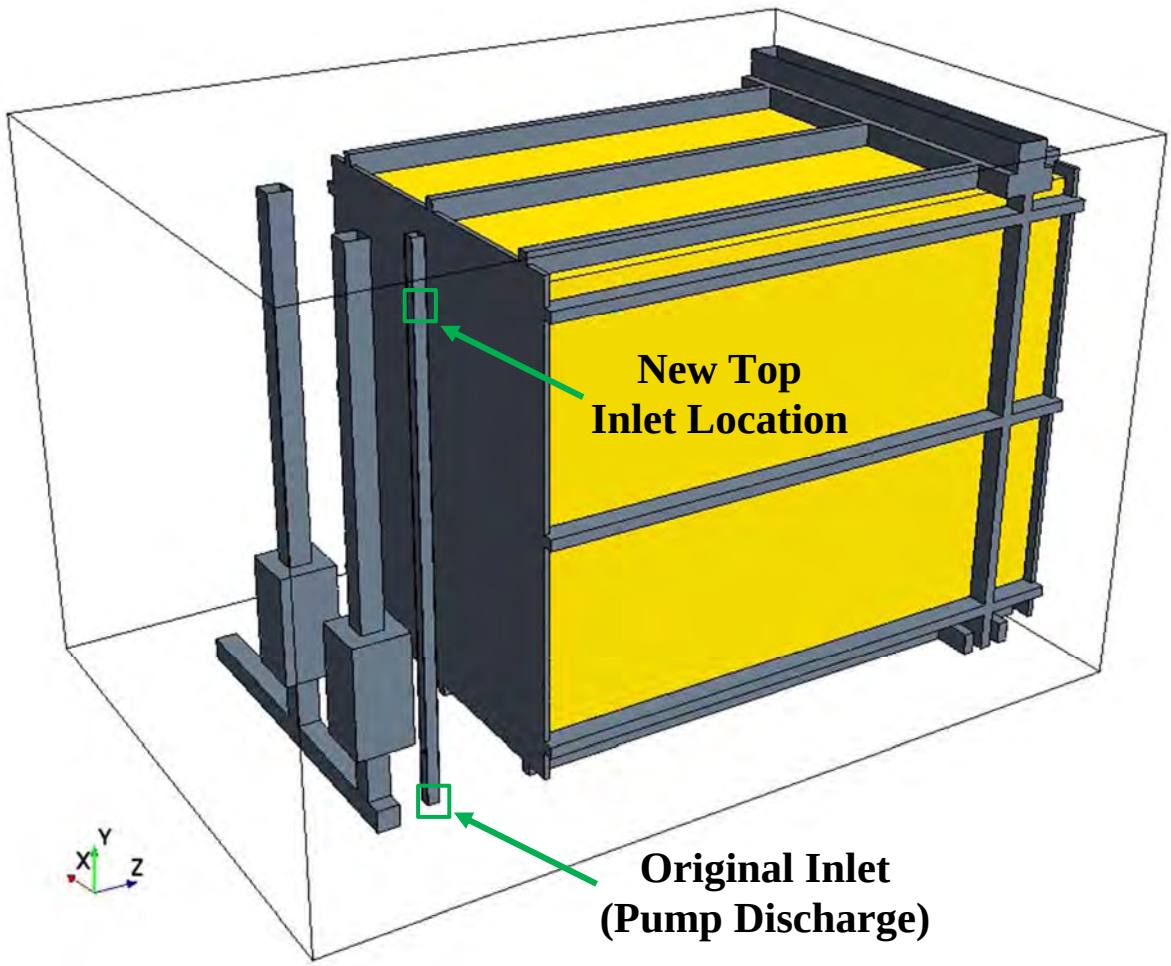

Figure 1: 35 Ton geometry view showing inlet locations.

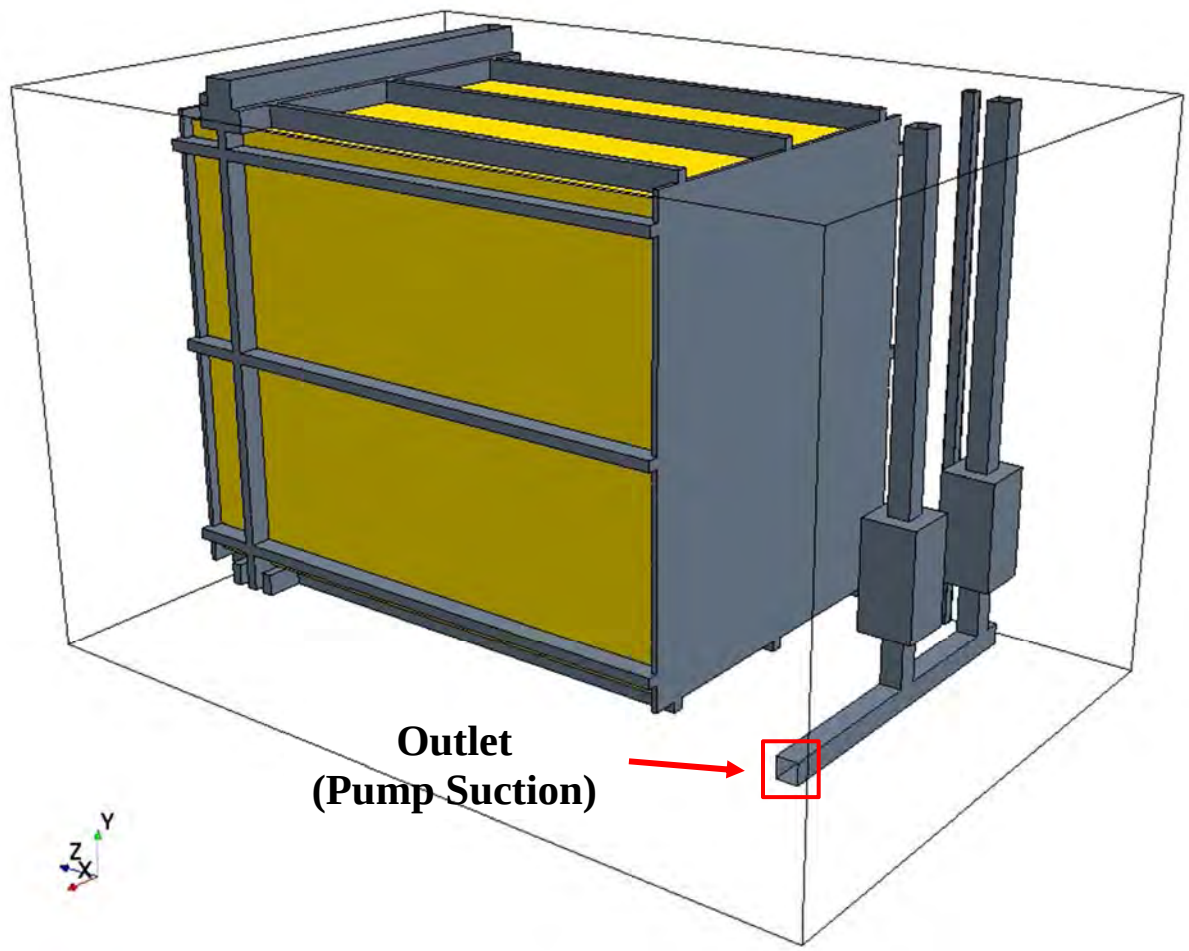

Figure 2: 35 Ton geometry view showing outlet and field cage.

Boundary Conditions (Operational Parameters)

The simulations used the boundary conditions listed in Table 1.

Table 1: 35 Ton simulation boundary conditions.

Boundary	***Conditions***
Liquid/Gas Interface (Top Wall)	Constant Temperature: 87.704 K (LAr saturation temperature) Impurity Flux: 0.201 ng/(m^2∗sec) No-Slip - per Erik Voirin
Remaining Outer Walls	Constant Heat Flux: 15 W/m2 No-Slip
Pump Discharge (Inlet to cryostat)	Flow Rate: 9.5 GPM

	Temperature: 87.808 K
Field Cage	Porosity of 23% Porous Region with 9.93 kg/m4 Inertial Resistance (no viscous resistance)

Using Porous Membranes to Simulate Field Cage

The grid size of the simulated 35 Ton simulation is too large to accommodate the true geometry of the field cage planes. The method Fermilab is using and that we have elected to use is to treat the field cage planes as porous media in the model. The settings for porous media in Star-CCM+ include an inertial and viscous resistance that determines the pressure drop across the porous media depending on fluid properties and velocity.

It was recommended by Erik Voirin to neglect the viscous resistance and only use an inertial resistance since it is much larger than the viscous resistance. Through a simulation he had previously run, the pressure drop at 3 mm/s was known, shown in Figure 3.

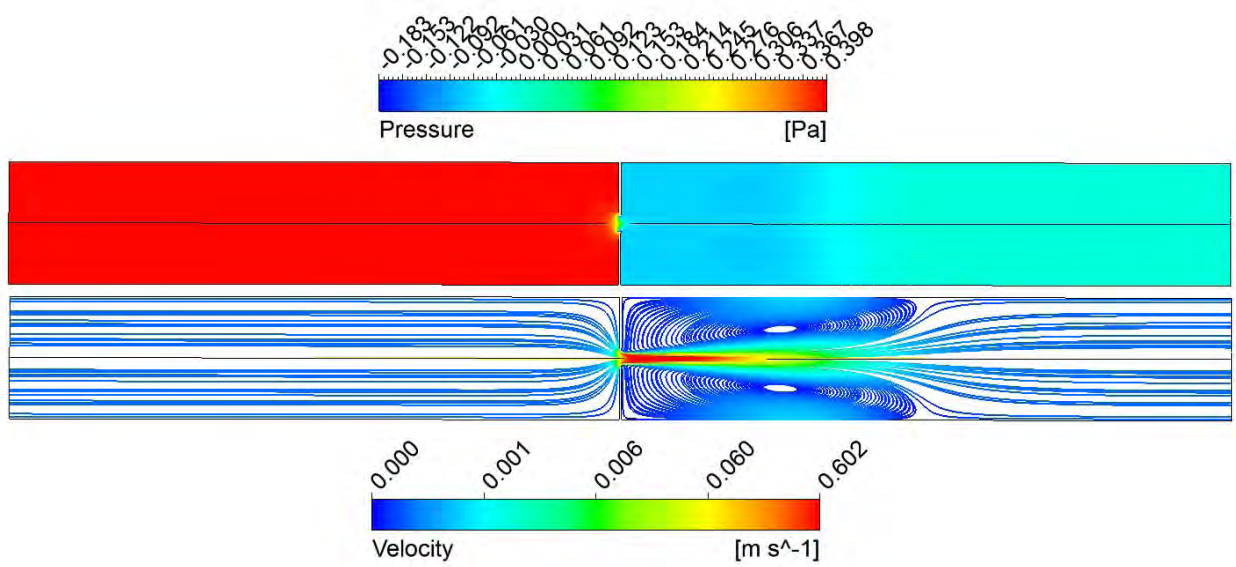

Figure 3: Fermilab simulation of 12.5% open slot representative of field cage geometry.

Since viscous resistance was neglected, the inertial resistance was found through trial and error using a simple simulation with a porous region of the same thickness to be used in the full 35

Ton cryostat simulation. The geometry of the simulation is shown in Figure 4. The inlet is on the left and the outlet is on the right. The orange region is the porous region.

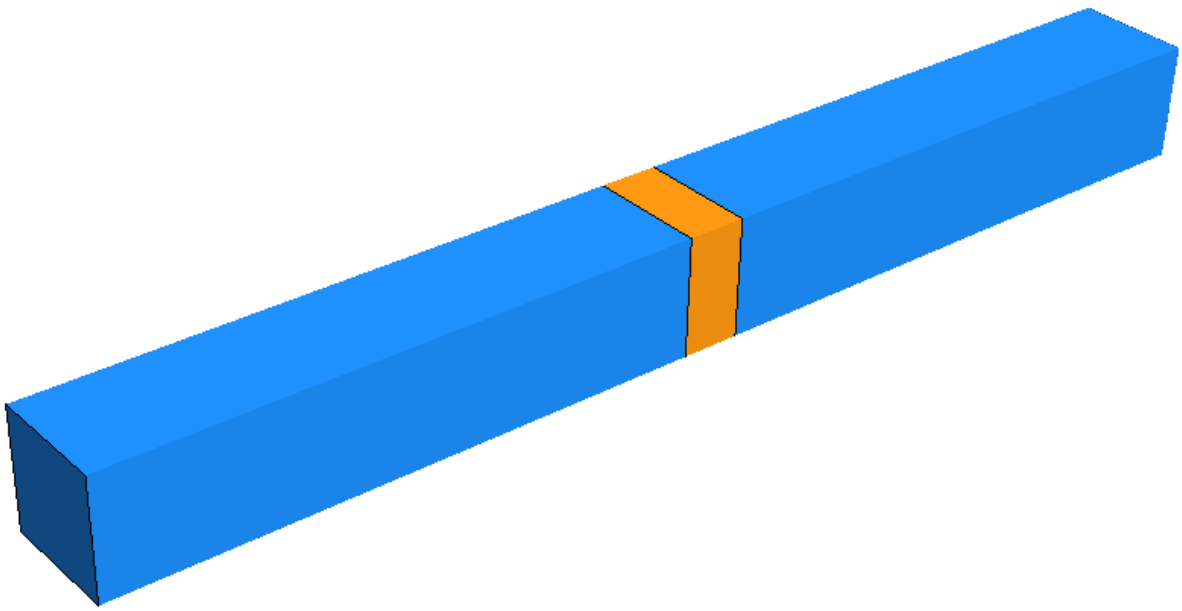

Figure 4: Simulation geometry used to find inertial resistance coefficient.

This method was quick and used information that was already available from Fermilab. A more complete method of finding the inertial and viscous resistances is accomplished by making a simulation of a small section of the actual field cage plane geometry and finding the pressure drop across it for several points in the expected velocity range. The relationship of velocity and pressure drop can be fitted with a quadratic trend line from which the coefficients can be used to determine resistance values. This process of determining the resistance coefficients was used for all of the LBNF simulations and is outlined in detail in the corresponding sections.

Physics Continua

The simulations used the physics model listed in Table 2.

Table 2: 35 Ton simulation physics continua.

Physics Model	***Description***
Segregated Flow	Flow and energy equations are solved separately.
Constant Density	Used to simplify calculation. Density change is simulated with the Boussinesq Model.
Steady State	

K-Omega SST Turbulence	This is the recommended turbulence model for buoyant convection flow
Boussinesq Model	Creates the buoyant force to induce natural convection. $\mathbf{f}_g = \rho\, \mathbf{g}\, \beta \left(T_{ref} - T\right)$, where $\beta =$ thermal expansion coefficient, $T_{ref} =$ average temperature

The simulations used the liquid argon properties listed in Table 3.

Table 3: LAr properties assumed in simulations.

Property	***Value***
Density	1387 kg/m^3
Viscosity	2.498 Pa-s
Specific Heat	1118.9 J/kg-K
Thermal Conductivity	0.1264 W/m-K
Thermal Expansion Coefficient	0.004508 1/K
Turbulent Prandtl Number	0.9

Computational Mesh Settings

The 35 Ton cryostat simulations used a polyhedral mesh with a base size of 5 cm, with wall surfaces refined down to 2.5 cm. Seven prism layers were used to capture the boundary layer near the wall. This resulted in a mesh with 2.9 million computational cells. This mesh type differs from previous Fermilab simulations, which have used structured hexahedral computational meshes. It is beneficial to analyze a problem using multiple meshes so that the effect of the mesh on the solution can be established. If the solution is the same or very similar between two different meshes, this validates that the mesh is accurately representing the physics. A cross section of the mesh used for the 35 Ton cryostat is pictured in Figure 5.

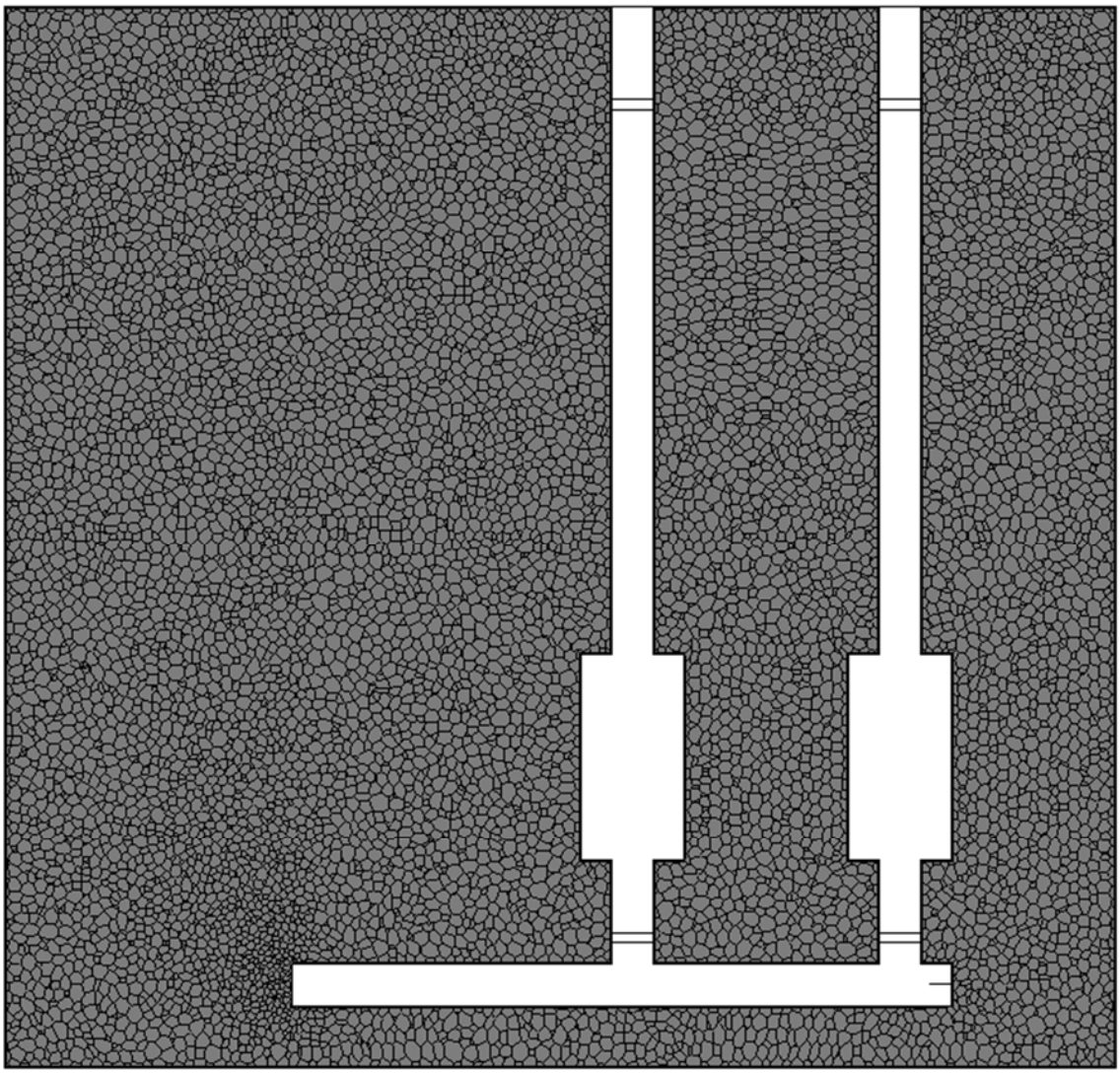

Figure 5: 35 Ton mesh section view through pump suction (outlet).

The y+ value is a dimensionless wall distance parameter that is used in the turbulence model. From the STAR-CCM+ User Guide describing y+: "… a scalar field that represents the non-dimensional wall distance. It is defined as $y^+ = u^* y/\nu$ where u^* is the reference velocity, y is the normal distance from the centroid to the wall in wall-adjacent cells, and ν is the kinematic viscosity." Also from the STAR-CCM+ user guide, the value of u^* is $u^* = \tilde{\nu}/(\kappa\tilde{d})$ where $\tilde{\nu}$ is the modified turbulent diffusivity, κ is the von Karman constant, and $\tilde{d}$ is the turbulent length scale.

For accurate heat transfer results, the y+ value must be maintained at 1.0 or less. Since the viscosity or the velocity of the fluid cannot be changed, the cell centroid distance is typically the only adjustable parameter. By making the prism layers thinner, the y+ value will decrease since the centroid of the cell will be closer to the wall.

Convergence Criteria

- Residuals:
  - Residuals of continuity, x momentum, y momentum, and z momentum should be below 0.01.
- Mass Balance:
  - Less than 1% difference in the mass of argon entering and exiting the cryostat over 1000 iterations. This is very rarely an issue since STAR-CCM+ always exactly balances the mass flow when everything is set correctly.
- Temperature:
  - Temperature change in average surface temperature of walls should be less than 0.02 K over 1000 iterations.
- Passive scalar concentration:
  - The percent difference in the mass of impurities entering and exiting the cryostat should be within 5% difference.

Passive Scalar Calculations

Impurity Levels

As mentioned in the physics continua, the impurity concentration was simulated using a passive scalar. An analogy to the behavior of the passive scalar would be that of adding dye to the fluid. The dye will be transported by the fluid throughout the volume, but it does not affect the flow of the fluid. A constant passive scalar flux was set on the top surface to simulate the impurities entering the fluid, while the fluid coming from the cryostat inlet contained no impurities.

Electron Lifetime

The electron lifetime was calculated from the passive scalar impurity concentration. This section will outline the process used to calculate electron lifetime from impurity concentration. The general equation for the electron lifetime was given by Fermilab:

$$\frac{\text{electon lifetime}[\mu s]}{\mu s} = \frac{30}{\left(\frac{\text{Volume Concentration } H_2O}{\text{parts per billion}}\right)}$$

In STAR-CCM+, the passive scalar concentration is a density representing the mass of passive scalar per mass of argon. The first step is that the density must be converted to a ratio of water molecules to argon molecules:

$$\frac{\mathrm{C_{H2O}}[kmol_{H2O}]}{\mathrm{C_{LAr}}[kmol_{LAr}]} = \mathrm{ImpDensity}\left[\frac{kg_{H2O}}{kg_{LAr}}\right] * \frac{\mathrm{MW_{Ar}}\left[\frac{kg_{LAr}}{kmol_{LAr}}\right]}{\mathrm{MW_{H2O}}\left[\frac{kg_{H2O}}{kmol_{H2O}}\right]}$$

The molecular ratio can be converted to parts per billion by multiplying by one billion:

$$\mathrm{PPB} = \frac{\mathrm{C_{H2O}}[kmol_{H2O}]}{\mathrm{C_{LAr}}[kmol_{LAr}]} * 10^9$$

Finally, the electron lifetime is calculated by:

$$\tau_{\mathrm{electron}}[\mu s] = \frac{30}{\mathrm{PPB}}$$

A more convenient form of the equation has all three parts in the same equation:

$$\tau_{\mathrm{electron}}[\mu s] = \frac{30 * \mathrm{MW_{H2O}}\left[\frac{kg_{H2O}}{kmol}\right]}{10^9 * \mathrm{MW_{LAr}}\left[\frac{kg_{LAr}}{kmol}\right] * \mathrm{ImpDensity}\left[\frac{kg_{H2O}}{kg_{LAr}}\right]}$$

35 TON CRYOSTAT SIMULATION RESULTS

Bottom (Original) Pump Discharge Location

Below is a comparison of the electron lifetime and velocity field results of Fermilab's simulation (Figure 6) and SDSU's (Figure 7). These data show that the impurity distribution and flow structures predicted for the original inlet location with Fluent at Fermilab and with Star-CCM+ at SDSU are consistent.

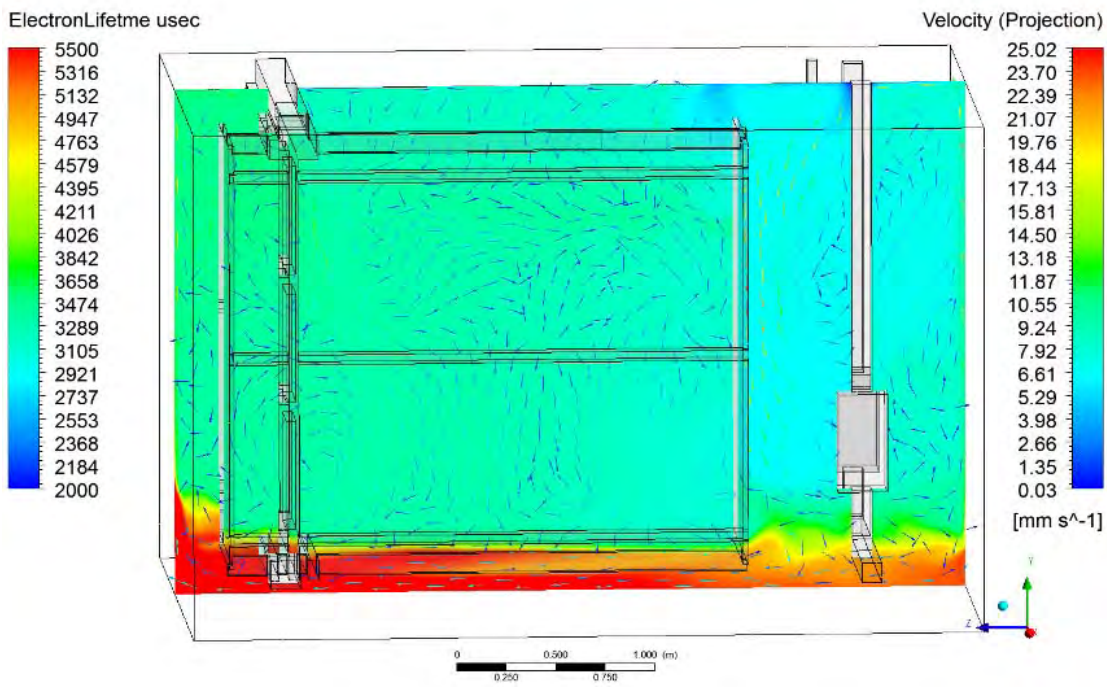

Figure 6: Fermilab simulation results for electron lifetime and velocity fields at the mid-plane of the 35 Ton prototype detector.

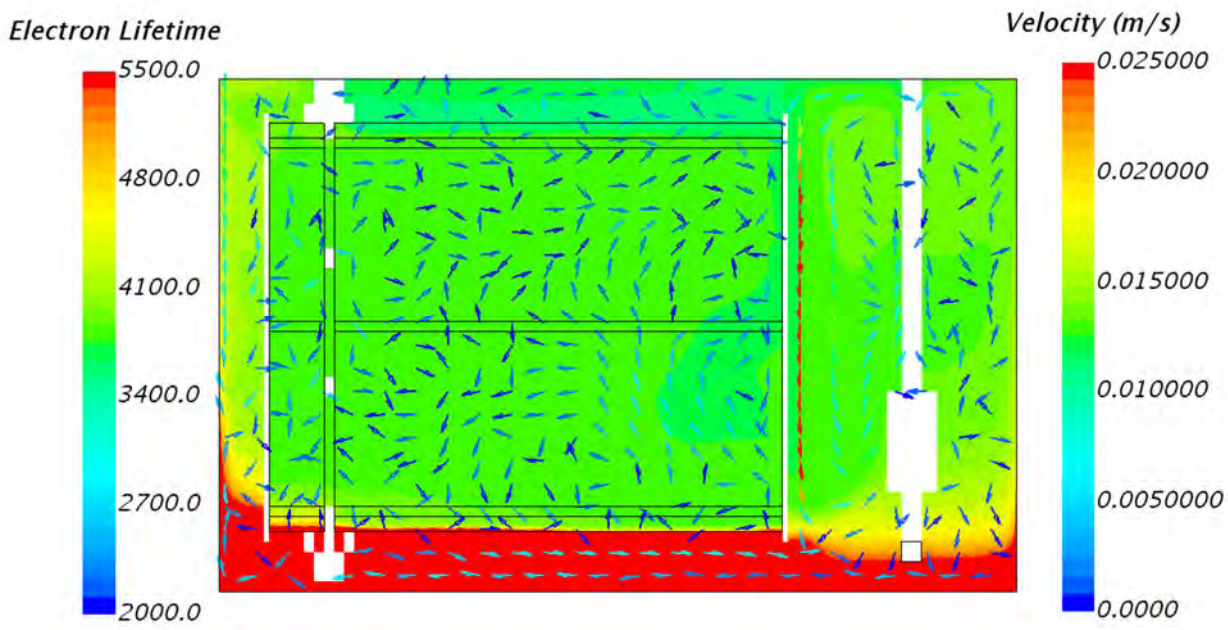

Figure 7: SDSU simulation results for electron lifetime and velocity fields at the mid-plane of the 35 Ton prototype detector.

Another reason our initial simulations were performed on the 35 Ton reactor is that there is some limited experimental data available for the impurity levels in the 35 Ton cryostat, enabling further validation of our results. The 35 Ton prototype contained 4 purity monitors in one corner of the cryostat whose locations are shown in Figure 8.

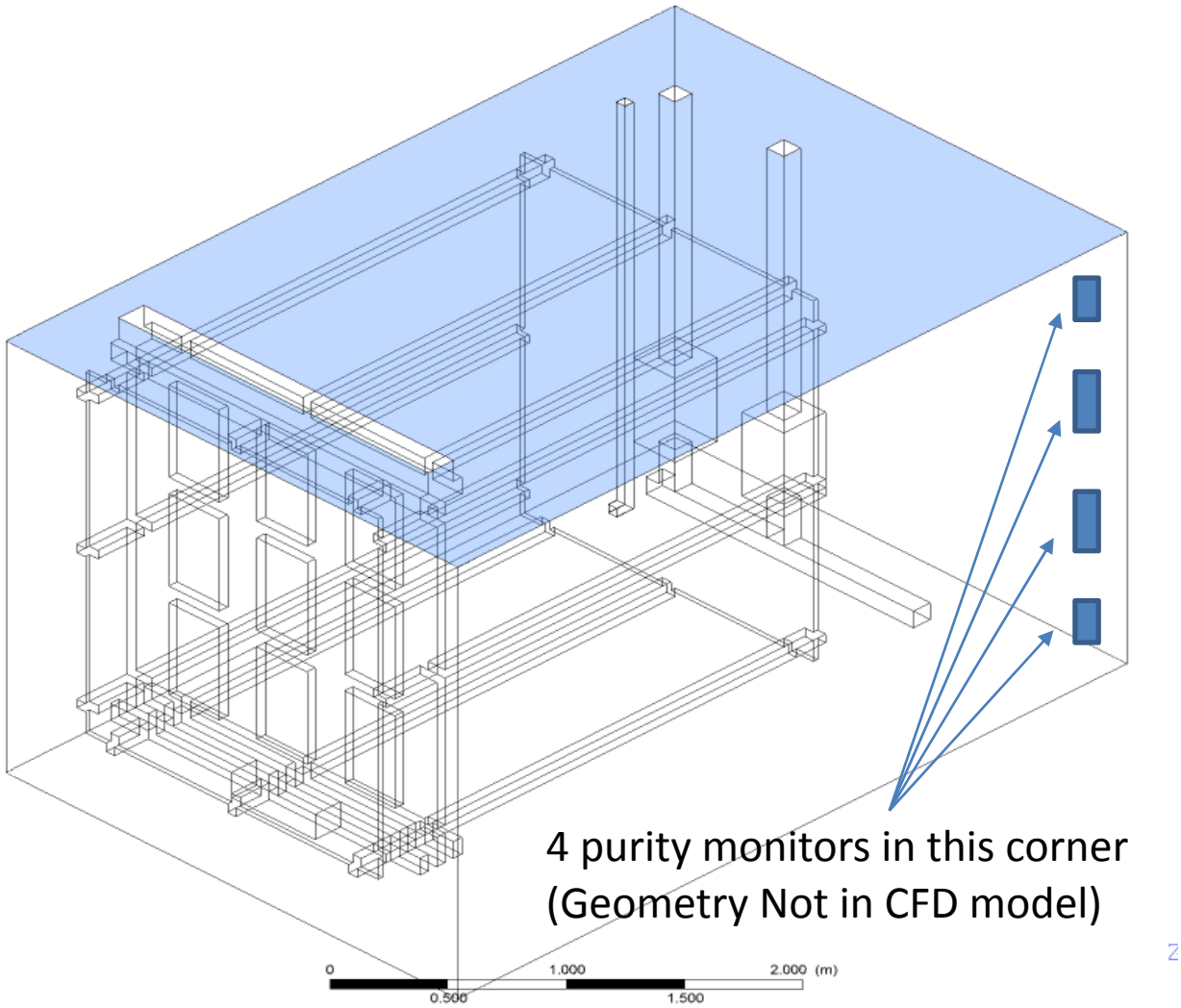

Figure 8: Locations of purity monitors in the 35 Ton cryostat.

The comparison of the electron lifetime predicted by the SDSU simulation and the experimental results and Fermilab simulation predictions (Figure 9) shows that both the Fermilab and SDSU simulations can accurately predict impurity distributions in the cryostat.

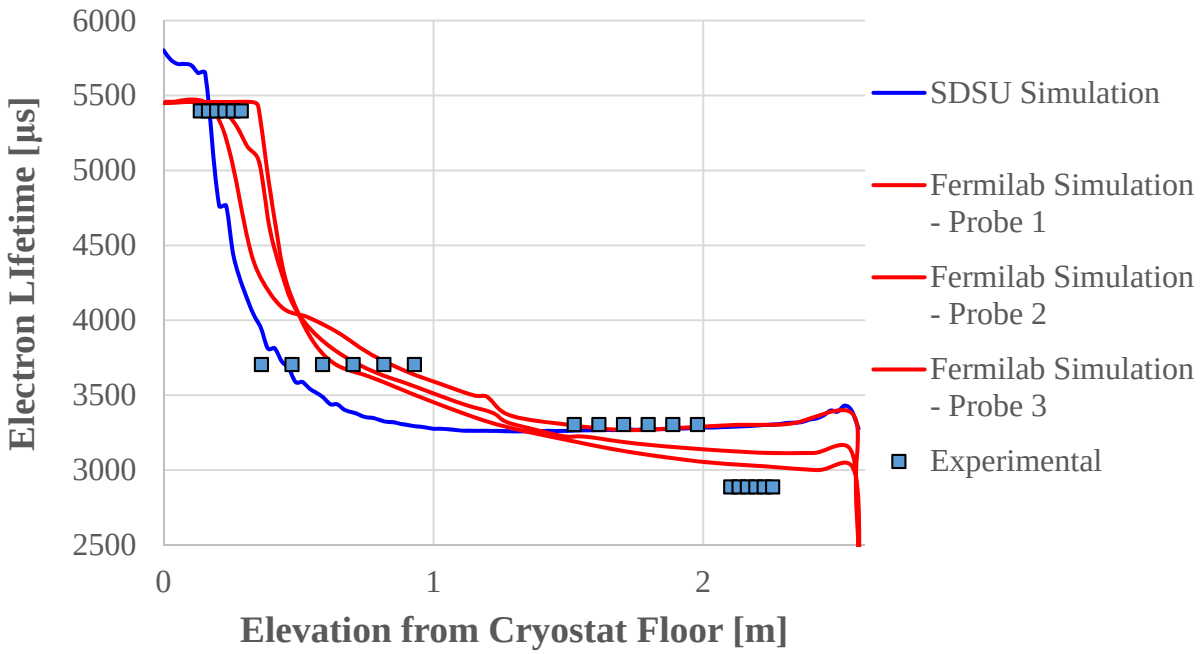

Figure 9: Comparison of experimental electron lifetime measurement at the purity monitor locations.

Figures 10 and 11 show streamlines from the 35 Ton simulation.

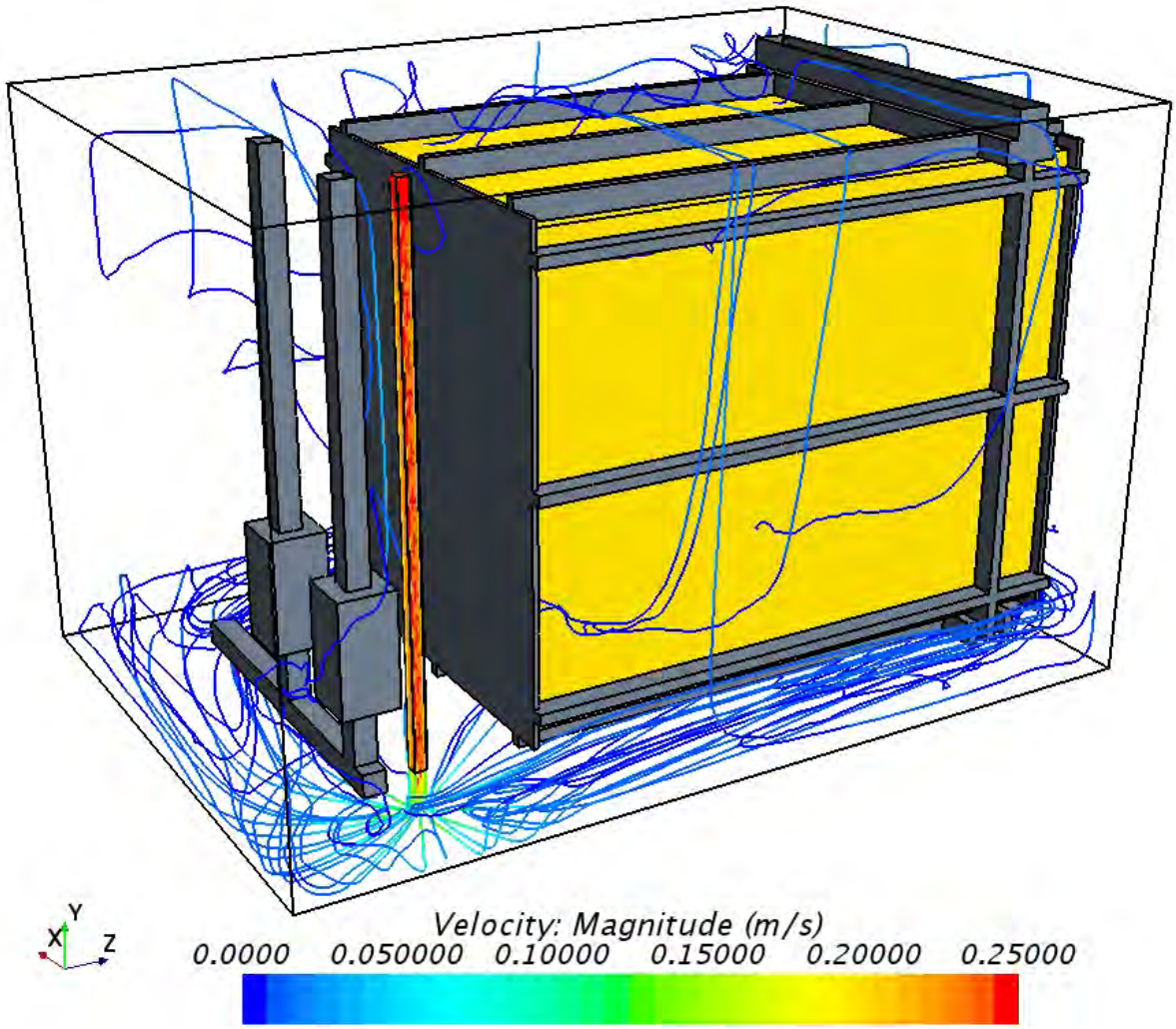

Figure 10: Streamline view from SDSU simulation.

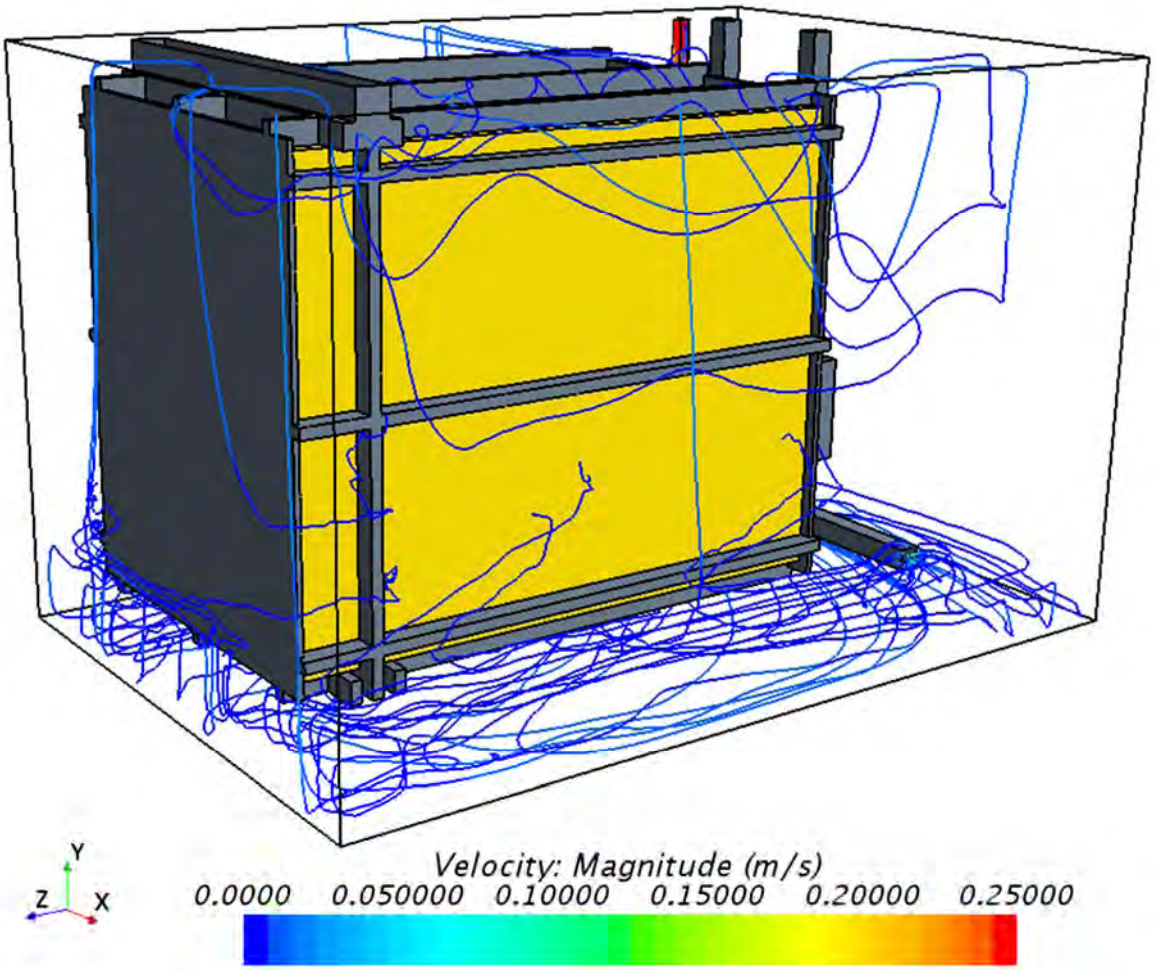

Figure 11: Streamline view from SDSU simulation.

Top Pump Discharge Location

A second inlet location was selected to create a more uniform distribution of the impurities. The inlet was placed near the top of the inlet pipe with the flow pointing at a 45 degree angle toward the center of the wall. Below we compare the electron lifetime results of Fermilab's simulation (Figure 12) with the SDSU simulation (Figure 13).

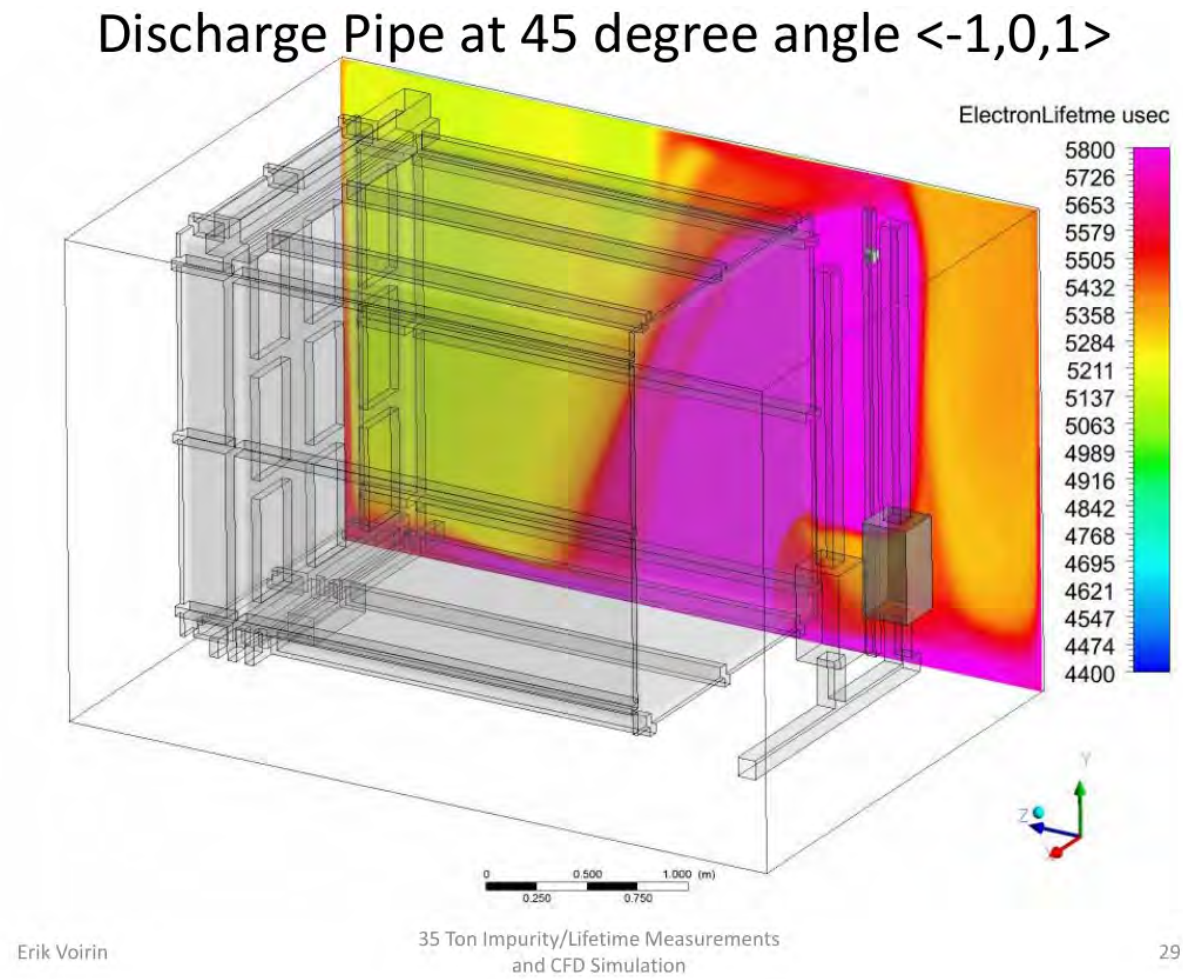

Figure 12: Fermilab electron lifetime results for 35 Ton cryostat with top inlet location.

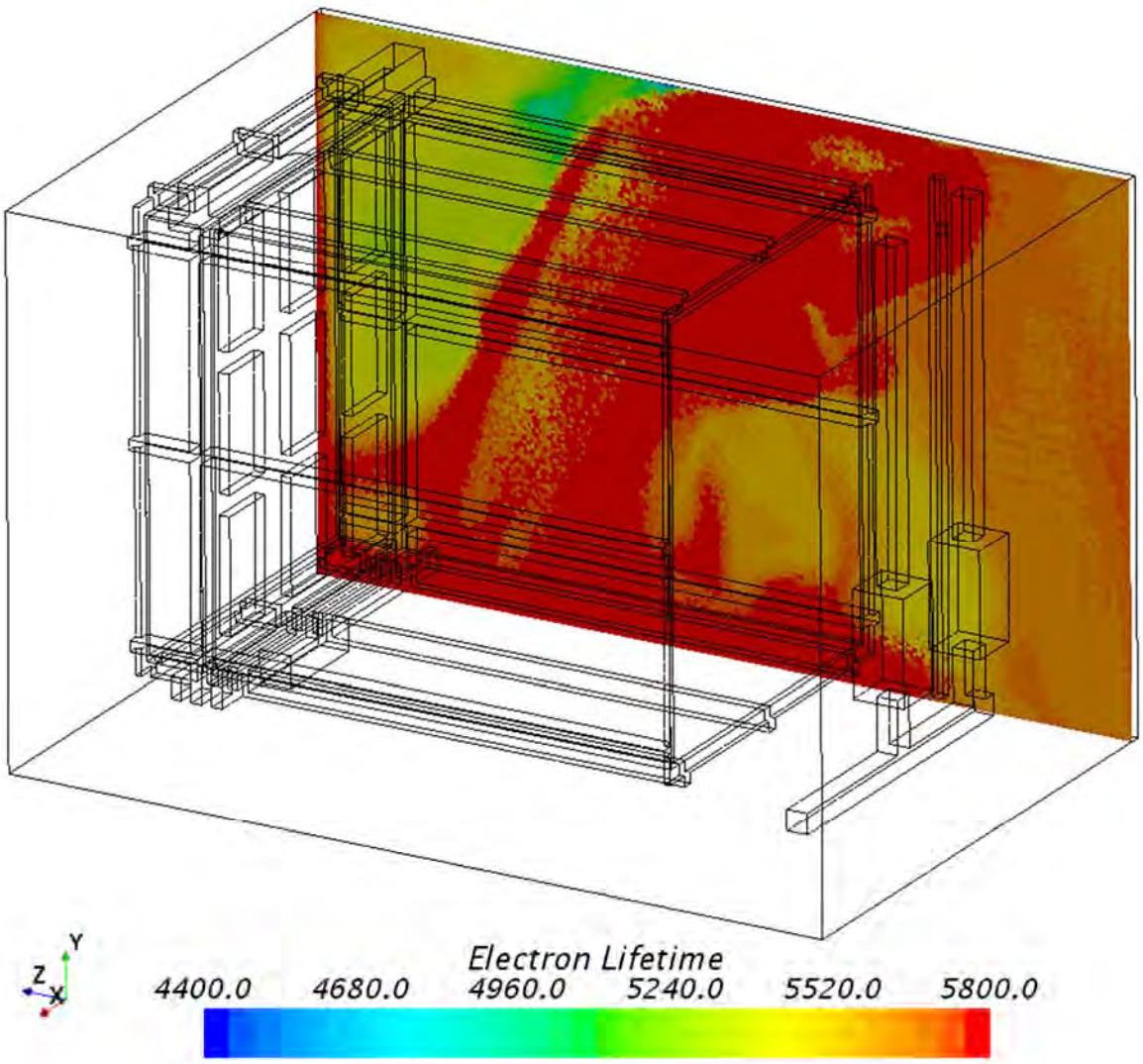

Figure 13: SDSU electron lifetime results for 35 Ton cryostat with top inlet location.

Figures 14, 15, and 16 show streamlines from the Fermilab and SDSU simulations.

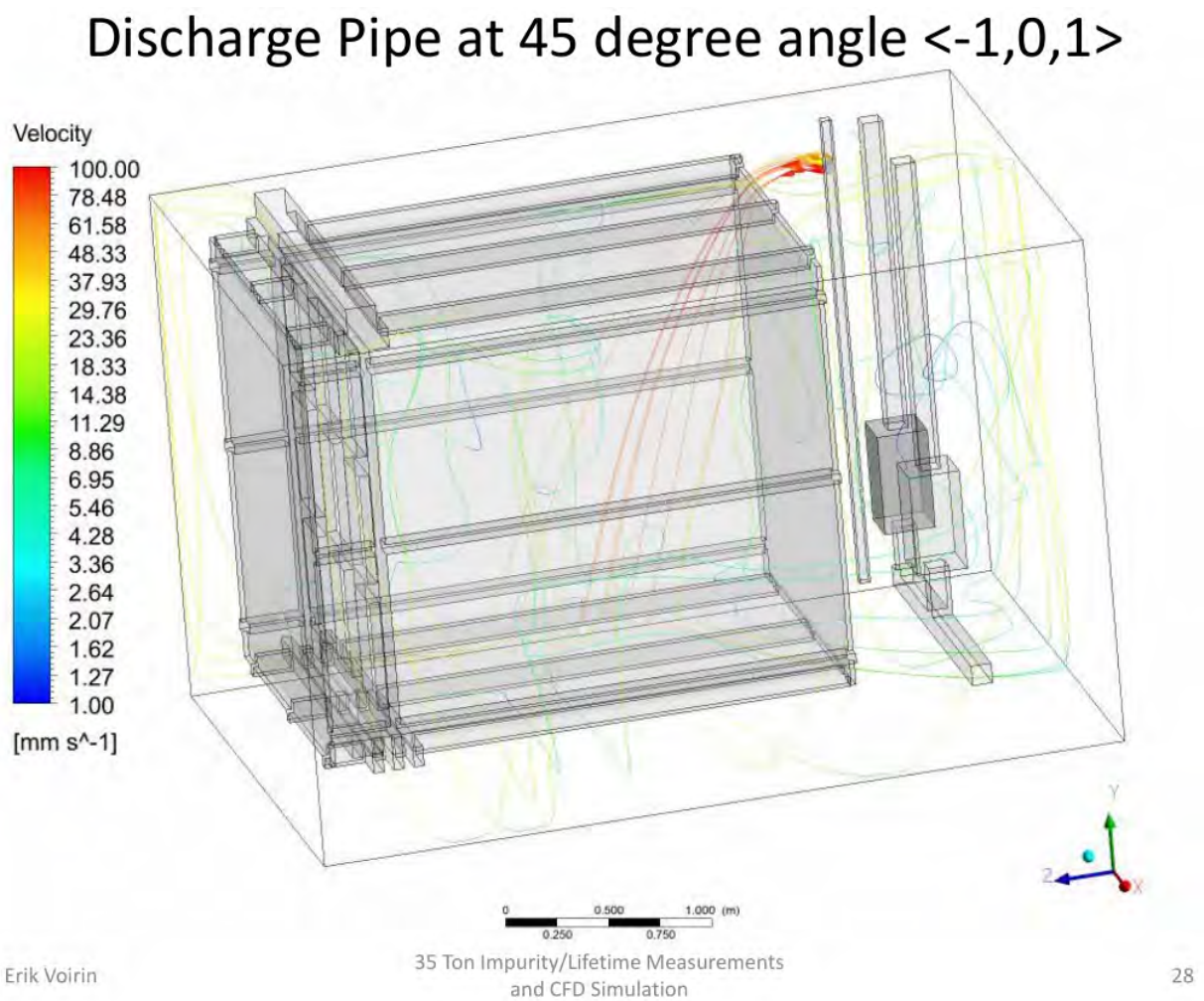

Figure 14: Streamline view from Fermilab simulation of top inlet at an angle of 45 degrees.

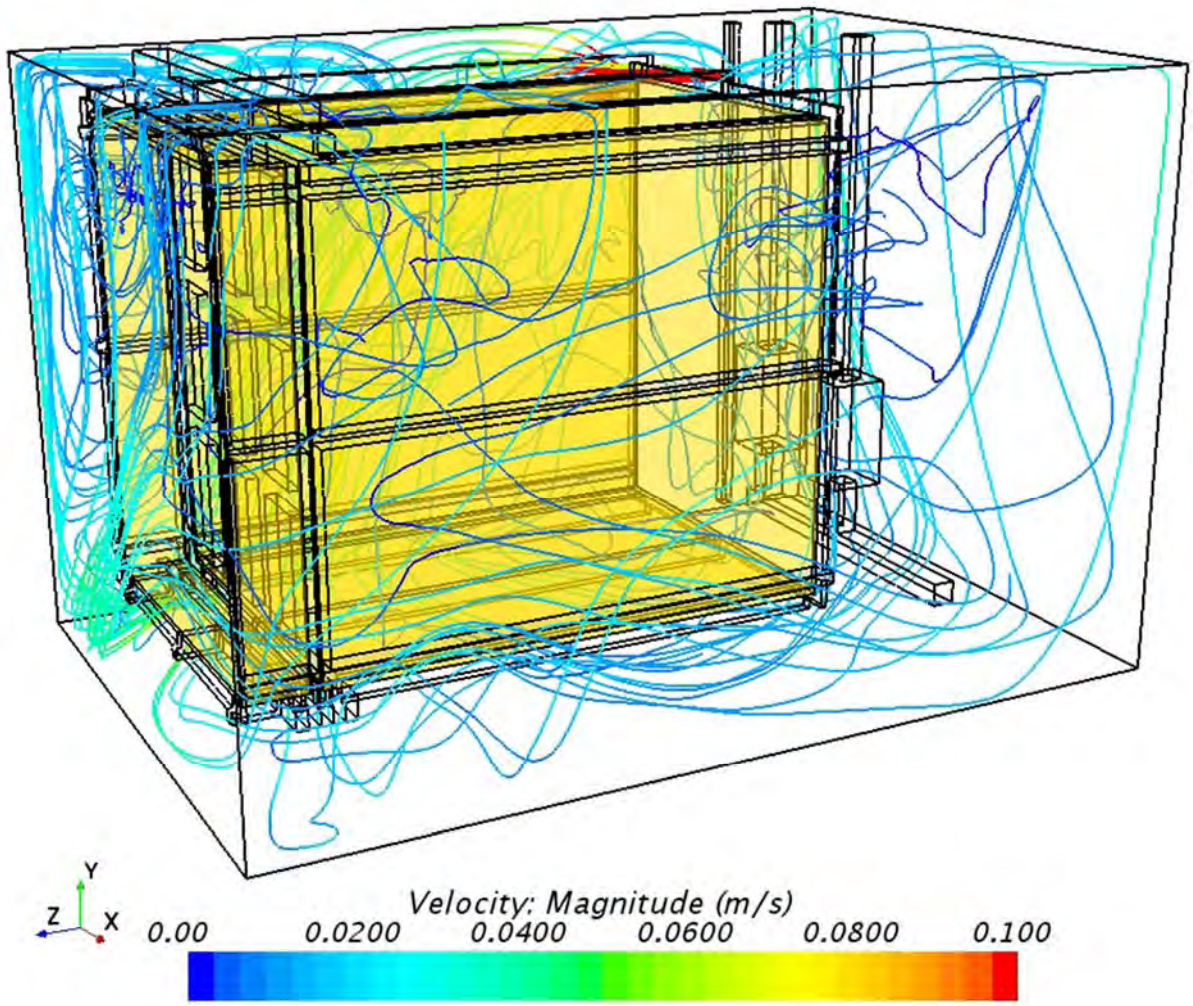

Figure 15: Streamline view from SDSU simulation of top inlet at an angle of 45 degrees.

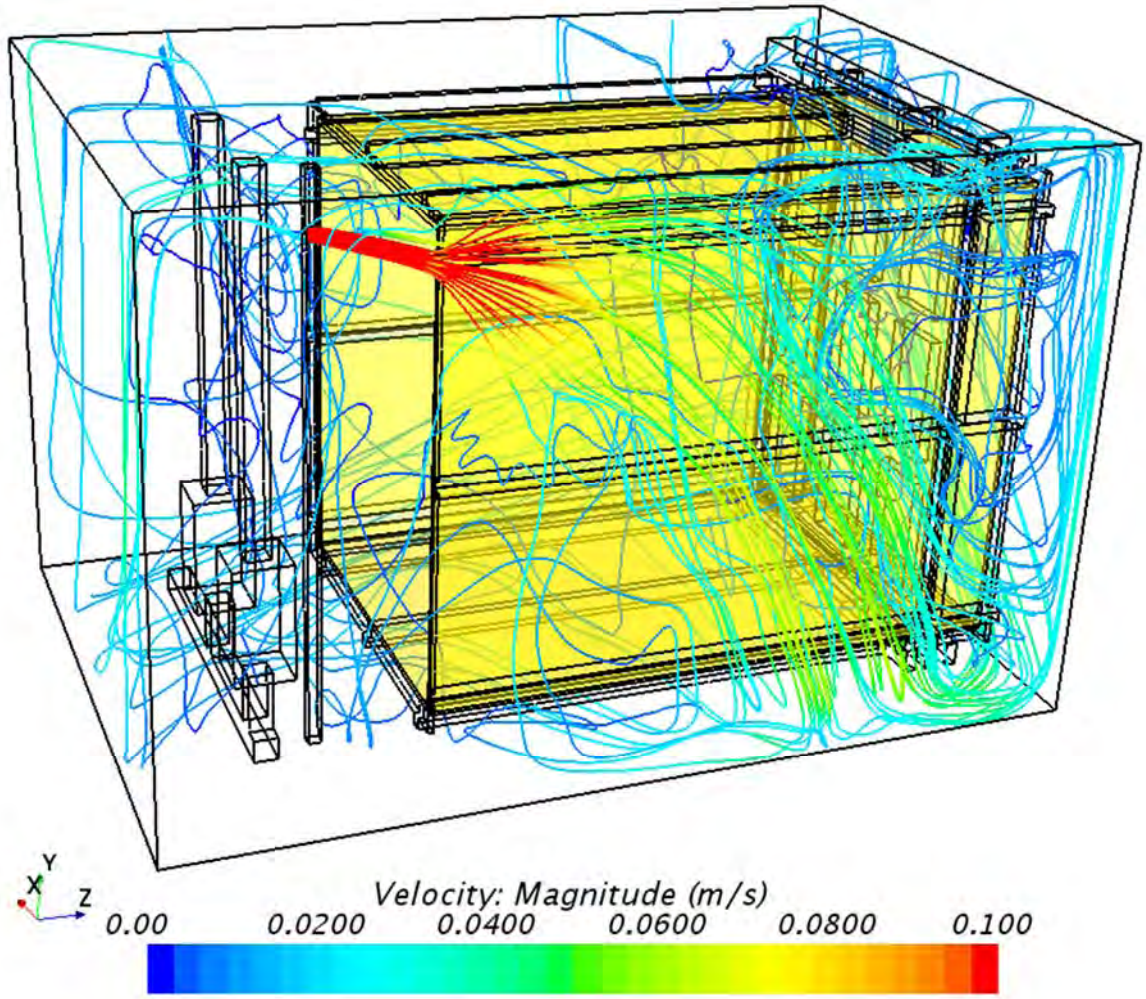

Figure 16: Additional streamline view from SDSU simulation of top inlet at an angle of 45 degrees.

The electron lifetime at the purity monitor is shown in Figure 17. The electron lifetime with the proposed new fluid outlet location is both longer and more consistent over the height of the cryostat.

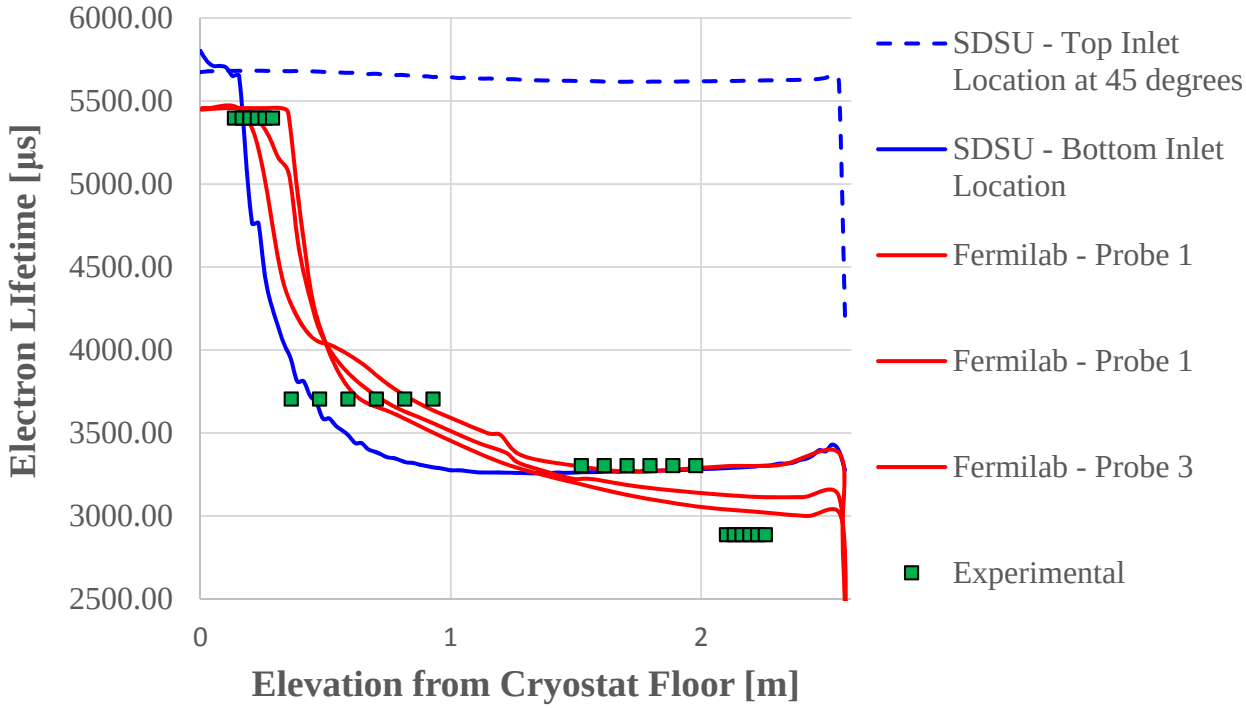

Figure 17: Electron Lifetime vs Elevation with Top Inlet at 45 Degrees.

DUNE LBNF MODELING APPROACH

Once our simulations were validated, our next goal was to investigate the symmetry of fluid, heat, and impurity flows in the LBNF cryostat. Through our conversations with Erik Voirin at Fermilab, we learned that he has been assuming a symmetric flow in the cryostat in order to reduce the size of the simulated volume and decrease computational time. We agreed with Erik's suggestion that it would be helpful to simulate a model that included the entire volume of the cryostat to confirm that this assumption was valid.

Geometry Cases

Common Geometry Features:

The origin of the cryostat is located on the bottom center surface in all simulations. The geometry of the LBNF cryostat includes three APA planes (approx. 73% open), two CPA planes (solid, impenetrable), and four field cage planes (23% open) as illustrated in Figures 18 and 19. The CPA planes are located 3.45 m from the origin in the x direction. The APA planes are located at the center of the cryostat and 7.55 m from the center in the x direction. The horizontal field cage planes are located at 0.7 m and 12.57 m from the origin in the y direction.

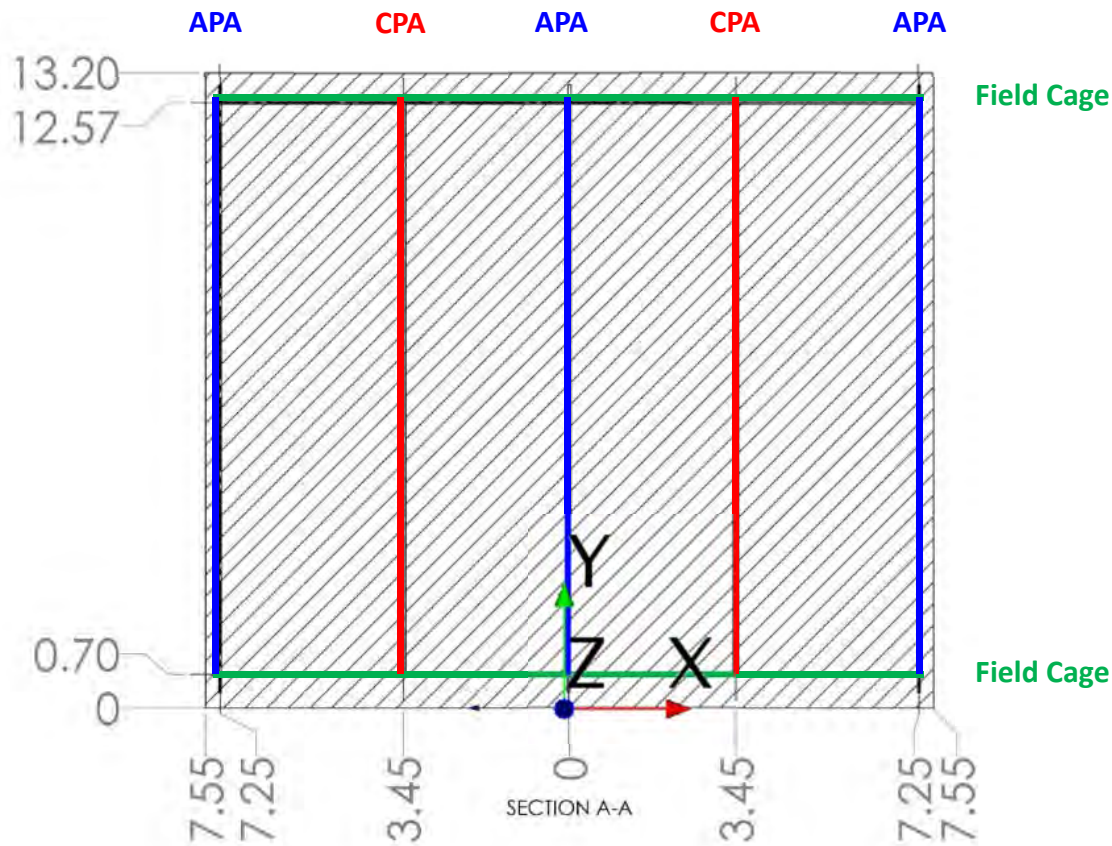

Figure 18: Cross section showing APA, CPA, and Field Cage planes.

Figure 19 shows the location of the field cage planes from a cross section in the y-z plane. The vertical field cage planes are located at 30 m and 28 m from the origin in the z direction.

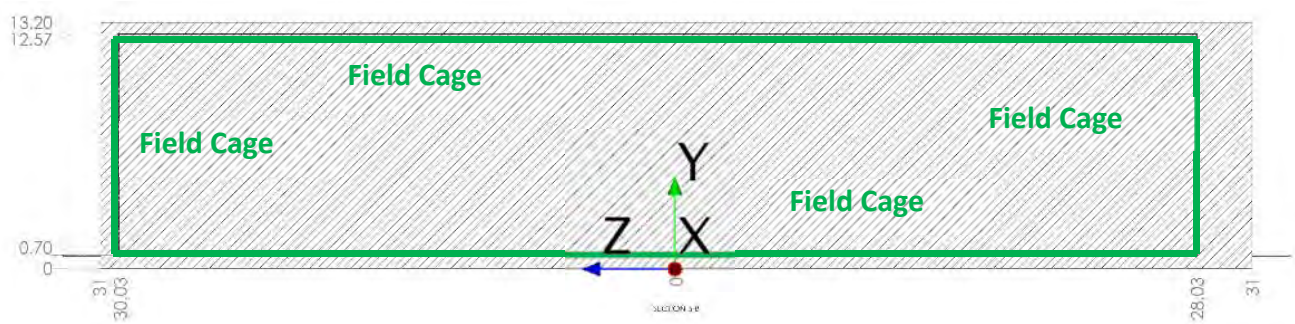

Figure 19: Cross Section showing Field Cage planes.

V1:

The V1 configuration has one LAr inlet and four outlets. The inlet is at one end of the cryostat near the floor, and the outlets are on the opposite end of the cryostat. Figure 20 shows a cross section looking down on the cryostat from the y direction. The inlet is located on the left 30.5 m

from the origin in the z direction. The four outlets are four pipes spaced across the width of the cryostat in the x direction on the opposite end of the cryostat. The pipes are located 0.7 m from the floor.

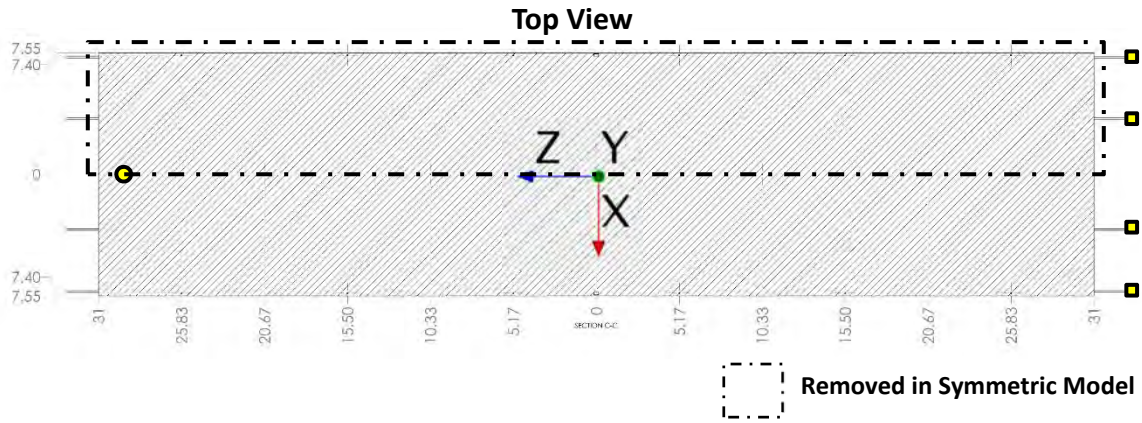

Figure 20: Cross section showing inlet and outlet locations in V1 configuration.

Latest Configuration:

The latest configuration has the outlets distributed along the entire length of the cryostat, with seven outlets (pictured in red) in the center and six inlets (pictured in green) on each wall for twelve total inlets (Figure 21). The five outlets in the center have an even flow split and the outlets on the two ends of the cryostat each have half the flow rate of the others (Table 4).

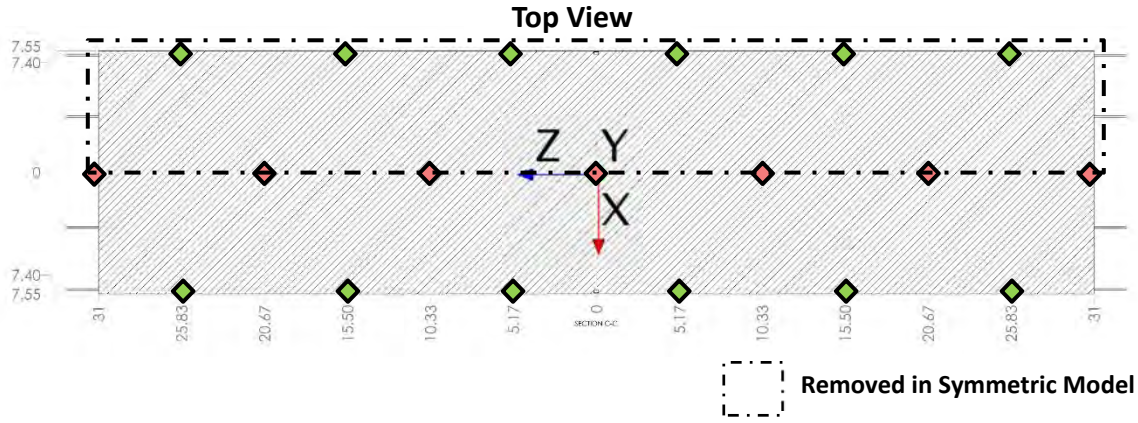

Figure 21: Cross section showing inlet (green) and outlet (red) locations in latest configuration.

A list of the inlet and outlet locations is given in Table 4. All inlets and outlets are located 0.2 m above the floor, which is why the y coordinate was not included in the table. Only the outlets on the positive x side of the cryostat were included in the simulation since it was symmetric across the y z plane at 0.0 m in the x direction. The outlets are located at zero in the x direction so they

are all included, but are half the size. All inlets and outlets were assumed to be 5 cm cubes fixed at the locations listed in Table 4.

Table 4: List of inlet and outlet locations of the latest configuration.

	Inlet	*x(m)*	*z(m)*	*Flow %*		*Outlet*	*x(m)*	*z(m)*	*Flow %*
Present in Symmetric Model	1	7.4	-25.8	8.3%		1	0.0	-31.0	8.3%
	2	7.4	-15.5	8.3%		2	0.0	-20.7	16.7%
	3	7.4	-5.2	8.3%		3	0.0	-10.3	16.7%
	4	7.4	5.2	8.3%		4	0.0	0.0	16.7%
	5	7.4	15.5	8.3%		5	0.0	10.3	16.7%
	6	7.4	25.8	8.3%		6	0.0	20.7	16.7%
Not Present in Symmetric Model	7	-7.4	-25.8	8.3%		7	0.0	31.0	8.3%
	8	-7.4	-15.5	8.3%				Total:	100.0%
	9	-7.4	-5.2	8.3%					
	10	-7.4	5.2	8.3%					
	11	-7.4	15.5	8.3%					
	12	-7.4	25.8	8.3%					
			Total:	100.0%					

Boundary Conditions

Common Conditions:

The boundary conditions assumed for the LBNF simulation are listed in Table 5.

Table 5: Description of LBNF boundary conditions.

Boundary	***Conditions***
Top Wall	LAr Saturation Temperature: 88.348 K Passive Scalar Flux: 1 kg/m^2-s (actual value is irrelevant as this will be scaled later)
Remaining Exterior Walls	Heat Flux: 7.2 W/m^2
Electronics Surfaces (Figure 22)	Total Heat Source: 23,700 W
Inlet Temperature	Maintained at 0.4418 K above outlet temperature to account for energy added through pump work Flow rates listed in Table 6
APA planes	Porosity: 73% open Inertial Resistance: 11,264.2 kg/m^4 Viscous Resistance: 118.6 kg/m^3-s
Field Cage planes	Porosity: 23% open

Inertial Resistance: 411,280 kg/m^4

Viscous Resistance: 247.4 kg/m^3-s

Figure 22 shows the electronic surfaces which has a total heat source of 23,700 W.

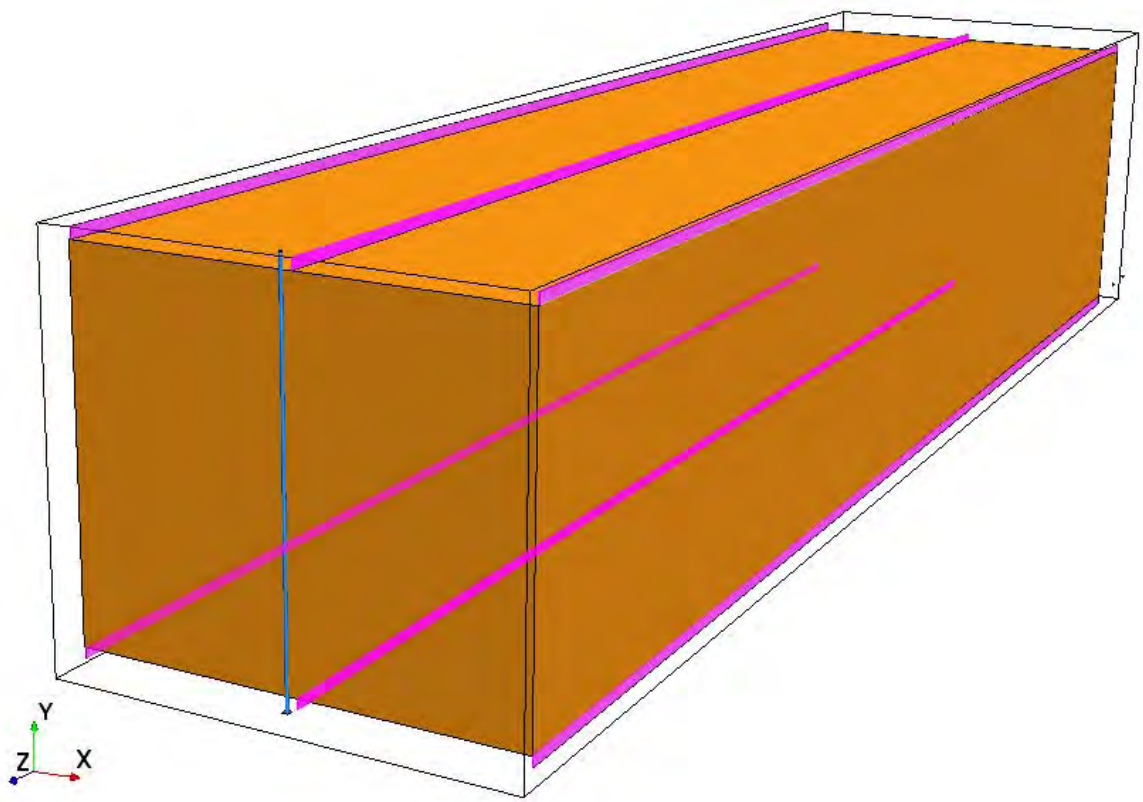

Figure 22: Geometry view with electronic surfaces highlighted.

Table 6 lists the flow rates and number of inlets and outlets present in each simulation.

Table 6: Number of pumps running in each simulation.

	V1 Full	***V1 Symmetric***	***Latest Symmetric***
Inlet Flow Rate	4 pumps	4 (2) pumps	1 (0.5) pump
Number of Inlets	1	1 (0.5)	12 (6)
Number of Outlets	4	4 (2)	7 (7, half size)

V1:

The only difference in boundary conditions between the V1 and the latest configuration is the pump flow rates, which is in the table above. The flow rate of the V1 is four pumps running at 103 GPM each, or 412 GPM total. In the symmetric model the flow rate is halved to 206 GPM since half the cryostat is removed.

Latest Configuration:

The only difference in boundary conditions between the latest configuration and the V1 is the pump flow rates, which is in the table above. The flow rate of the latest configuration is a single pump running at 103 GPM. Again, in the symmetric model the flow rate is halved to 51.5 GPM since half the cryostat is removed.

Using Porous Membranes to Simulate APA and Field Cage Planes

The grid size of the simulated LBNF cryostat is too large to accommodate the true geometry of the APA and field cage planes. The method Fermilab is using and that we have elected to use is to treat the APA and field cage planes as porous media in the model. The settings for porous media in Star-CCM+ include an inertial and viscous resistance that determines the pressure drop across the porous media depending on fluid properties and velocity. Finding these resistances is accomplished by making a simulation of the actual plane geometry and finding the pressure drop across it for several points in the expected velocity range. The relationship of velocity vs pressure drop can be fitted with a quadratic trend line from which the coefficients can be used to determine resistance values.

APA Plane

The APA planes (picture in Figure 23) consisted of 10 layers as follows:

- **Plane 1**: Vertical wires (150 micron diameter at a 5-mm pitch)
- **Plane 2**: +60° wires
- **Plane 3**: -60° wires
- **Plane 4**: Vertical wires
- **Plane 5**: Mesh (90° set of wires of 0.528-mm dia. and 5-mm pitch (80% open area))
- **Planes 6-10**: Symmetry of planes 1-5, with a 75 mm space between planes 5 and 6.

The APA simulation used five layers and the pressure was doubled when calculating the resistance coefficients.

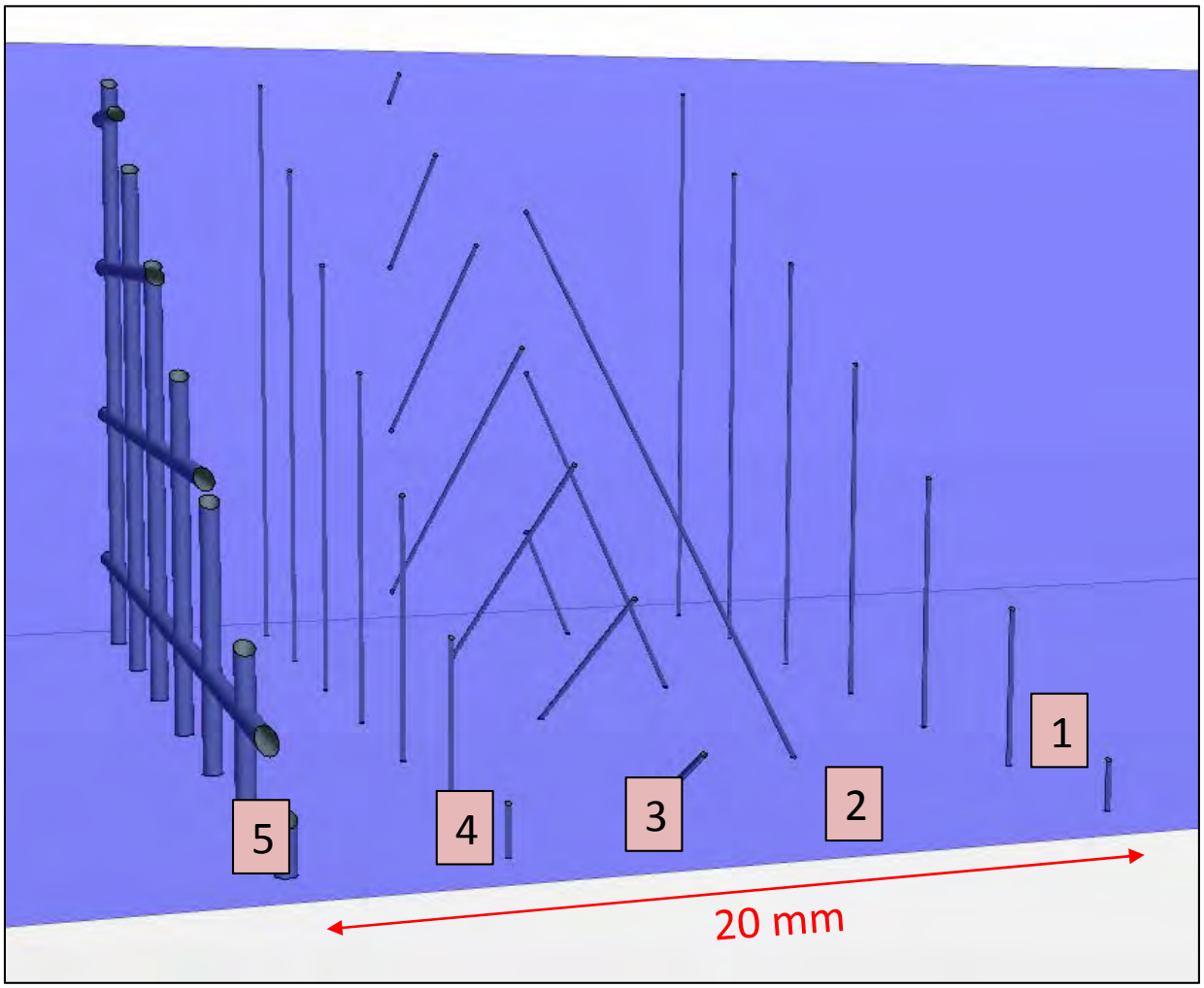

Figure 23: APA plane layer geometry view used in pressure drop simulation.

Figure 24 shows a view of the full APA pressure drop simulation. The red section is where the fluid enters and it travels to the green outlet at the opposite end. The APA mesh geometry is in the middle and will cause a pressure drop as the fluid moves past it. The blue walls are symmetry planes. The triangular cross section was chosen to decrease the number of computational cells. Additionally, only half the layers were included in the geometry. The reason for the geometrical simplifications is the 150 micron wires require a very small cell base size, which resulted in a mesh that was still around 1 million cells even though this is a very small section of the APA plane. This fact highlights the extreme difficulty of modeling the actual APA geometry in the full simulation since the computing power required would be vastly greater than what is available.

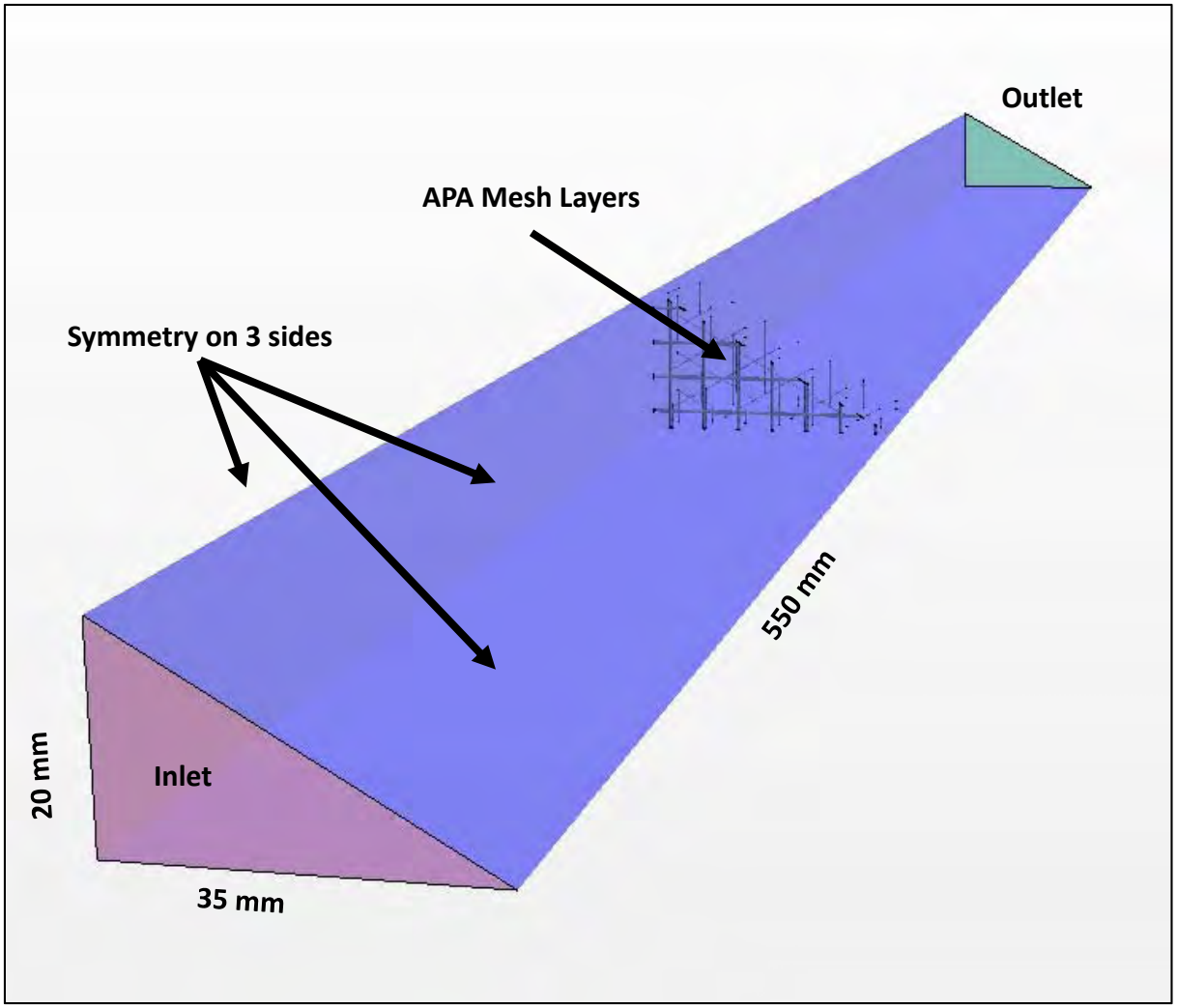

Figure 24: Full View of APA pressure drop simulation geometry.

The resulting plot of pressure drop and velocity is shown in Figure 25.

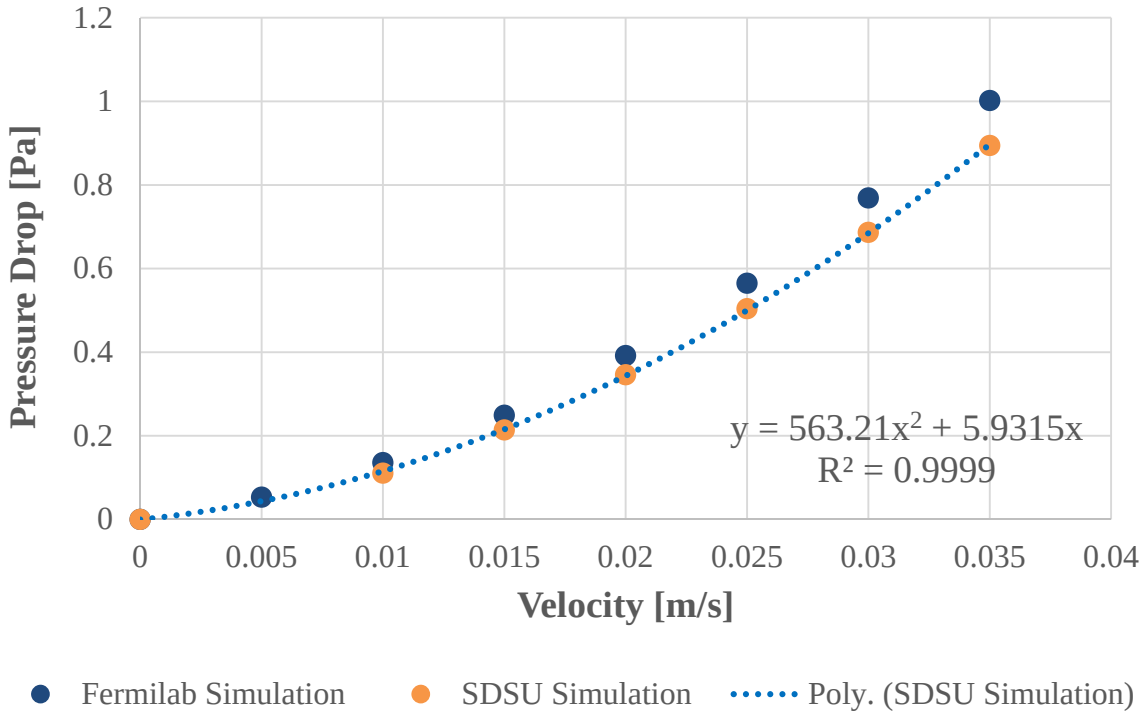

Figure 25: Plot of pressure drop vs. velocity, with coefficients used to determine resistance values.

The coefficients found from the trend line are 563 kg/m^3 and 5.9 kg/m^2-s for the inertial and viscous coefficients, respectively. These values were divided by the porous media thickness (0.05 m) that was used in the full simulation to get the final coefficients of 11,300 kg/m^4 and 119 kg/m^3-s for the inertial and viscous resistances, respectively.

To verify the coefficients, a test simulation with a porous region of the same thickness as the porous APA planes in the full simulation (0.05 m) was tested at the same velocities used to determine the coefficients. The shape of the simulated section will not affect the pressure drop, only the thickness of the plane will, so a rectangular section was simulated. The four sides of the length of the geometry are symmetry planes, as shown in Figure 26.

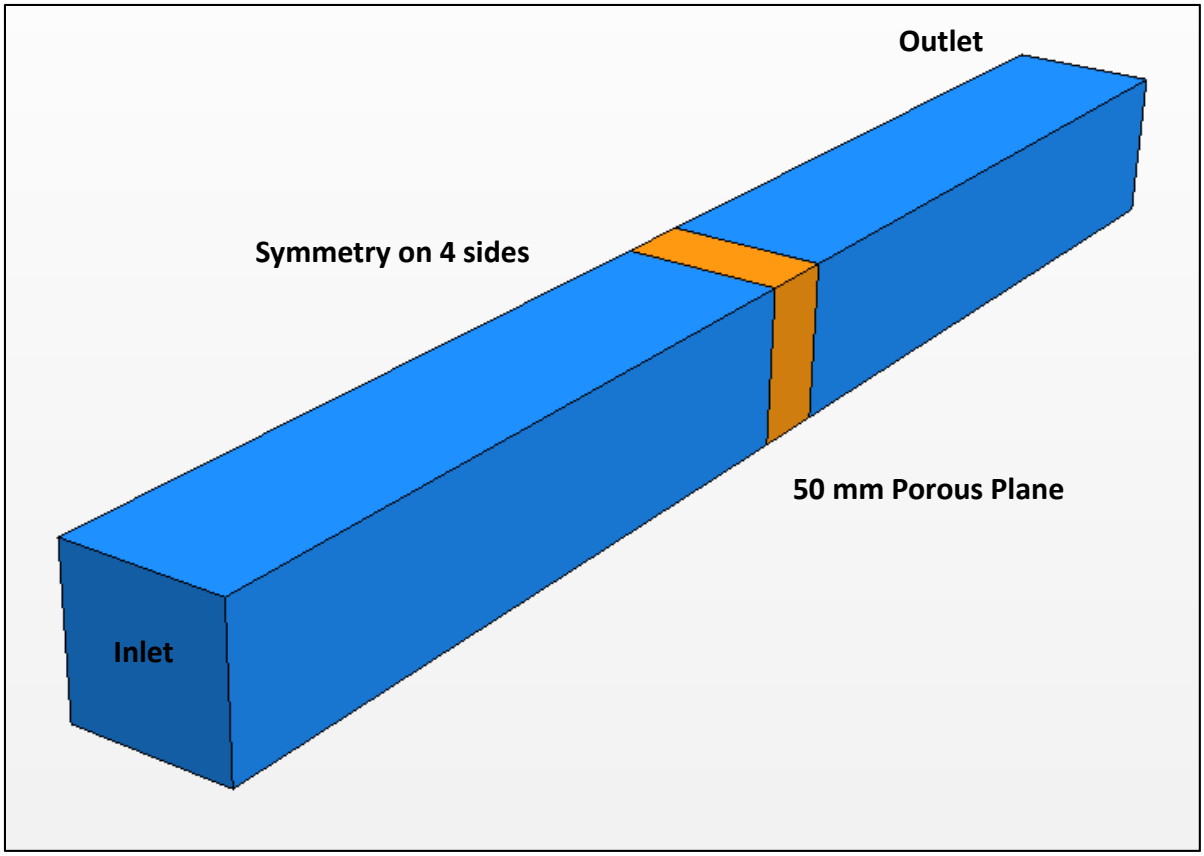

Figure 26: Geometry view of APA resistance coefficients verification simulation.

The results of the verification simulation are shown in Figure 27, which matches the original APA simulation exactly.

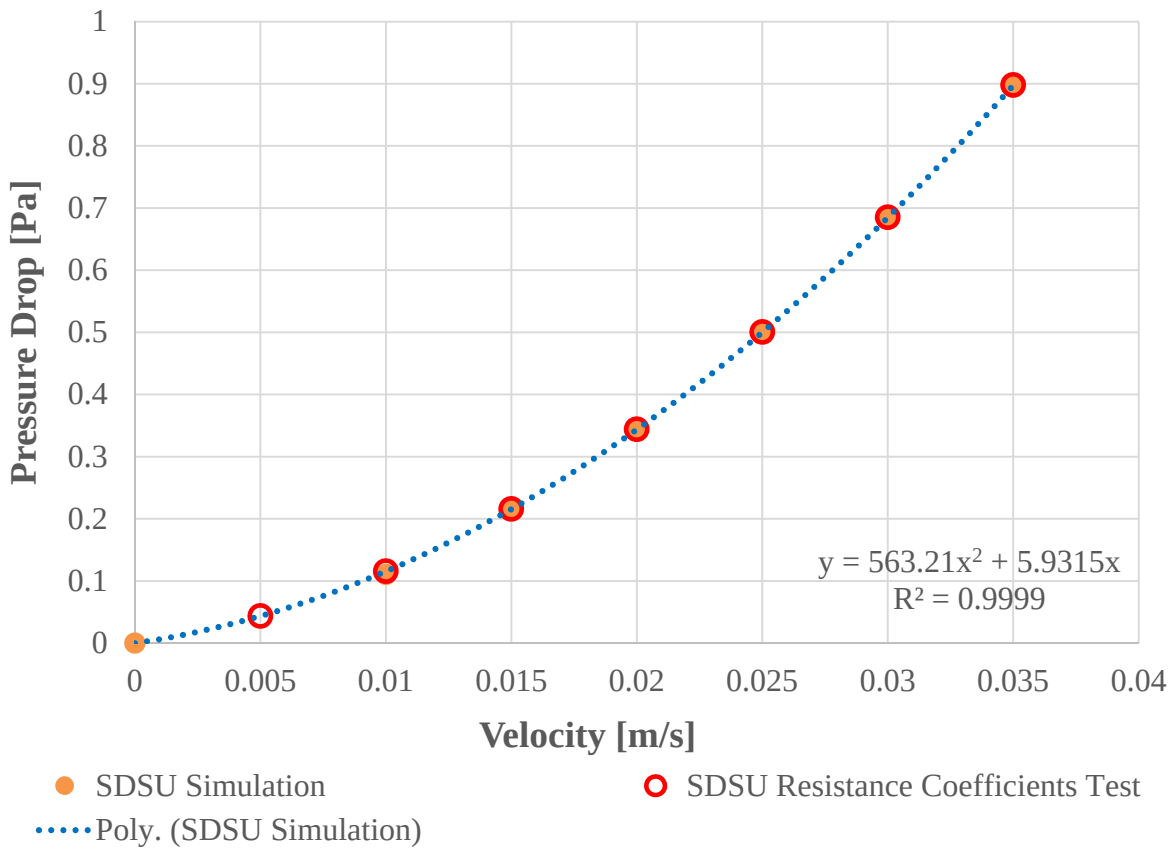

Figure 27: Plot of pressure drop vs. velocity, with results of the coefficient verification simulation (red).

Field Cage Plane

The exact same method of finding resistance coefficients for the geometry of the APA planes was also used for the field cage planes. The field cage planes are assumed to be 23% open and have a slot geometry that is 23 mm at a 100 mm pitch. Figure 28 shows the geometry used to represent the field cage plane. The resistance values determined for the field cage planes was 411,000 kg/m^4 and 247 kg/m^3-s for the inertial and viscous coefficients, respectively.

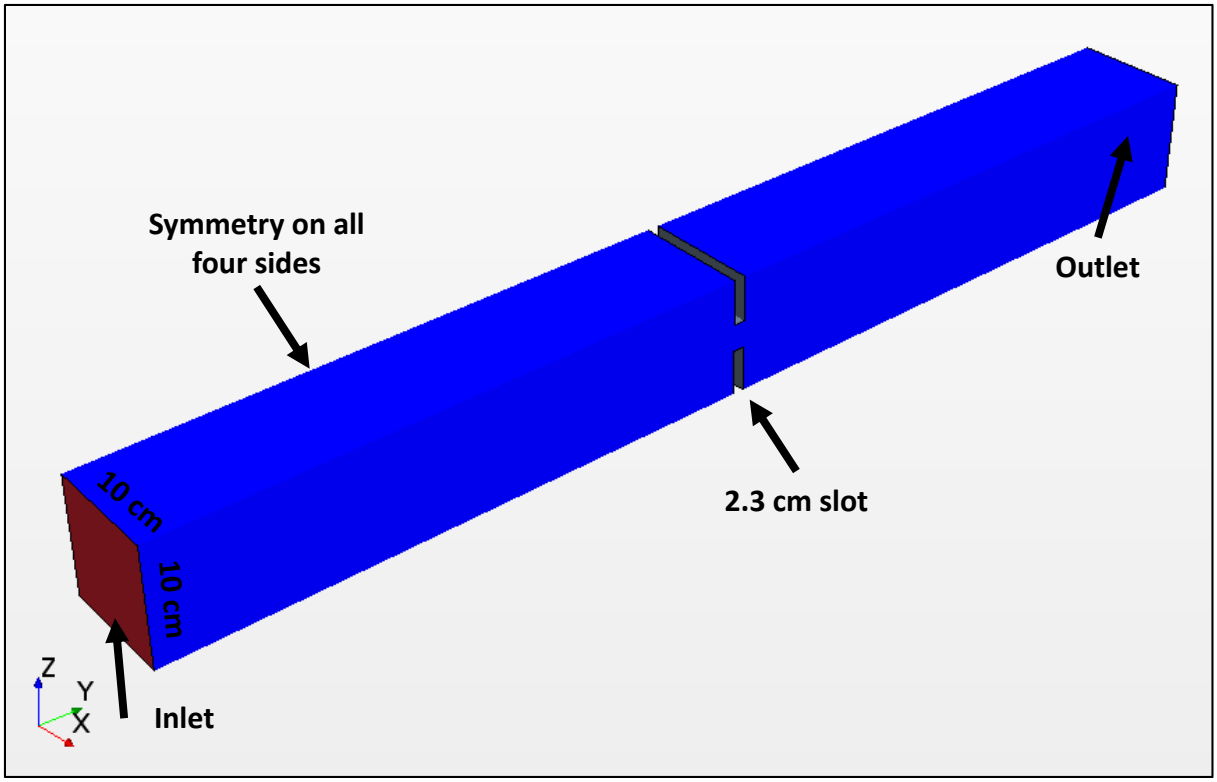

Figure 28: Field cage plane geometry for pressure drop simulation.

Physics Continua

The physics models used in the full LBNF simulation are the same as those used for the 35 Ton cryostat simulation, with the addition of a second physics continua for the solid CPA planes. The solid continua used the physics models listed in Table 7.

Table 7: Physics models used in solid continua.

Physics Model	***Description***
Steady State	The fluid physics continua is steady state, so this must match for the solid continua.
Constant Density	Density change of the solid with temperature is not important, therefore constant density is used.
Segregated Energy	Thermal energy equation for the solid region.

The stainless steel 302 properties used in the simulation are shown in Table 8.

Table 8: Stainless steel 302 properties used in solid continua.

Property	*Value*
Density	8055.0 kg/m^3
Specific Heat	480.0 J/kg-K
Thermal Conductivity	15.1 W/m-k

Mesh Settings

The mesh for the full LBNF simulation contains 34 million cells. The main fluid volume is comprised of polyhedral cells that have an average edge length or base size of 10 cm. The mesh also contains 12 prism layers with an overall thickness of 1 cm to capture the boundary layers on the walls. Figure 29 shows a corner of the mesh and the prism layers along the wall.

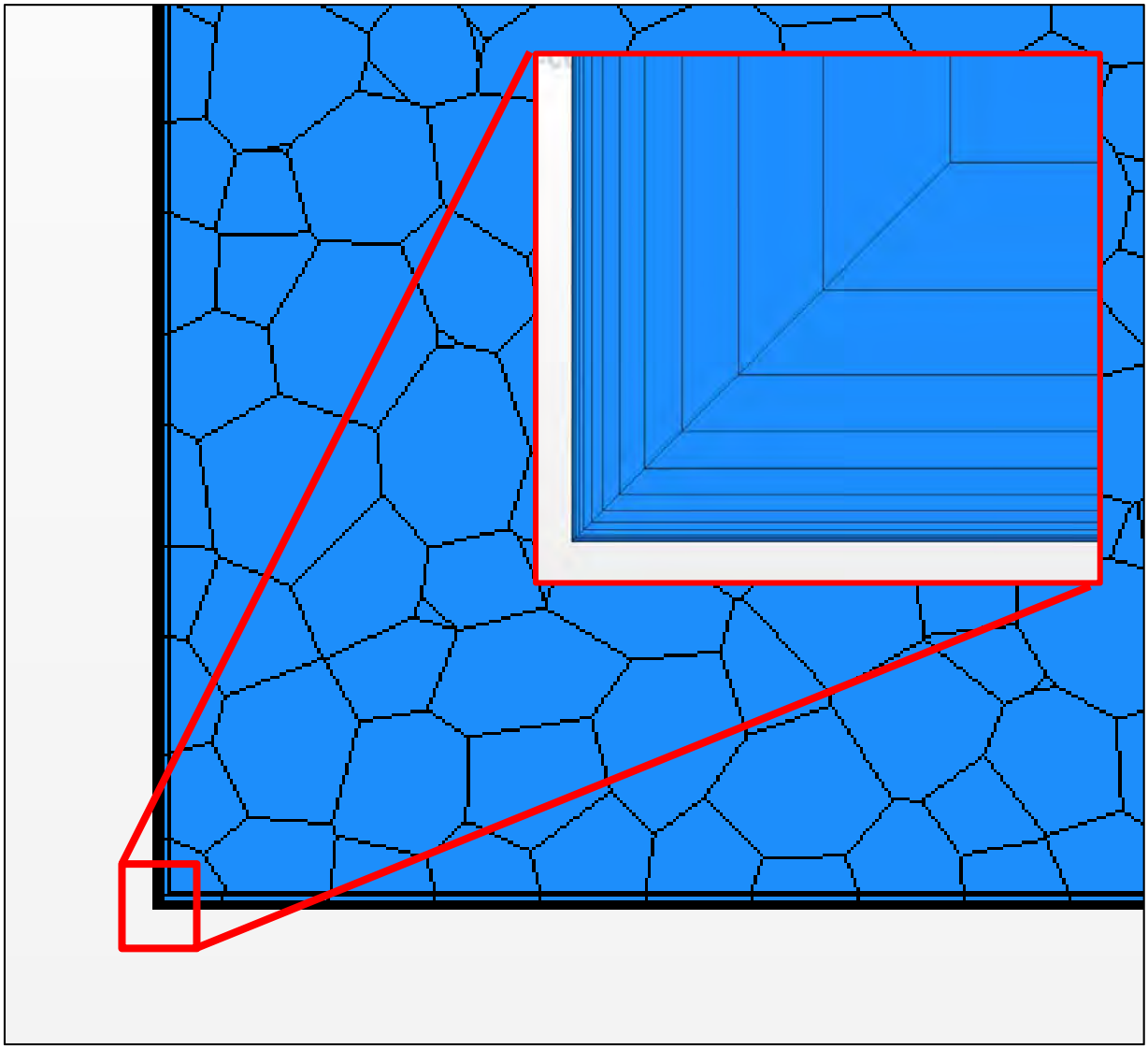

Figure 29: Mesh cross section of full LBNF simulation.

The porous and solid planes used a thin polyhedral mesh with two layers. In the field cage and APA planes, the total plane thickness is 5 cm, therefore the cell thickness is 2.5 cm. The CPA planes are 10 cm thick, therefore the cell thickness is 5 cm. Figure 30 shows a cross section of the CPA and field cage planes.

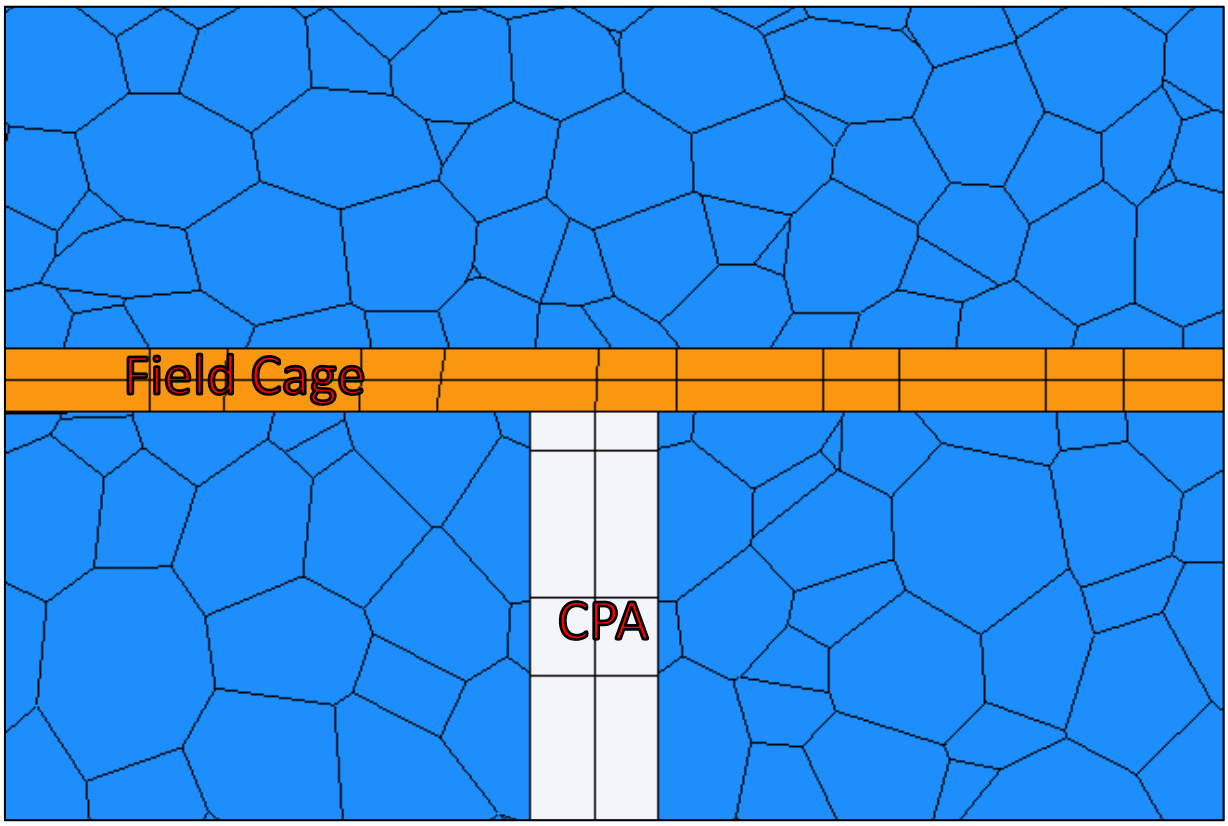

Figure 30: Mesh cross section of CPA and field cage planes.

New Mesh Settings for Latest Design

The original mesh used for the latest design was of the polyhedral type and had approximately 17 million computational cells. The two new meshes have 6 prism layers which is fewer than the original mesh which had 12. The new polyhedral mesh has 8 million cells, and the new trimmed (hexahedral) cell mesh has 16.5 million cells. The goal of the reduced number of cells was to decrease the calculation time to reach a converged solution. Additionally, it was thought that a trimmed cell mesh may further reduce the computational time due to its cells being structured. Below are cross sections of the original polyhedral mesh, new poly mesh, and the new trimmed cell mesh.

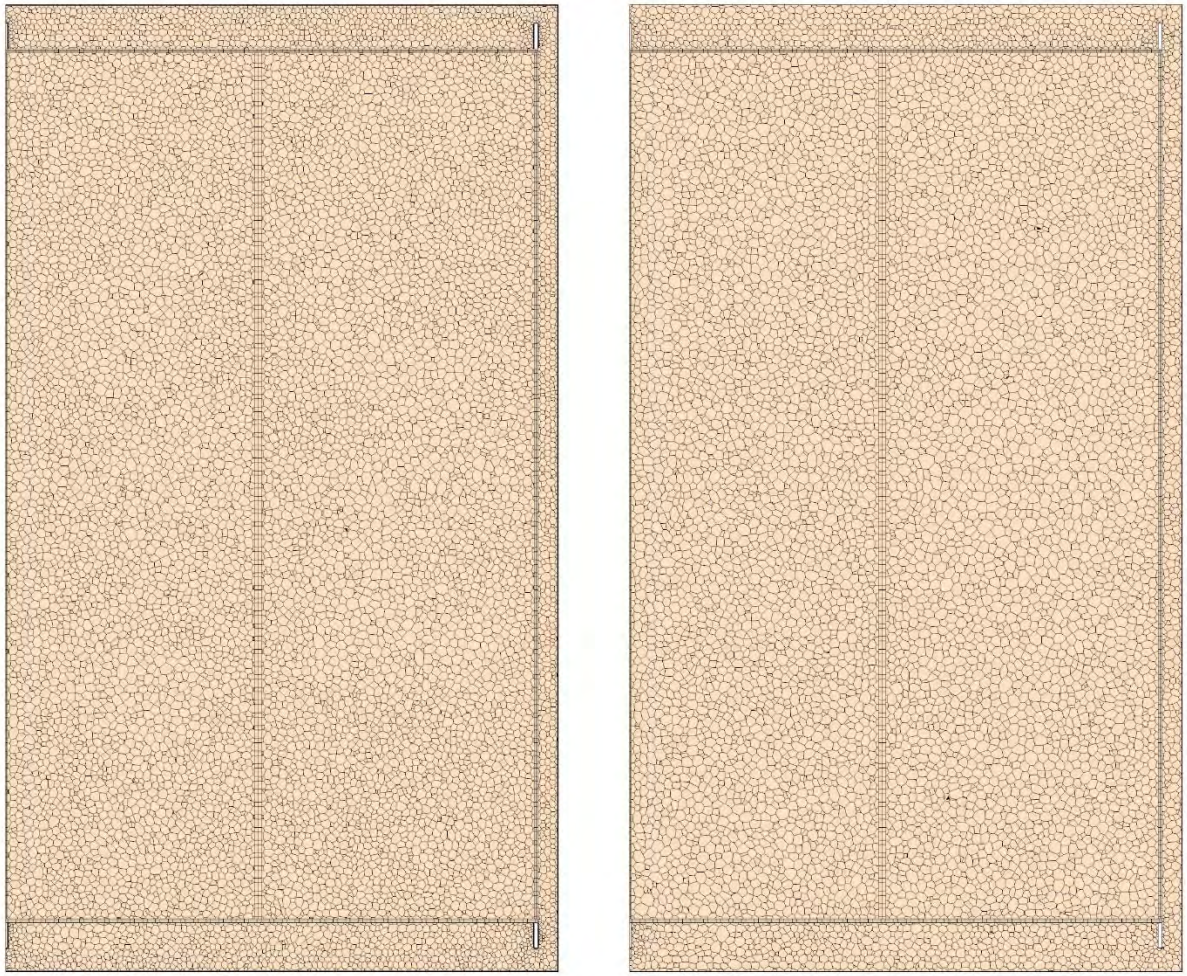

Figure 31: Mesh cross section views of original and new polyhedral meshes, respectively.

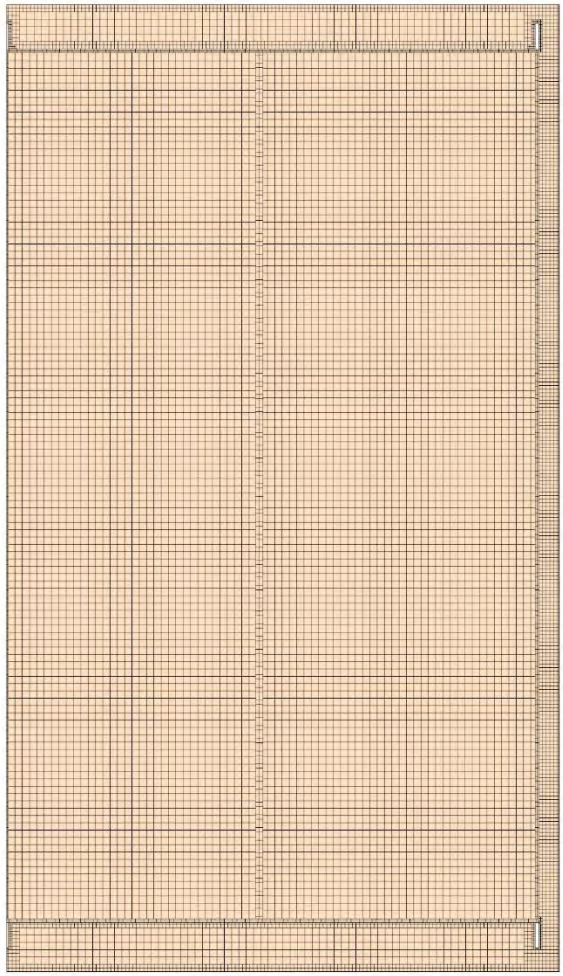

Figure 32: Mesh cross section views of new trimmed (hexahedral) mesh.

Convergence Criteria

The following is an outline of the convergence criteria defined for the LBNF simulations.

- Residuals:
  - Residuals of continuity, x momentum, y momentum, and z momentum should be below 0.01.
- Mass Balance:
  - Less than 1% difference in the mass of argon entering and exiting the cryostat over 1000 iterations. This is not very useful since STAR-CCM+ preserves conservation of mass.
- Temperature:
  - Temperature change in average surface temperature of walls should be less than 0.02 K over 1000 iterations.
  - Inlet and outlet LAr temperatures change by less than 0.05 K over 1000 iterations.

- Passive scalar concentration:
    - The percent difference in the mass of impurities entering and exiting the cryostat should be within 5% difference.
    - The average impurity concentration should not change by more than 0.1% over 1000 iterations.

Passive Scalar Calculations

The impurities were simulated using a passive scalar, which is the same method used on the 35 Ton cryostat simulation. Electron lifetime could be determined from the impurity concentration, but the focus shifted to the standard deviation of the impurities within the field cage. To have comparable calculations between different designs with different levels of concentration, a normalized impurity was defined.

The normalized impurity uses the average impurity concentration within the LAr enclosed by the field cages. The impurity values are divided by the average impurity within the field cage to create the normalized impurity. By dividing by the average impurity, the new average is one. The standard deviation of the normalized impurities within the field cage was of interest, along with the minimum and maximum normalized impurity within the field cage. The minimum and maximum were expressed as a percent difference between the average concentration (which is always one, as mentioned above) and the minimum or maximum value.

$$\text{percent difference} = \frac{\text{minimum} - \text{average}}{\text{average}}$$

DUNE LBNF SIMULATION RESULTS

Below are the results for each simulation. As previously mentioned, the origin is located at the bottom center of the cryostat with the y direction being up, z direction running the length of the cryostat, and x being the width of the cryostat.

Comparison of New Meshes for Latest Design

Impurity Scaled with Velocity Vectors

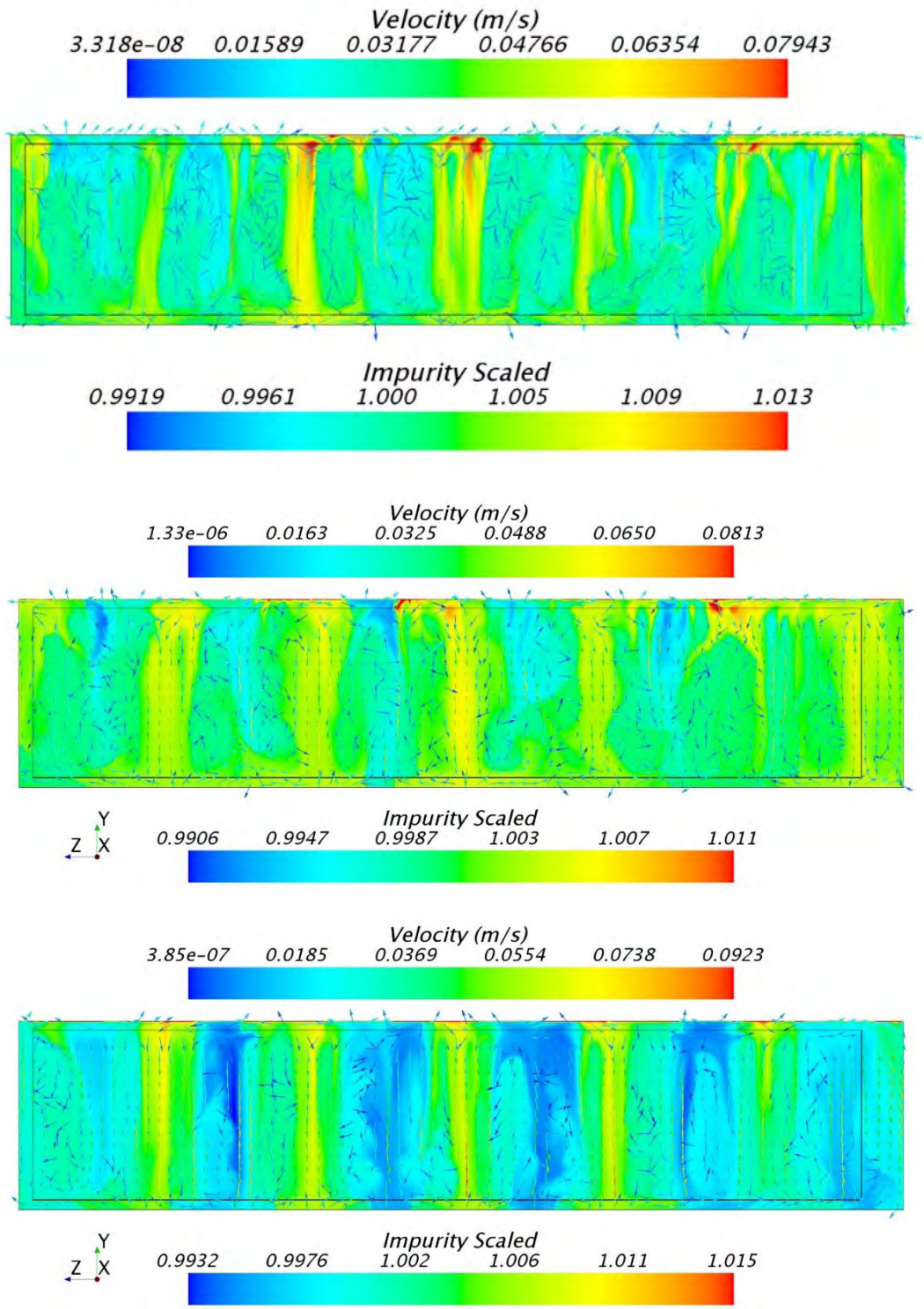

Figure 33. Impurity and velocity vectors at x = 0.1 m for latest design with original poly, new poly, and new trimmed meshes.

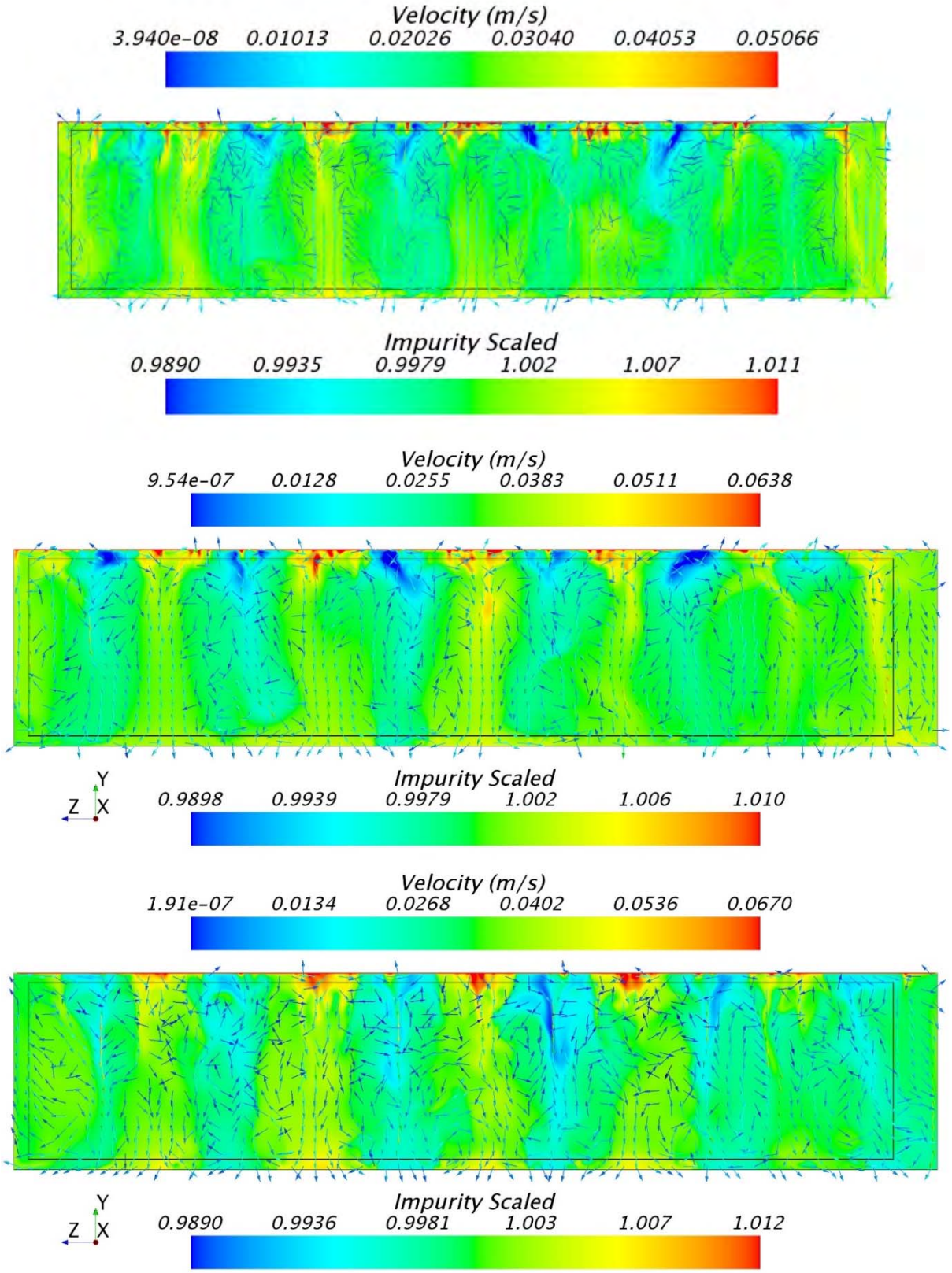

Figure 34. Impurity and velocity vectors at x = 1 m for latest design with original poly, new poly, and new trimmed meshes.

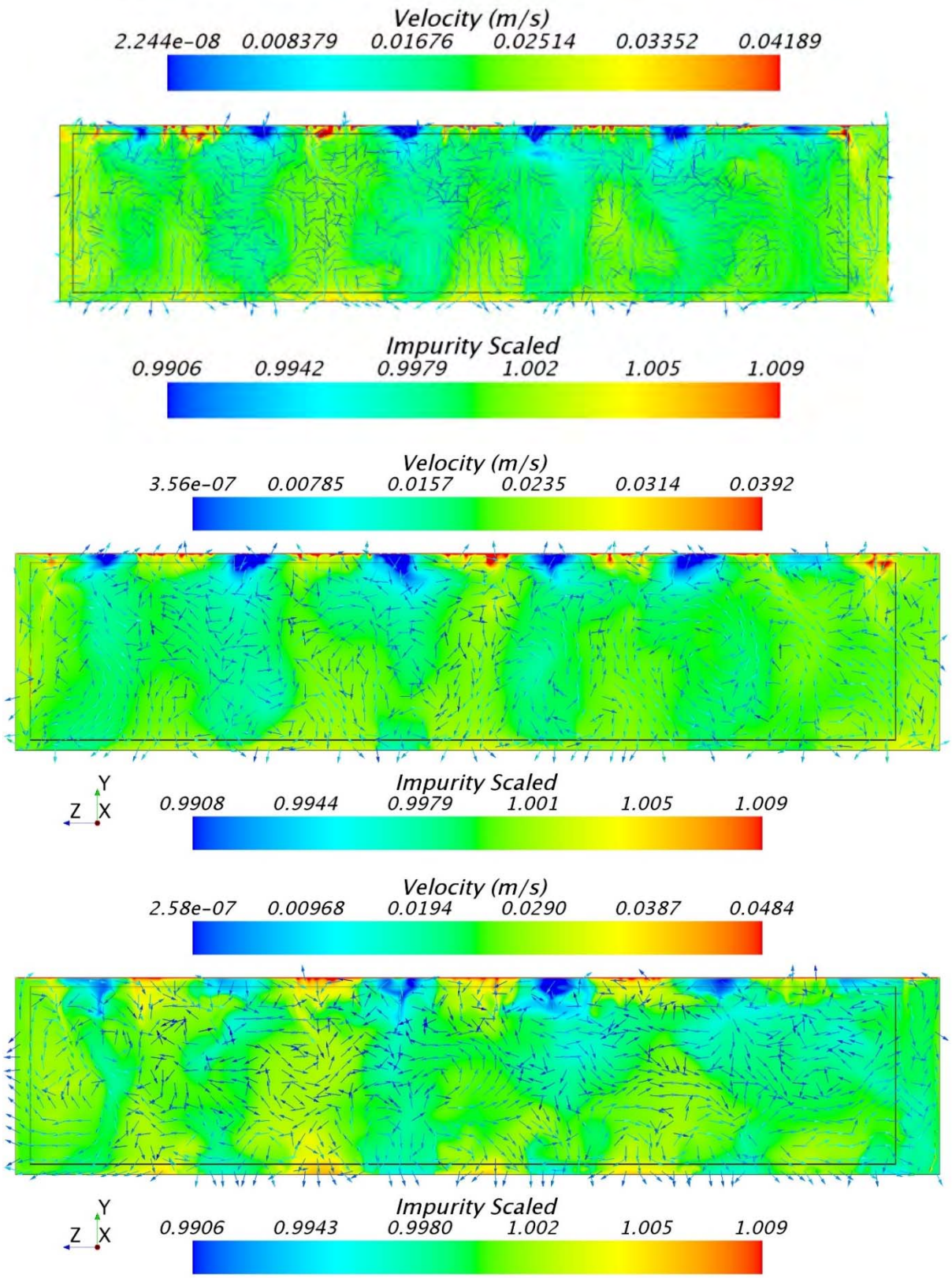

Figure 35. Impurity and velocity vectors at x = 2 m for latest design with original poly, new poly, and new trimmed meshes.

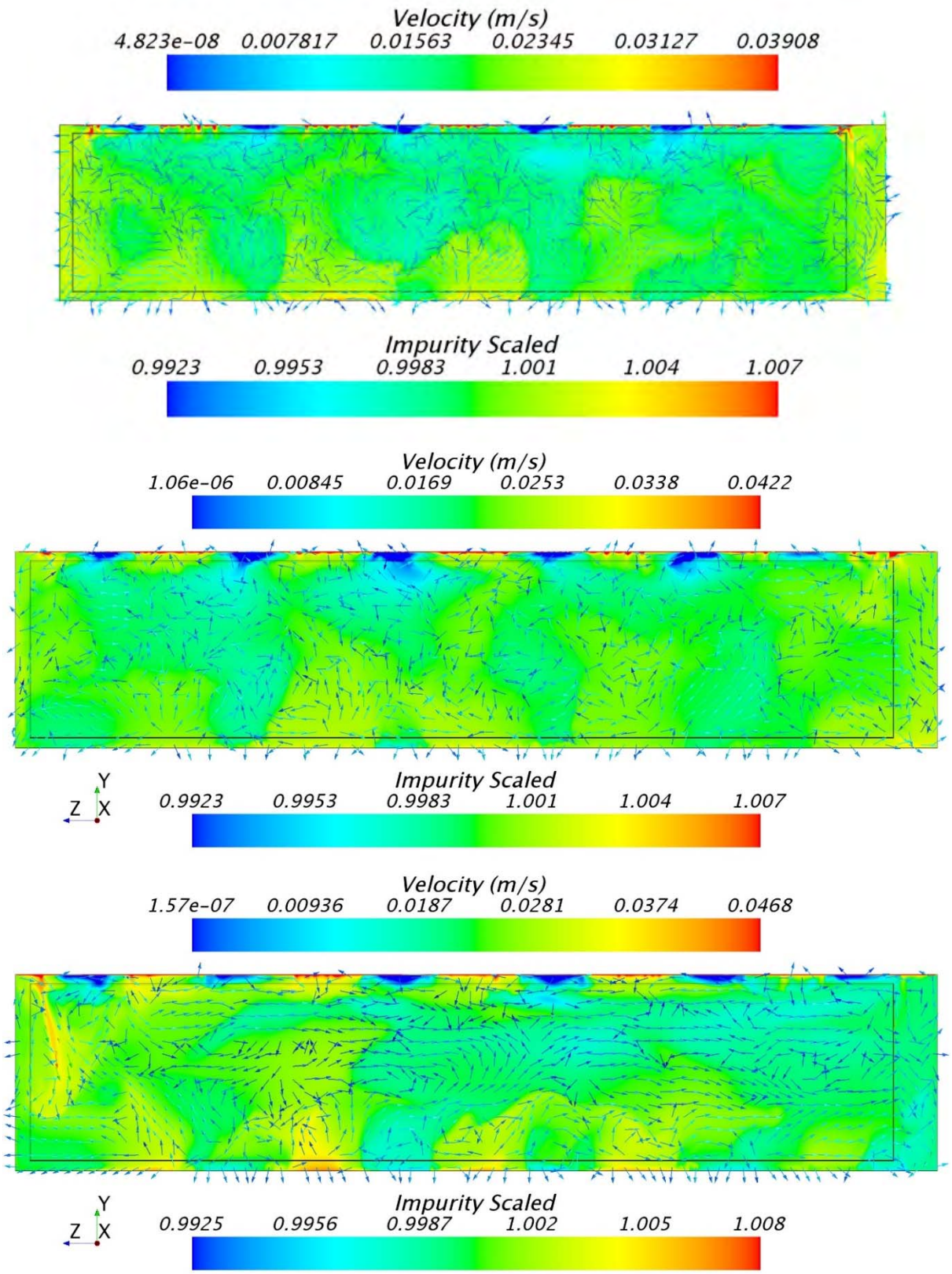

Figure 36. Impurity and velocity vectors at x = 3 m for latest design with original poly, new poly, and new trimmed meshes.

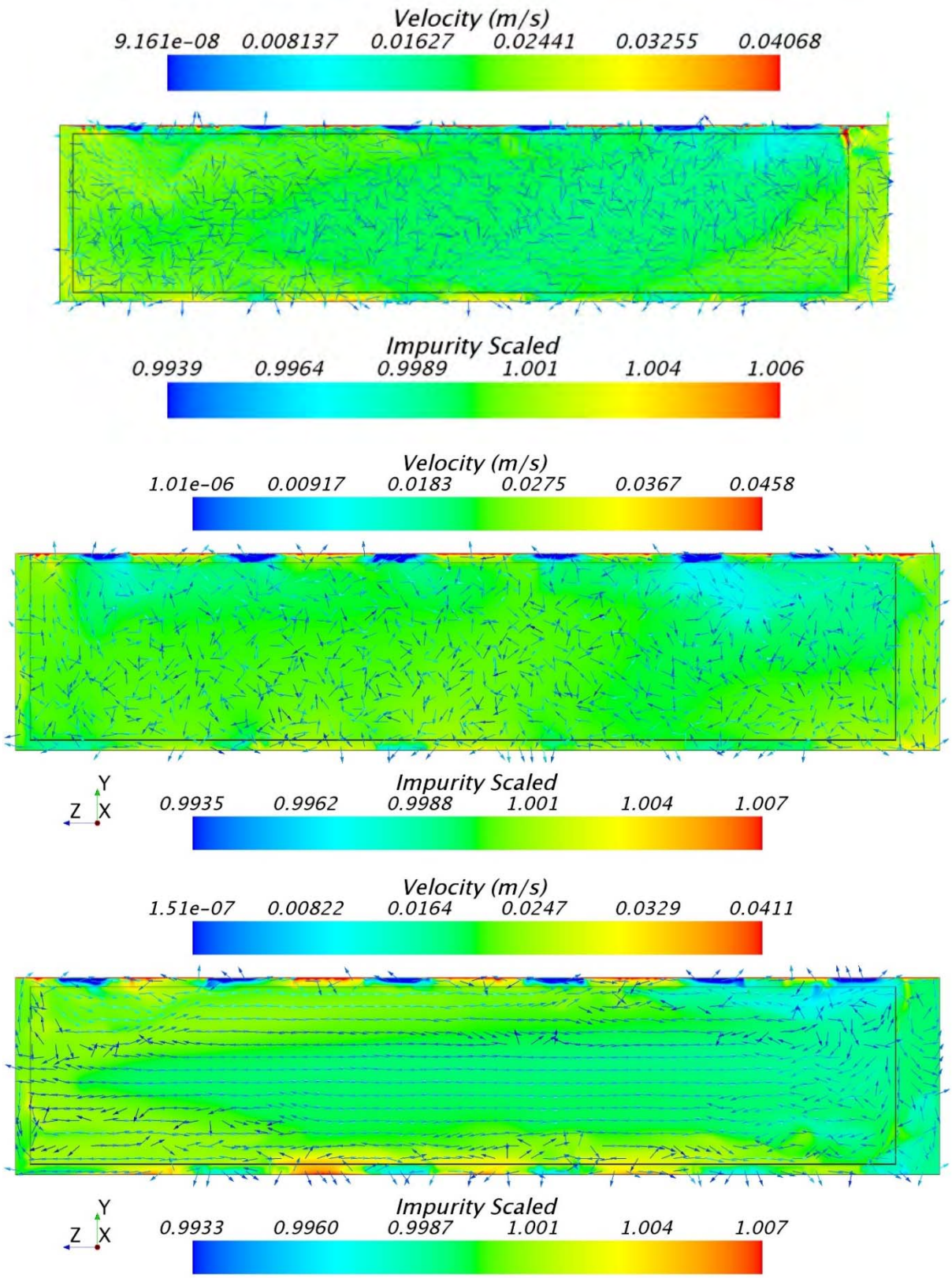

Figure 37. Impurity and velocity vectors at x = 4 m for latest design with original poly, new poly, and new trimmed meshes.

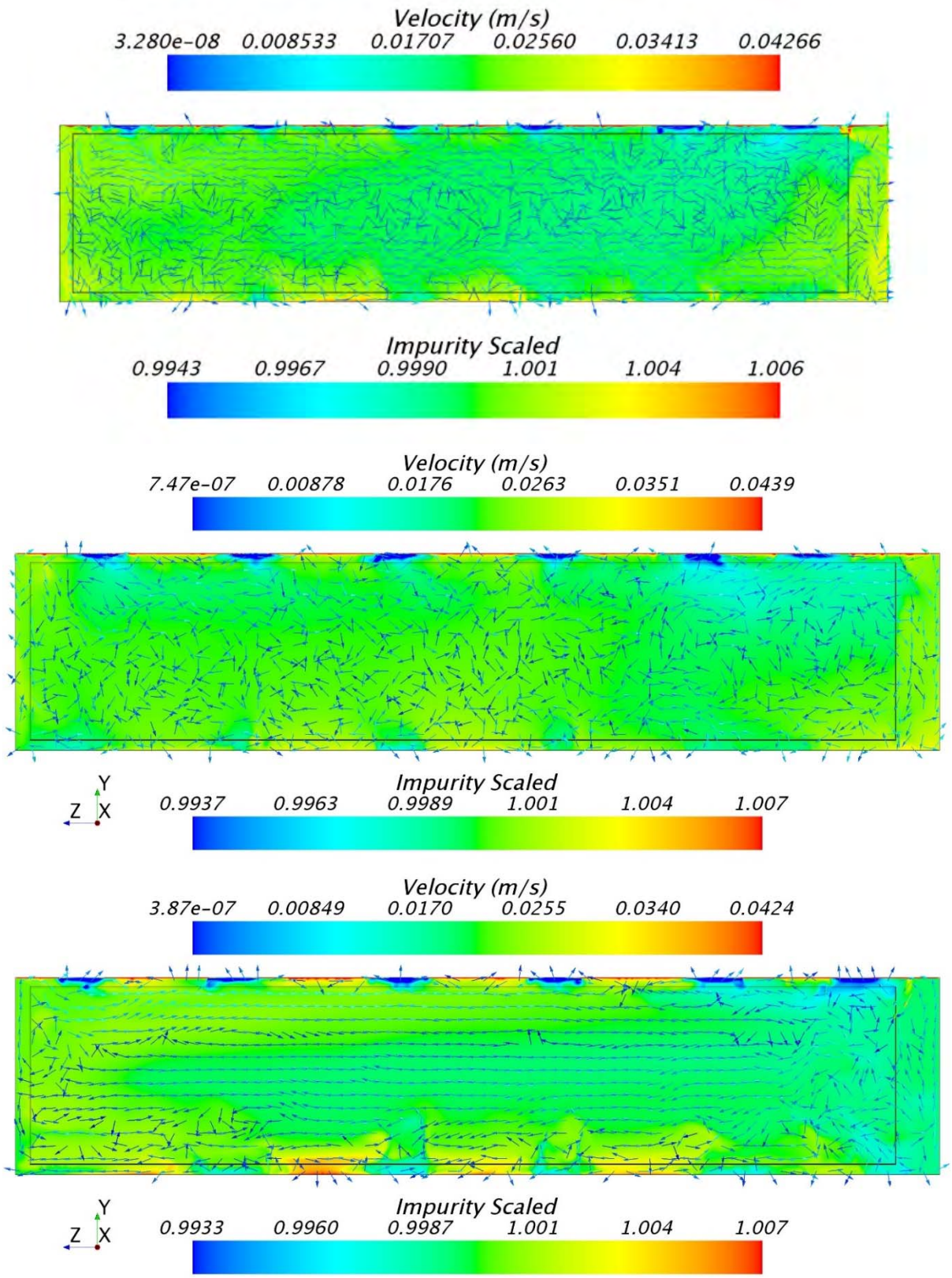

Figure 38. Impurity and velocity vectors at x = 5 m for latest design with original poly, new poly, and new trimmed meshes.

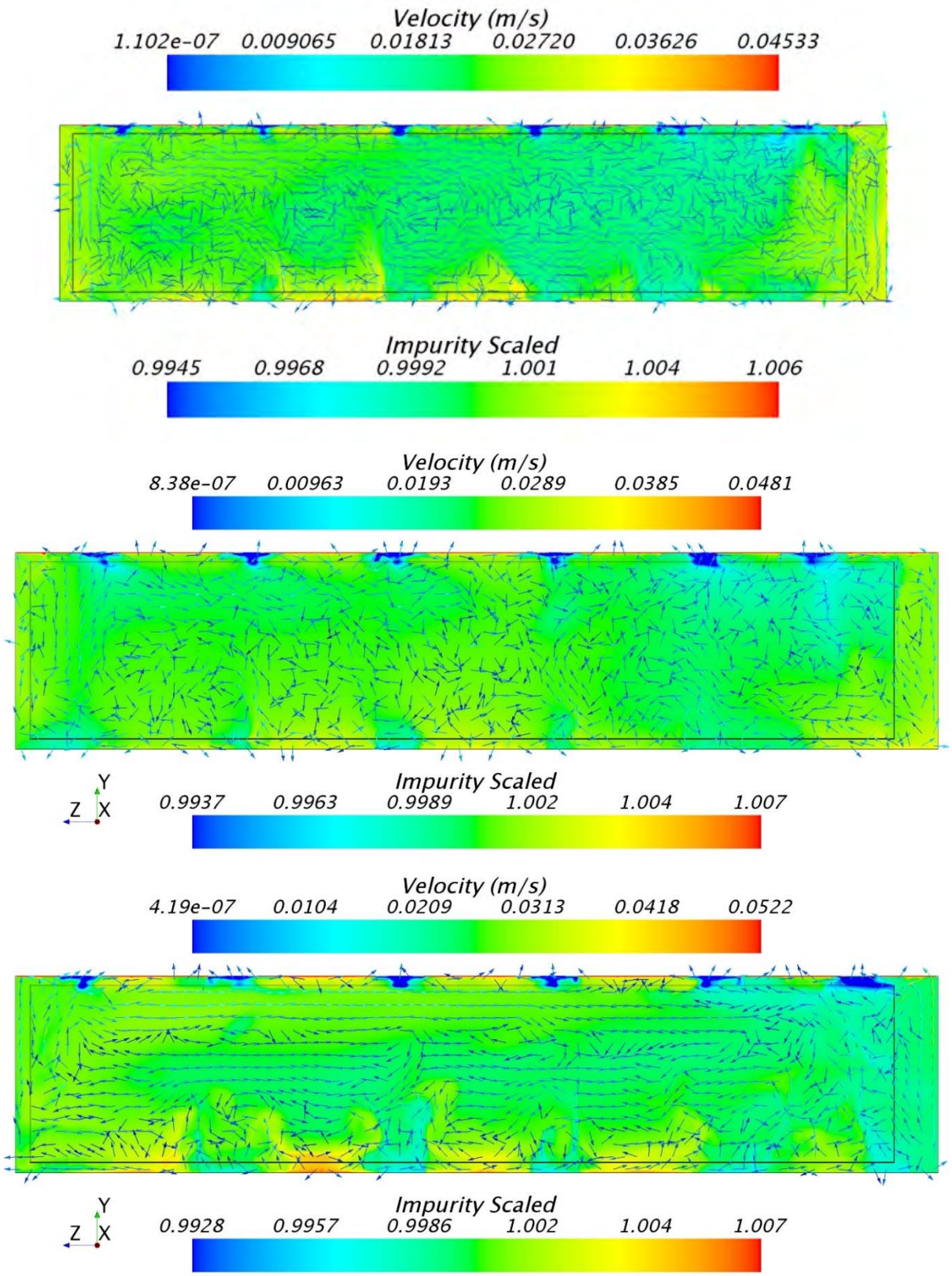

Figure 39. Impurity and velocity vectors at x = 6 m for latest design with original poly, new poly, and new trimmed meshes.

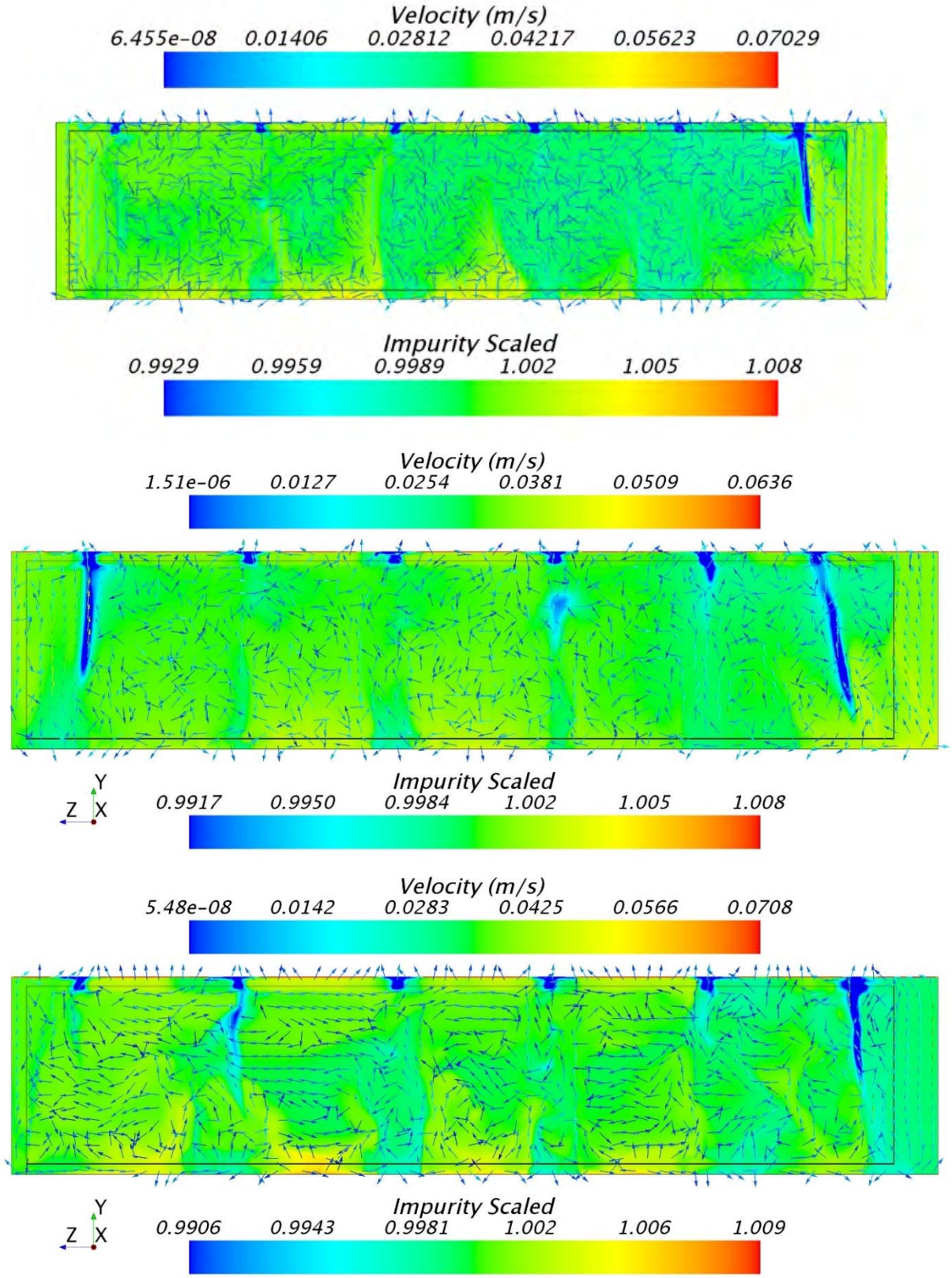

Figure 40. Impurity and velocity vectors at x = 7 m for latest design with original poly, new poly, and new trimmed meshes.

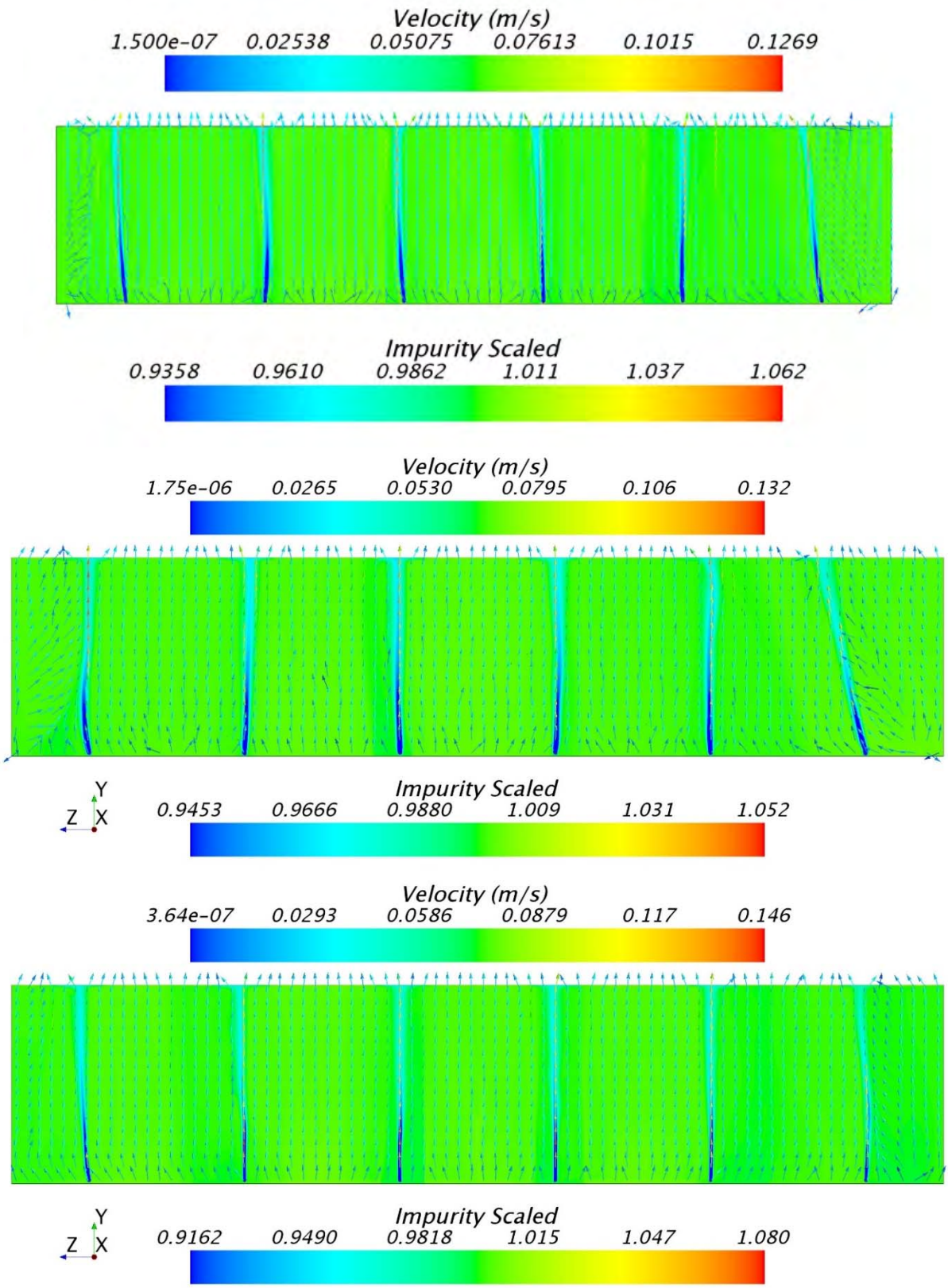

Figure 41. Impurity and velocity vectors at x = 7.4 m for latest design with original poly, new poly, and new trimmed meshes.

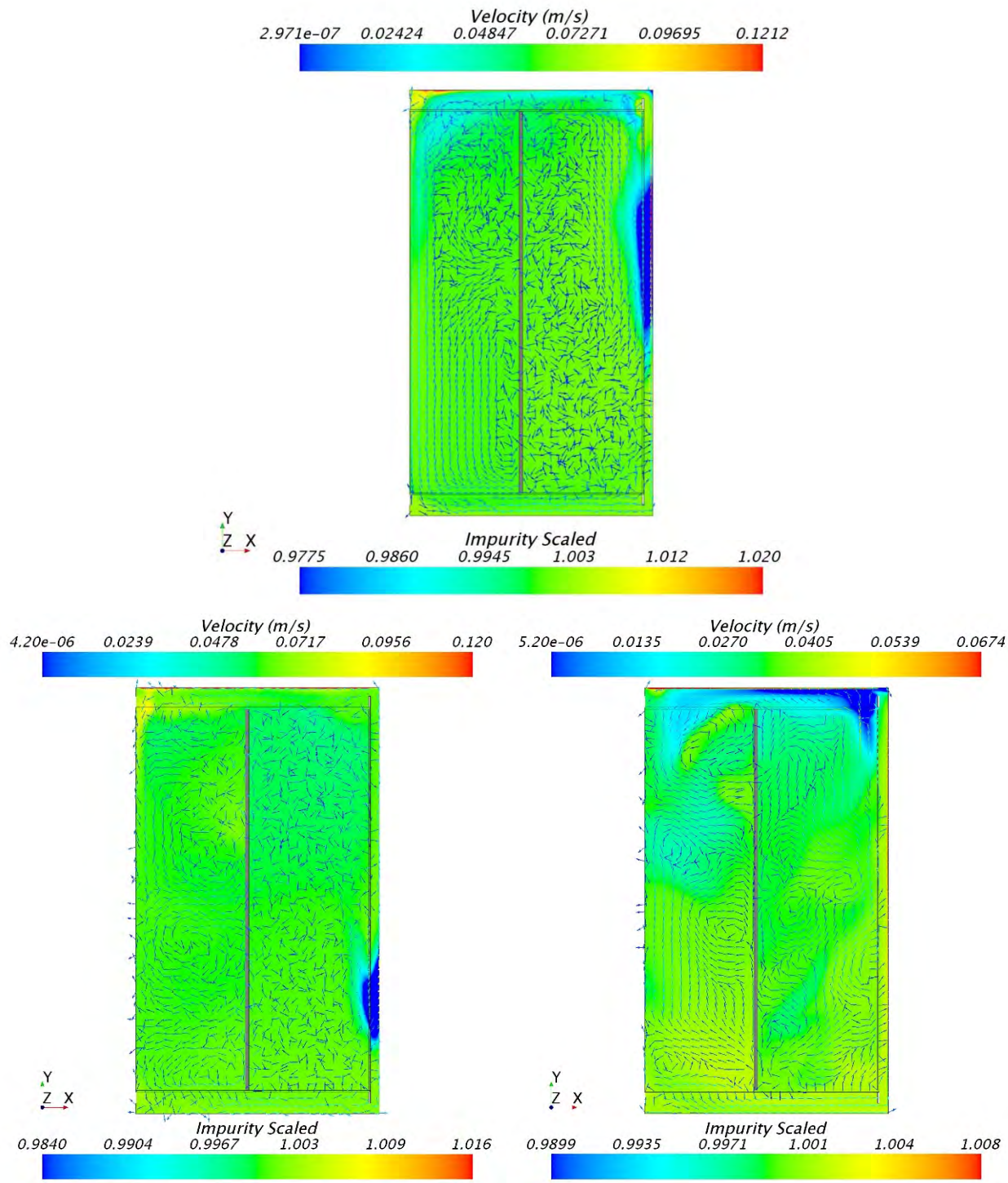

Figure 42. Impurity and velocity vectors at z = -25 m for latest design with original poly, new poly, and new trimmed meshes.

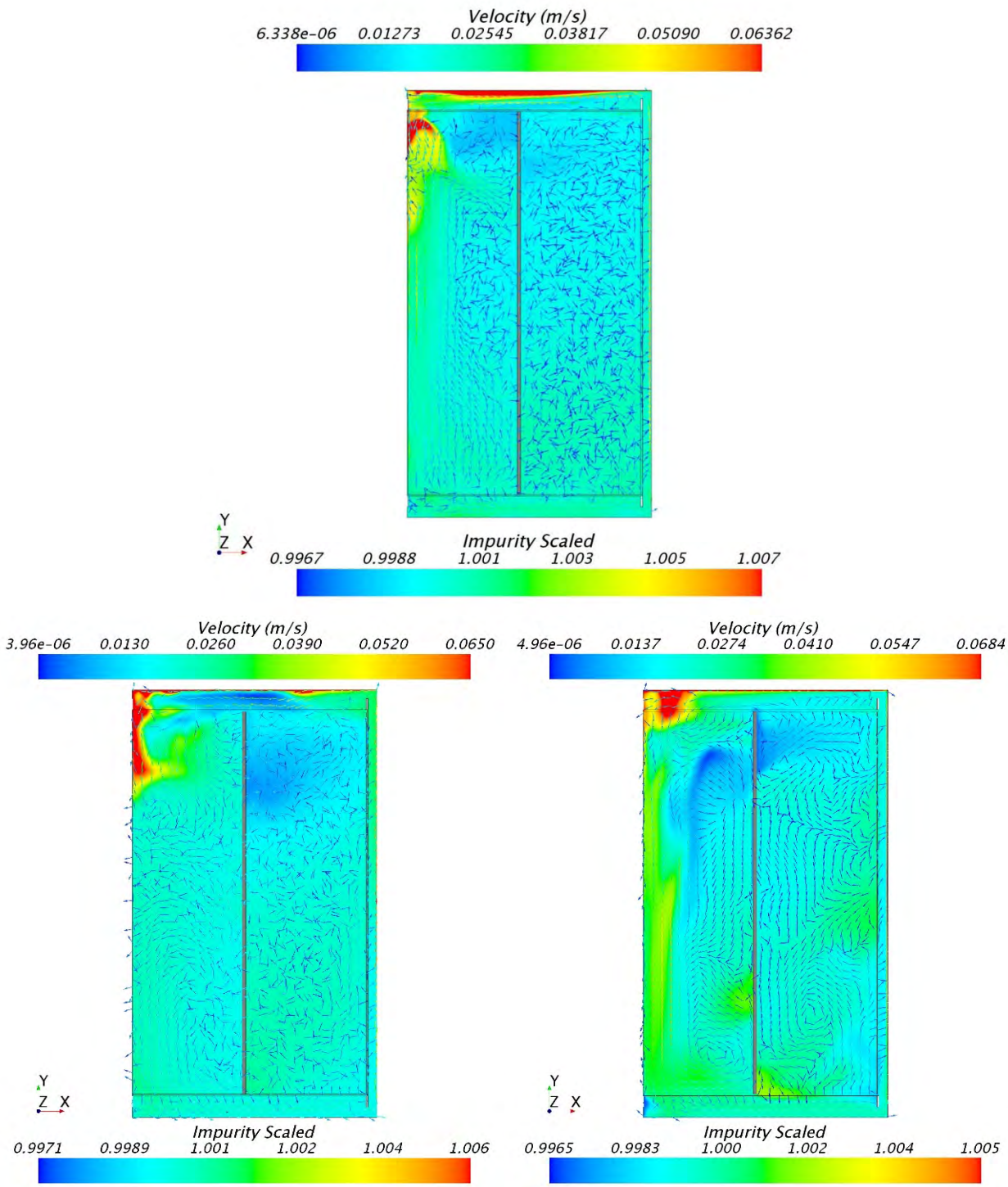

Figure 43. Impurity and velocity vectors at z = -20 m for latest design with original poly, new poly, and new trimmed meshes.

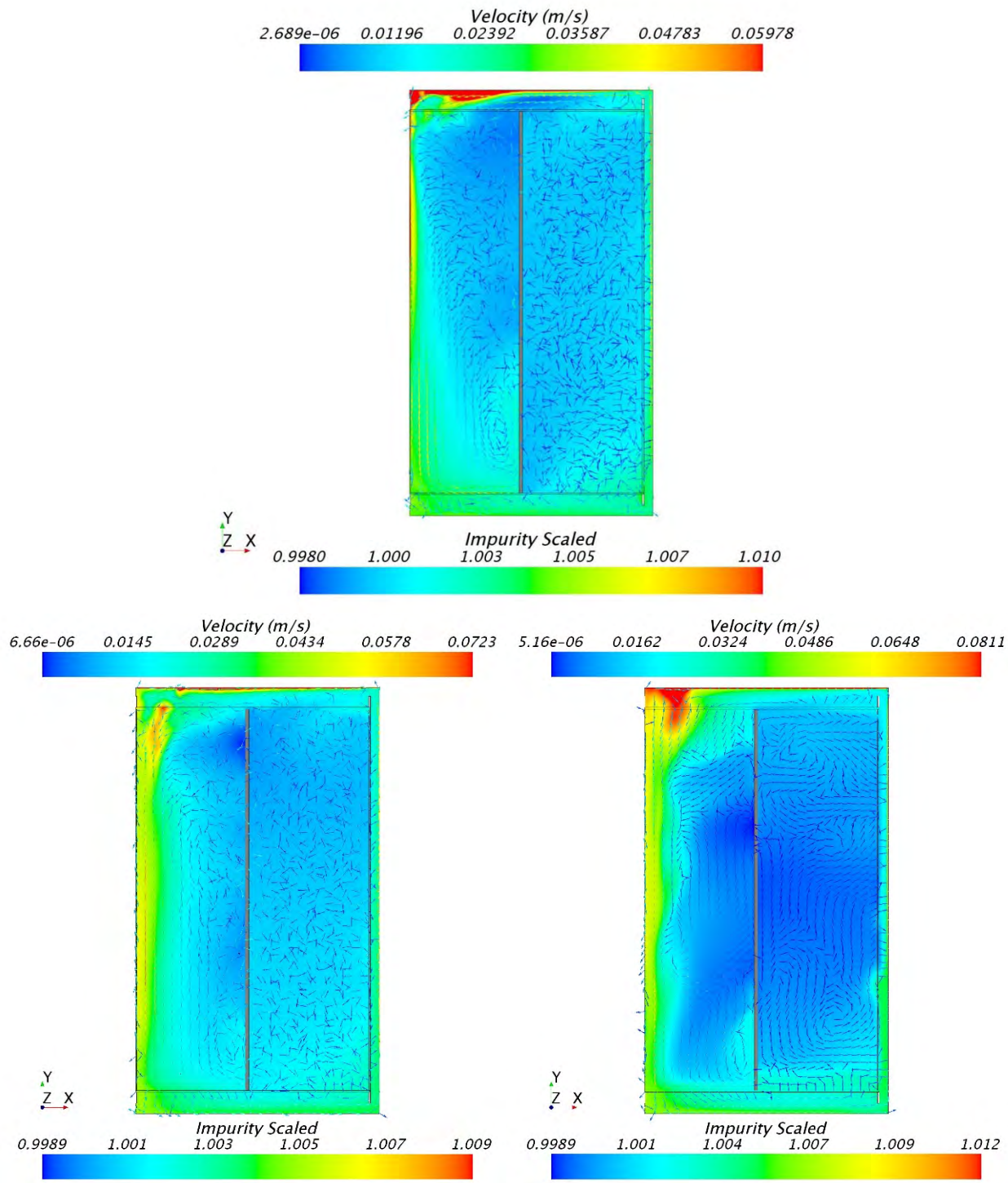

Figure 44. Impurity and velocity vectors at z = 0.0 m for latest design with original poly, new poly, and new trimmed meshes.

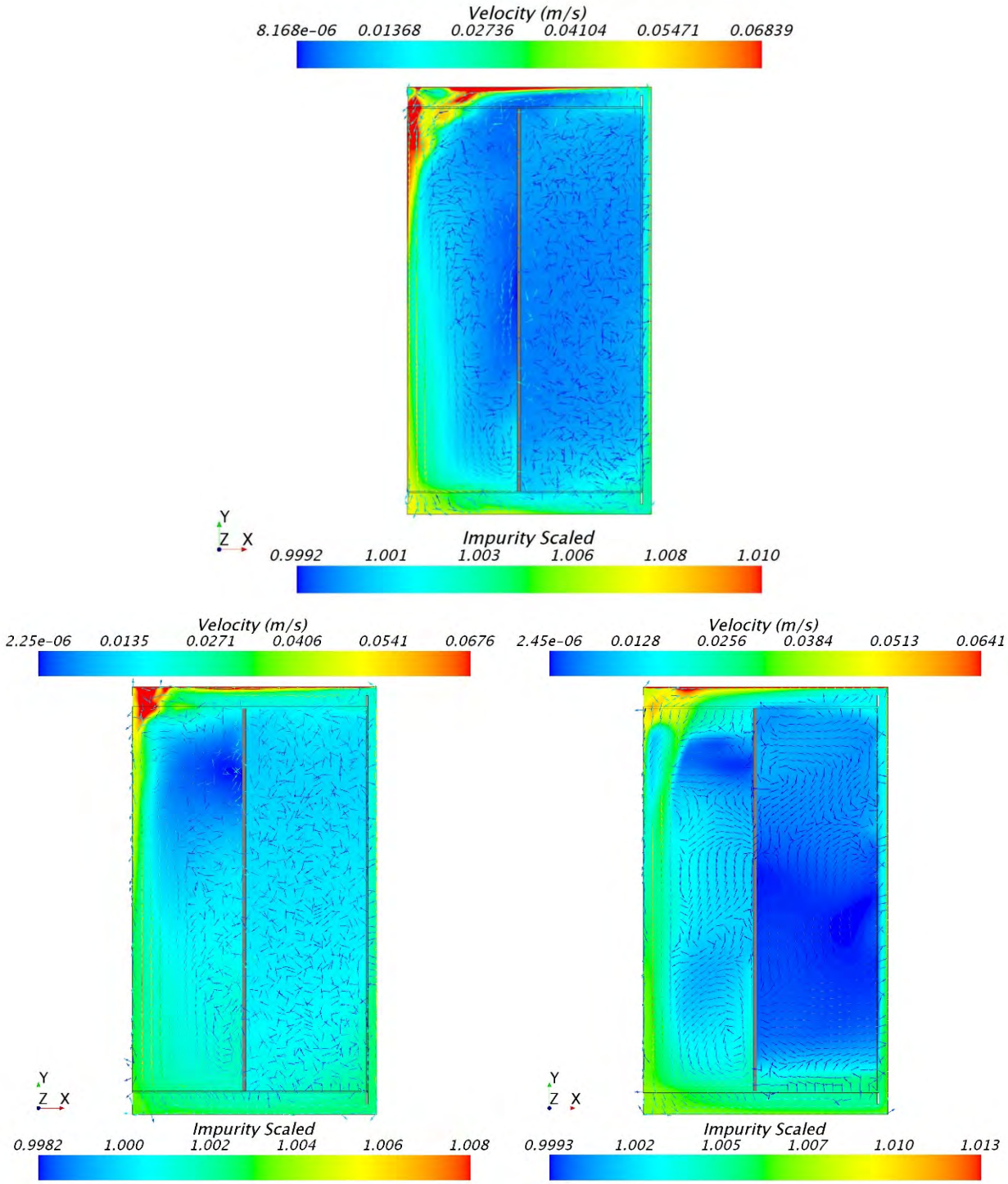

Figure 45. Impurity and velocity vectors at z = 10 m for latest design with original poly, new poly, and new trimmed meshes.

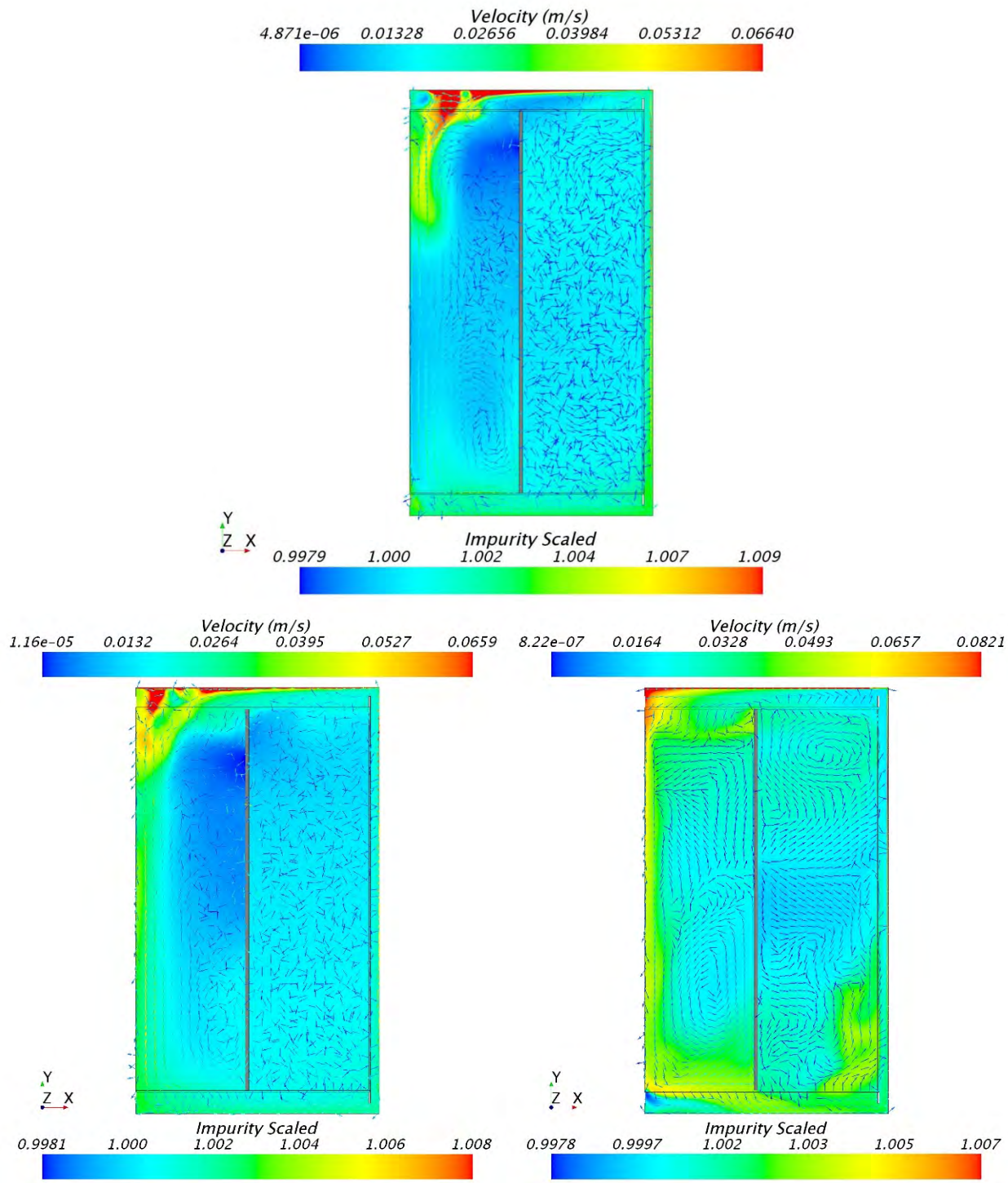

Figure 46. Impurity and velocity vectors at z = 20 m for latest design with original poly, new poly, and new trimmed meshes.

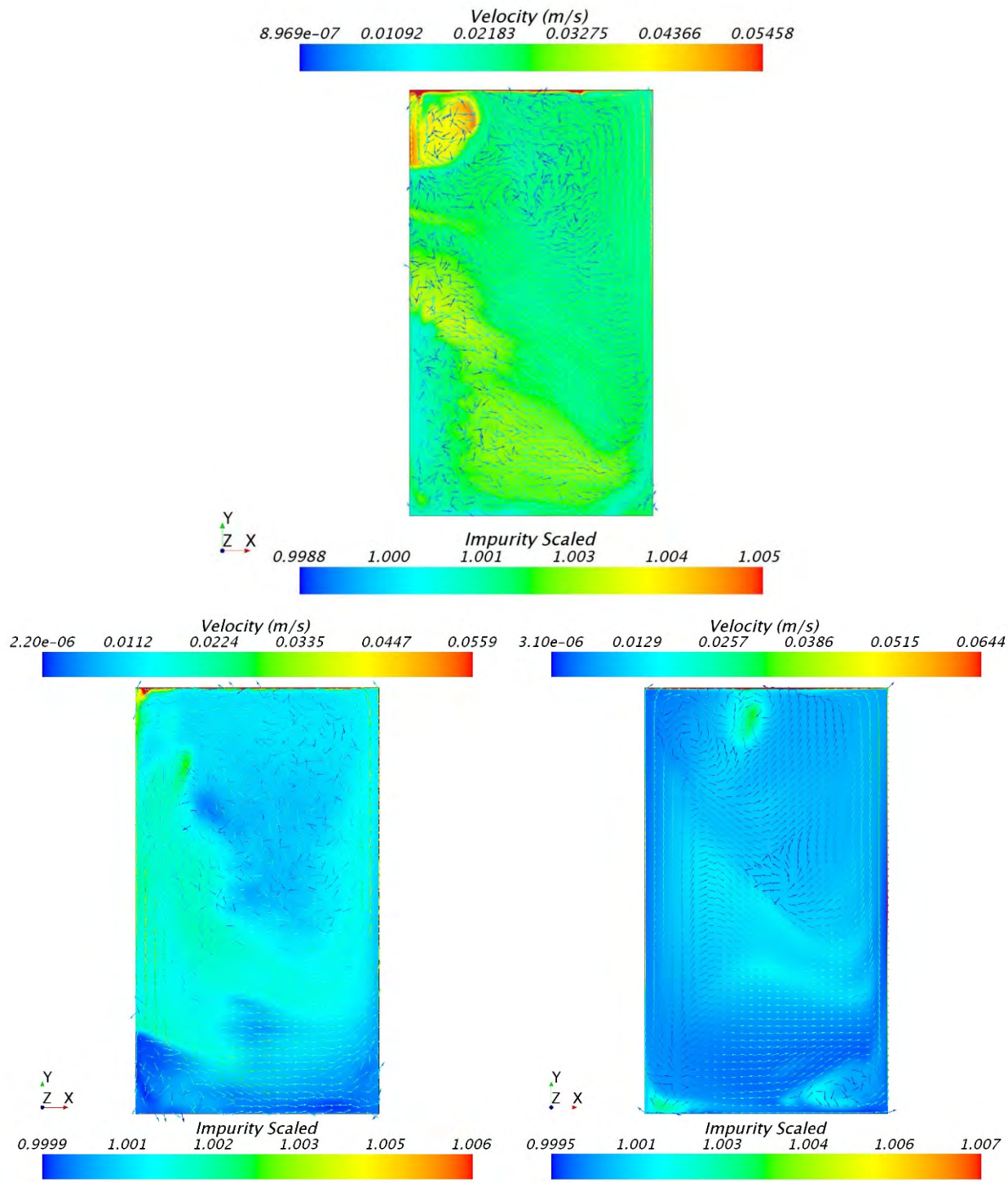

Figure 47. Impurity and velocity vectors at z = 30.5 m for latest design with original poly, new poly, and new trimmed meshes.

Temperature with Velocity Vectors

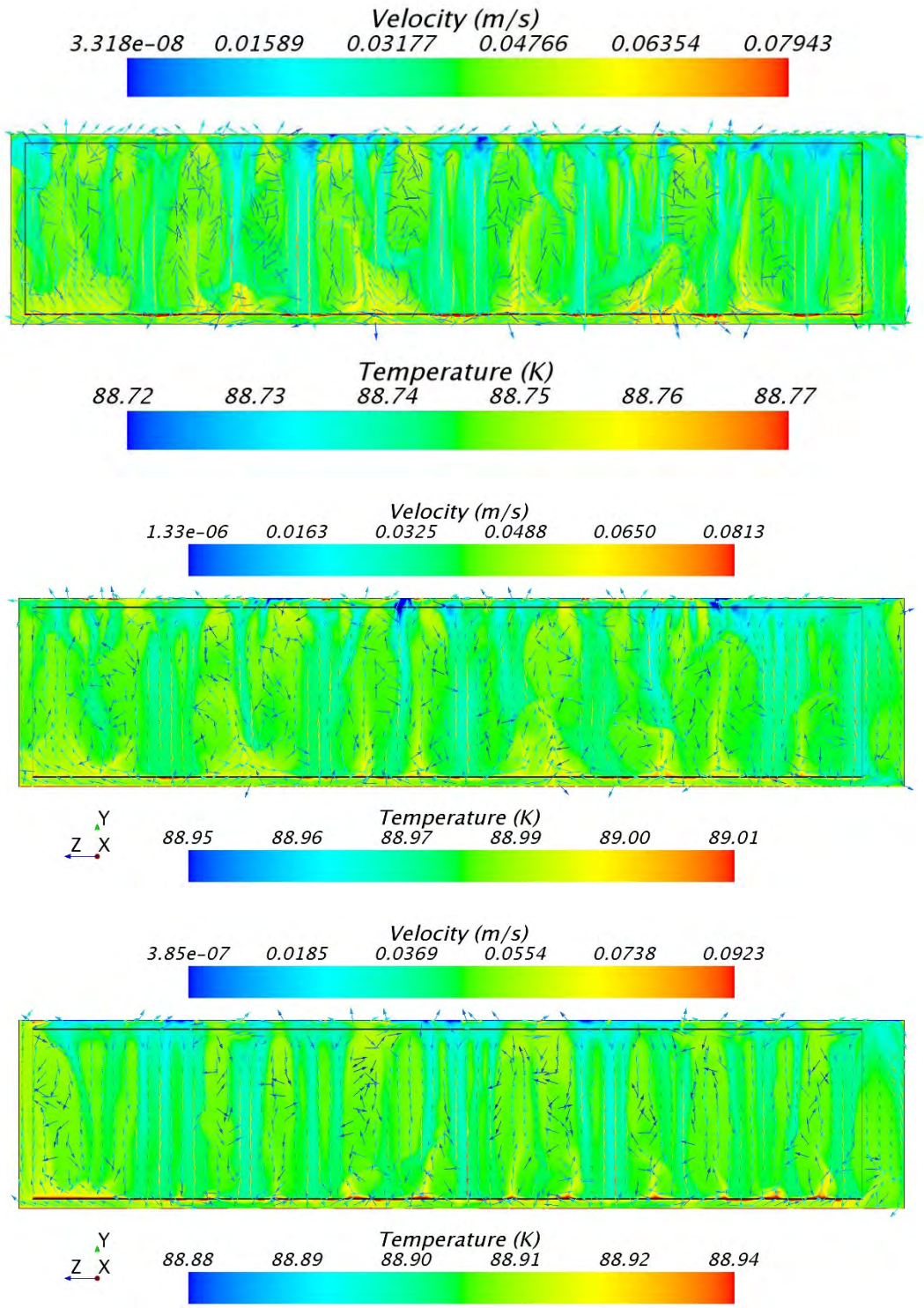

Figure 48. Temperature and velocity vectors at x = 0.1 m for latest design with original poly, new poly, and new trimmed meshes.

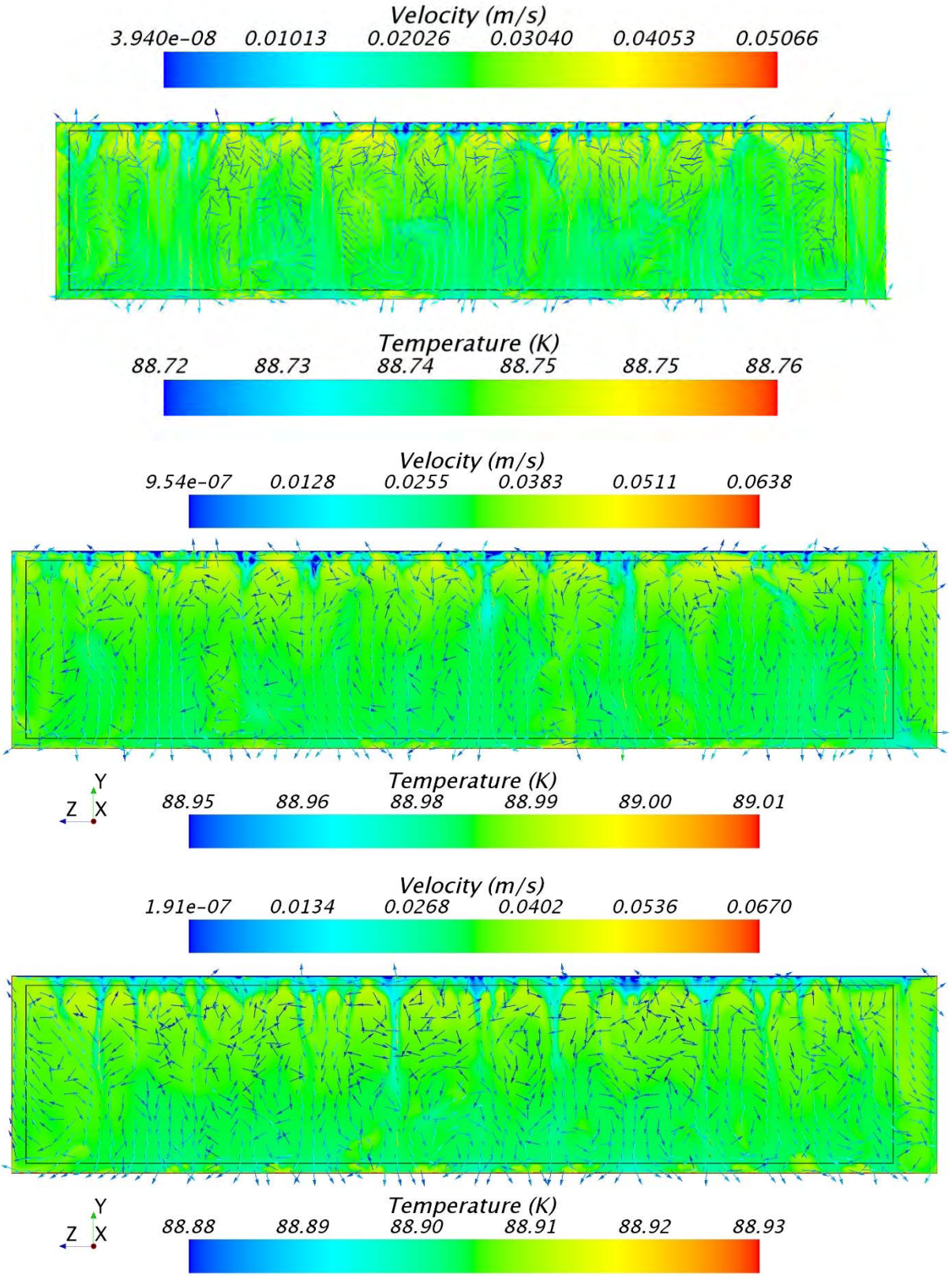

Figure 49. Temperature and velocity vectors at x = 1 m for latest design with original poly, new poly, and new trimmed meshes.

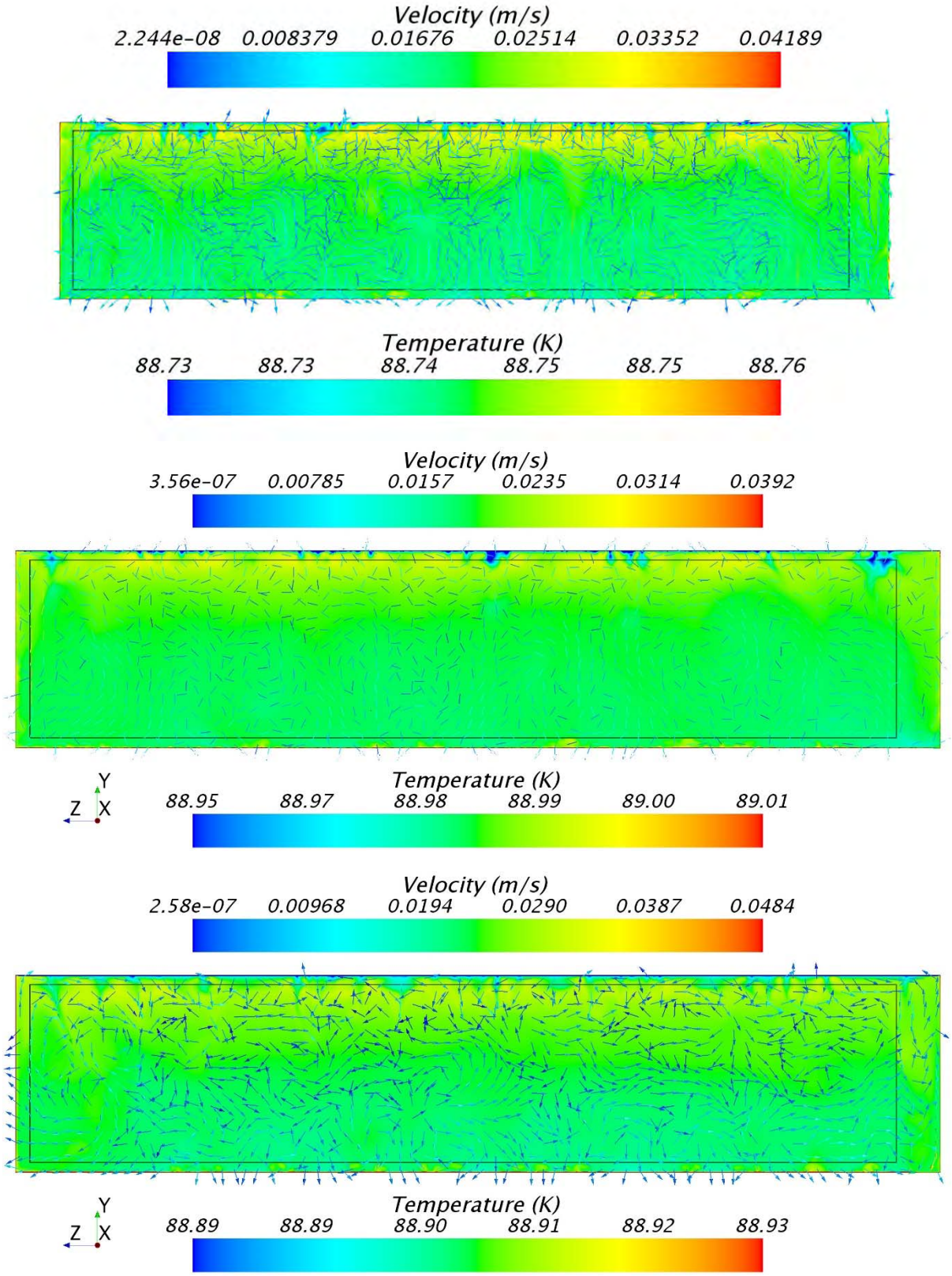

Figure 50. Temperature and velocity vectors at x = 2 m for latest design with original poly, new poly, and new trimmed meshes.

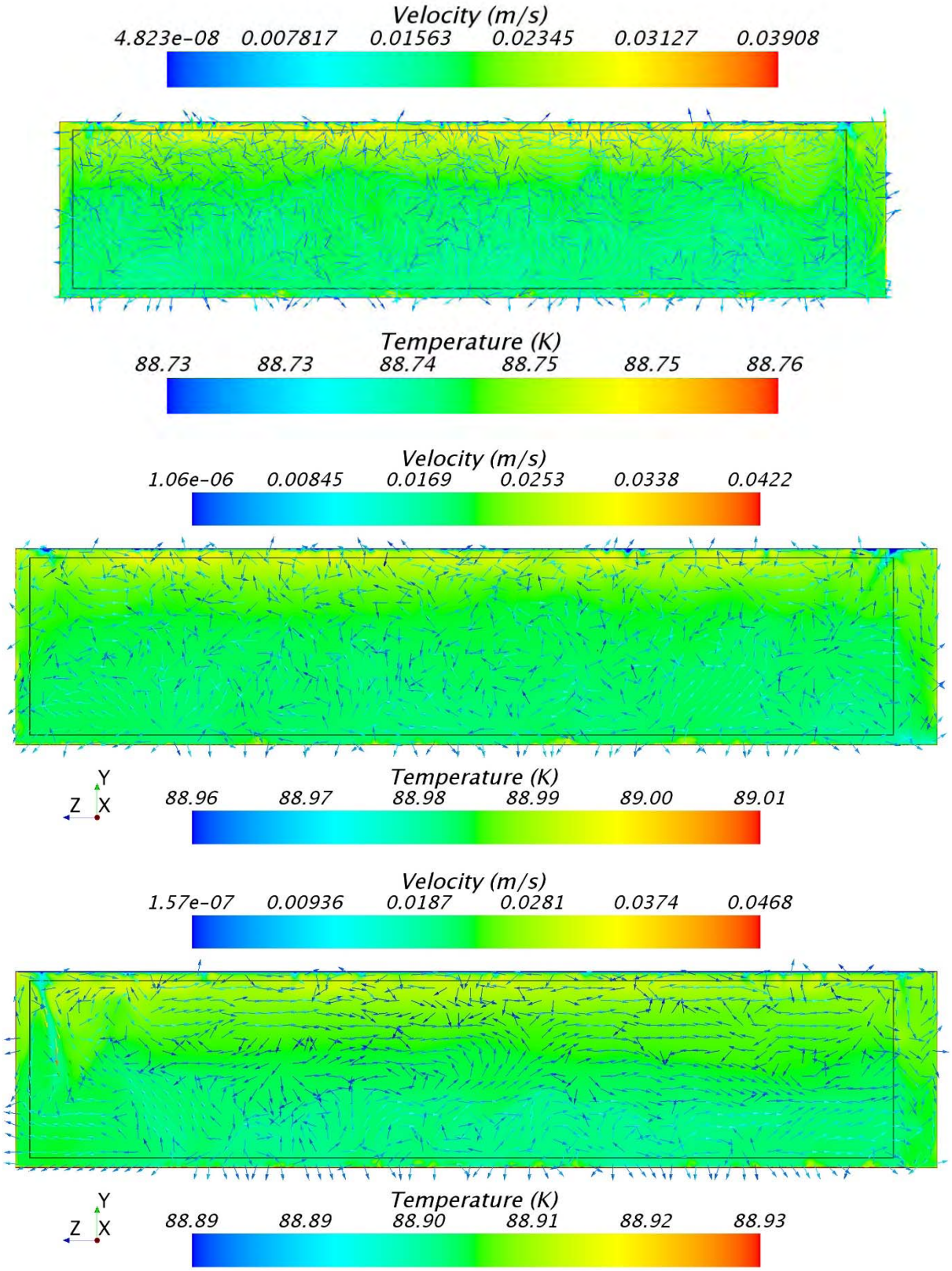

Figure 51. Temperature and velocity vectors at x = 3 m for latest design with original poly, new poly, and new trimmed meshes.

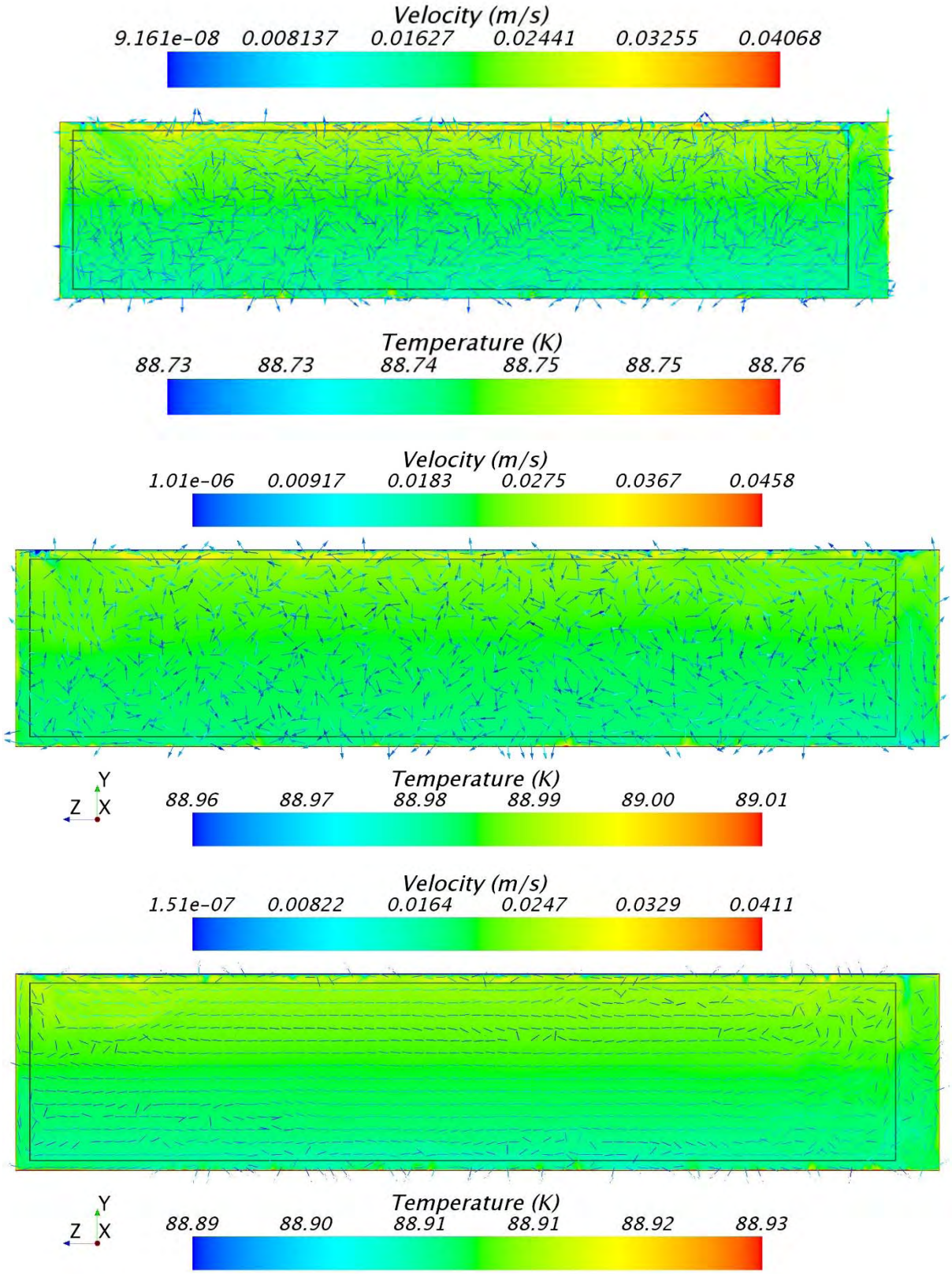

Figure 52. Temperature and velocity vectors at x = 4 m for latest design with original poly, new poly, and new trimmed meshes.

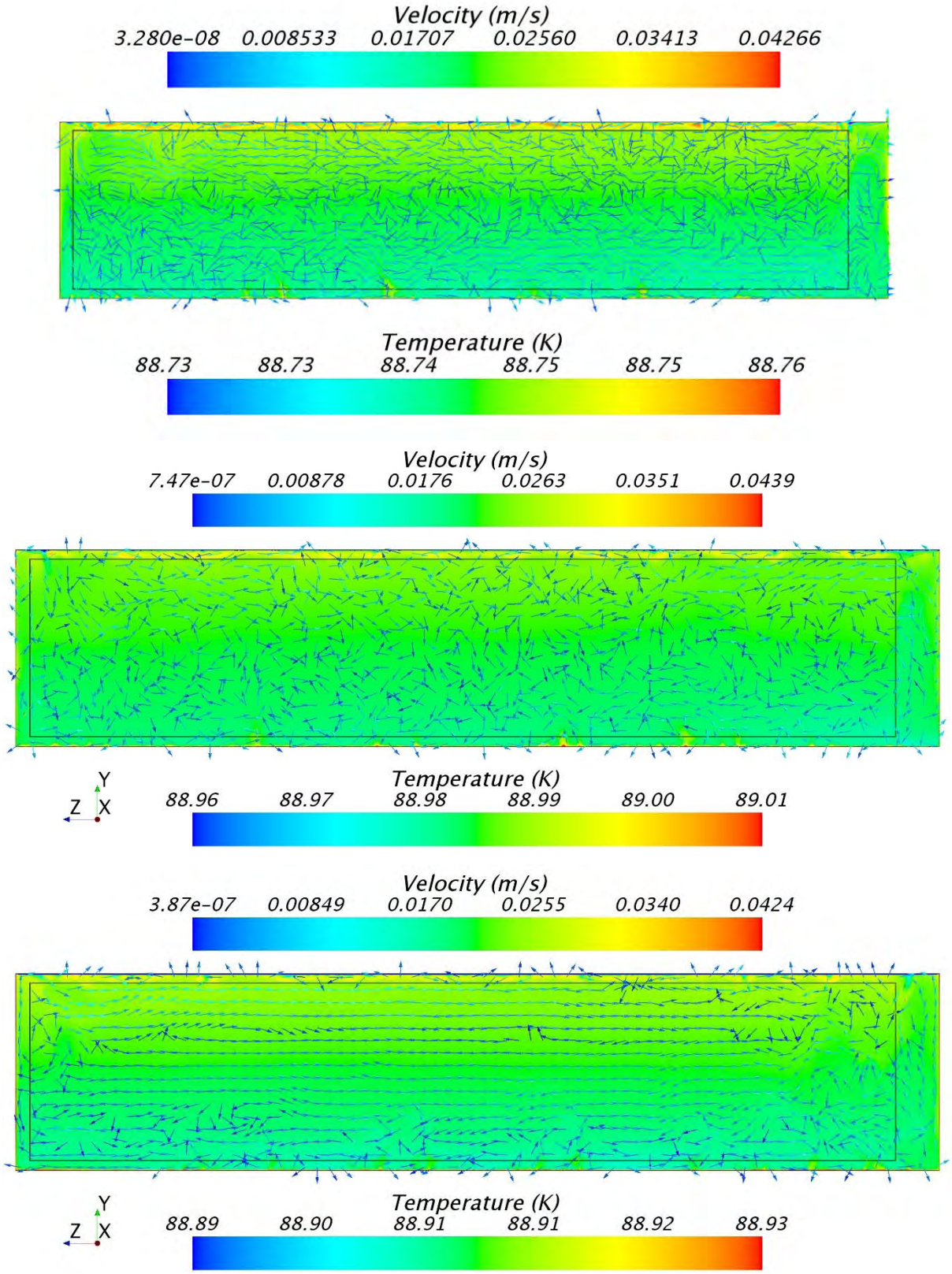

Figure 53. Temperature and velocity vectors at x = 5 m for latest design with original poly, new poly, and new trimmed meshes.

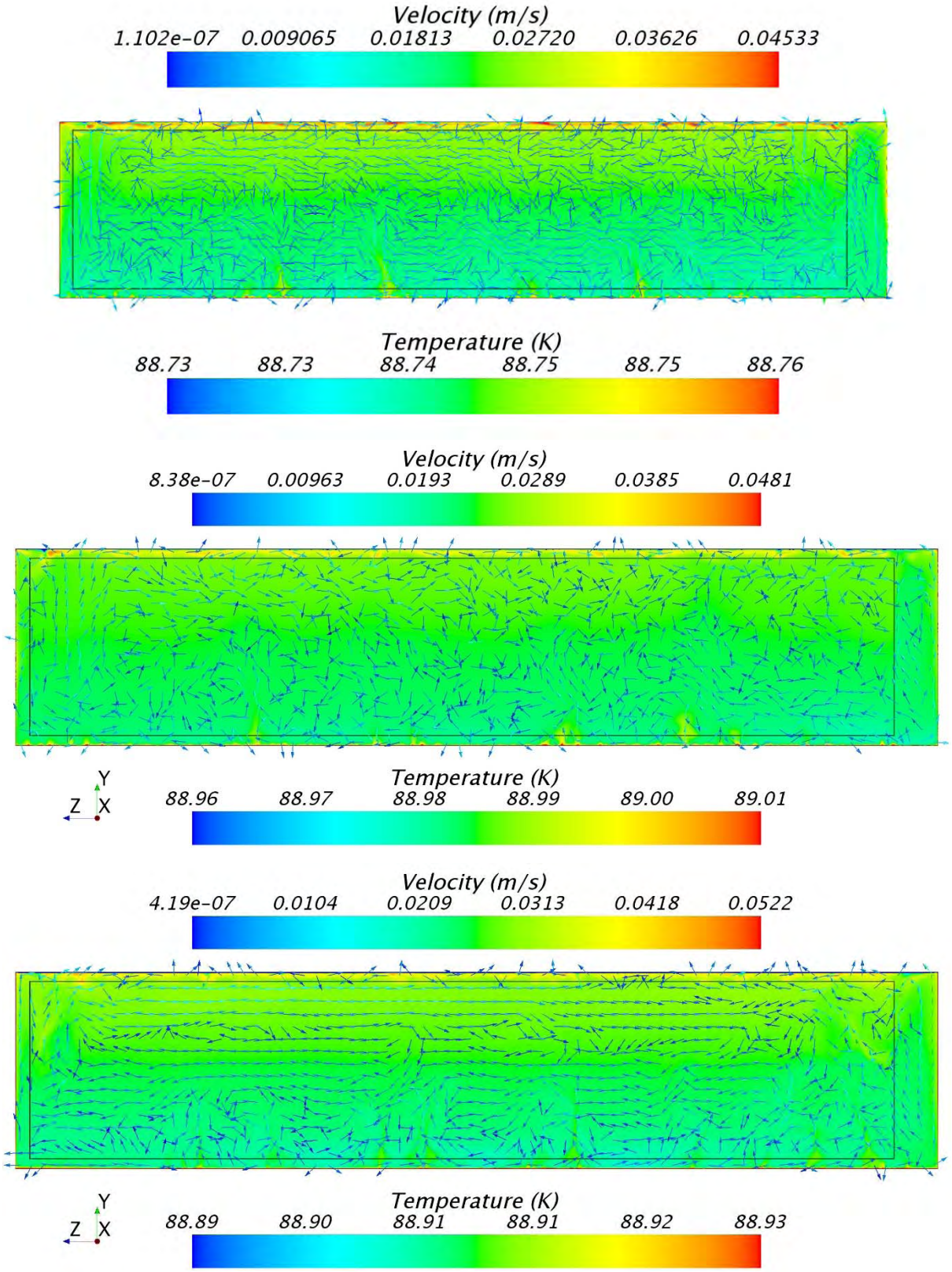

Figure 54. Temperature and velocity vectors at x = 6 m for latest design with original poly, new poly, and new trimmed meshes.

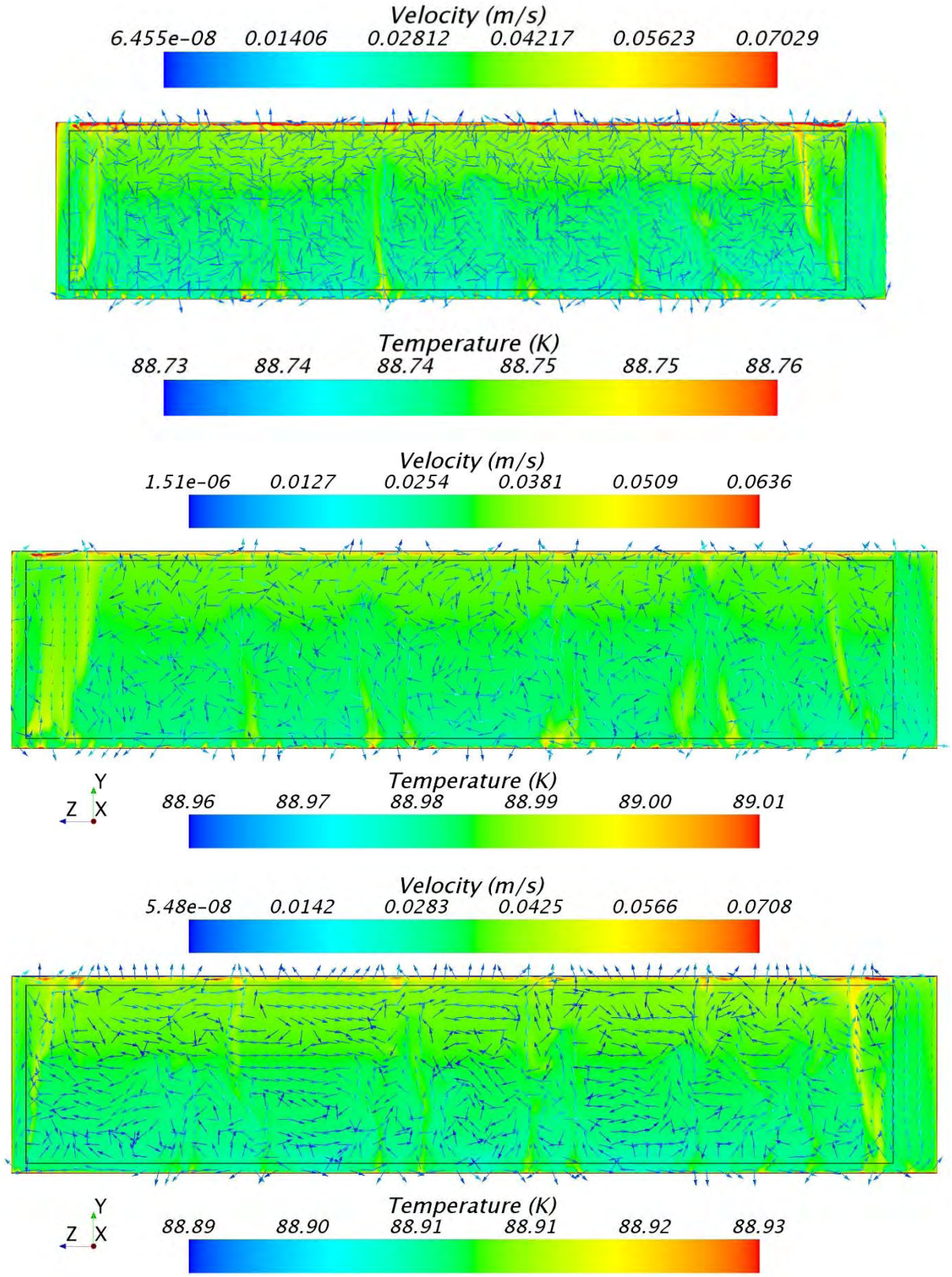

Figure 55. Temperature and velocity vectors at x = 7 m for latest design with original poly, new poly, and new trimmed meshes.

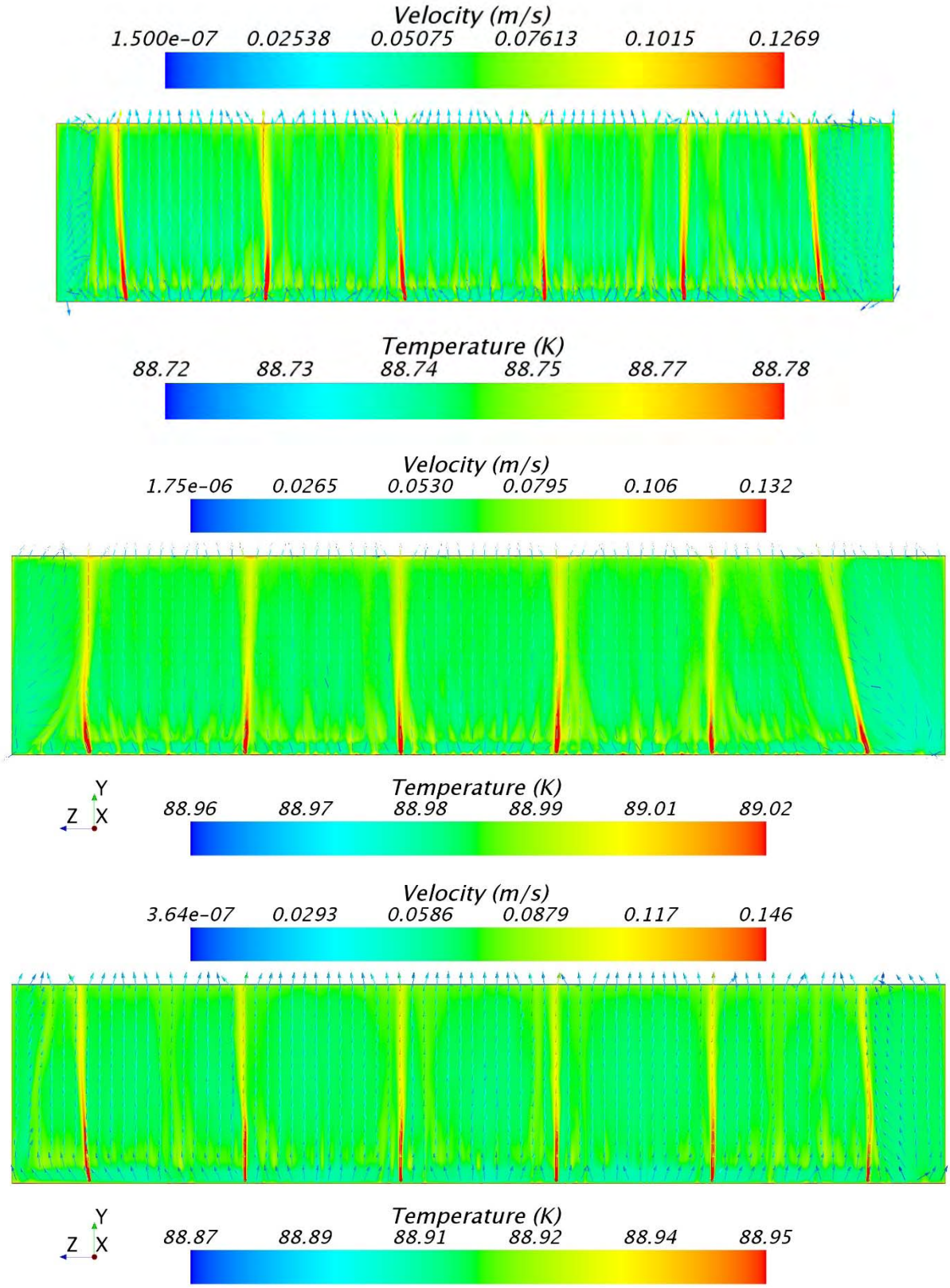

Figure 56. Temperature and velocity vectors at x = 7.4 m for latest design with original poly, new poly, and new trimmed meshes.

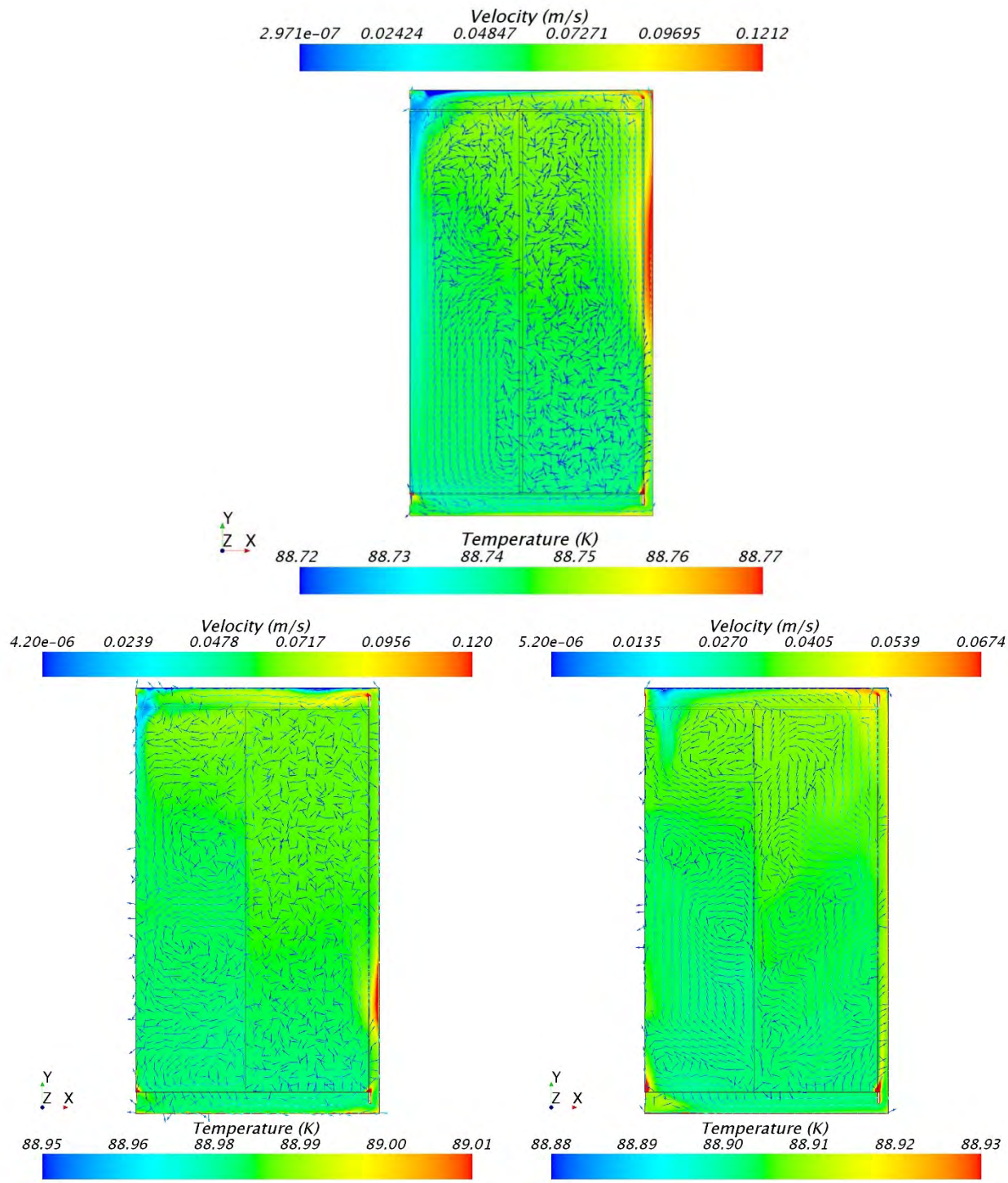

Figure 57. Temperature and velocity vectors at z = -25 m for latest design with original poly, new poly, and new trimmed meshes.

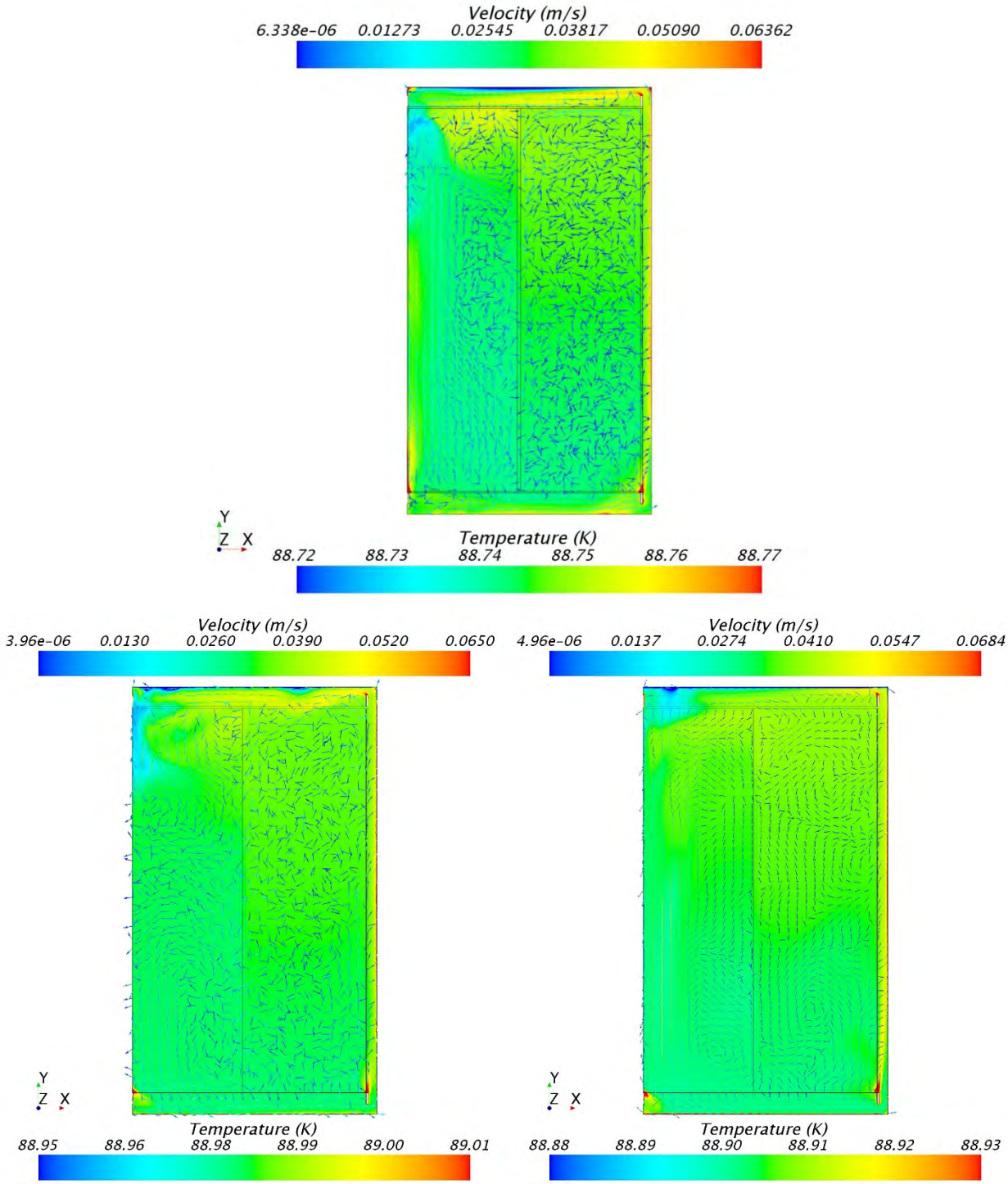

Figure 58. Temperature and velocity vectors at z = -20 m for latest design with original poly, new poly, and new trimmed meshes.

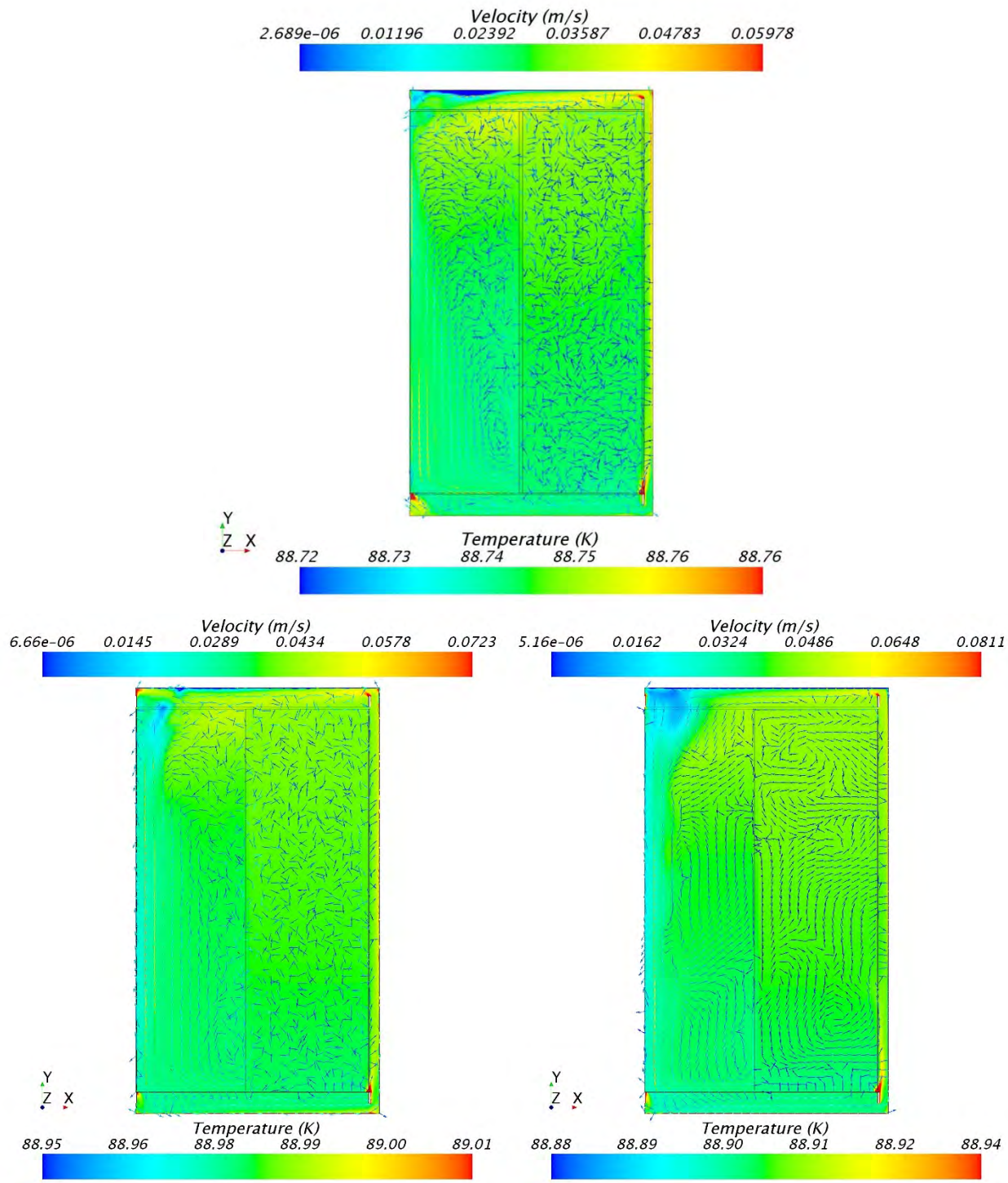

Figure 59. Temperature and velocity vectors at z = 0.0 m for latest design with original poly, new poly, and new trimmed meshes.

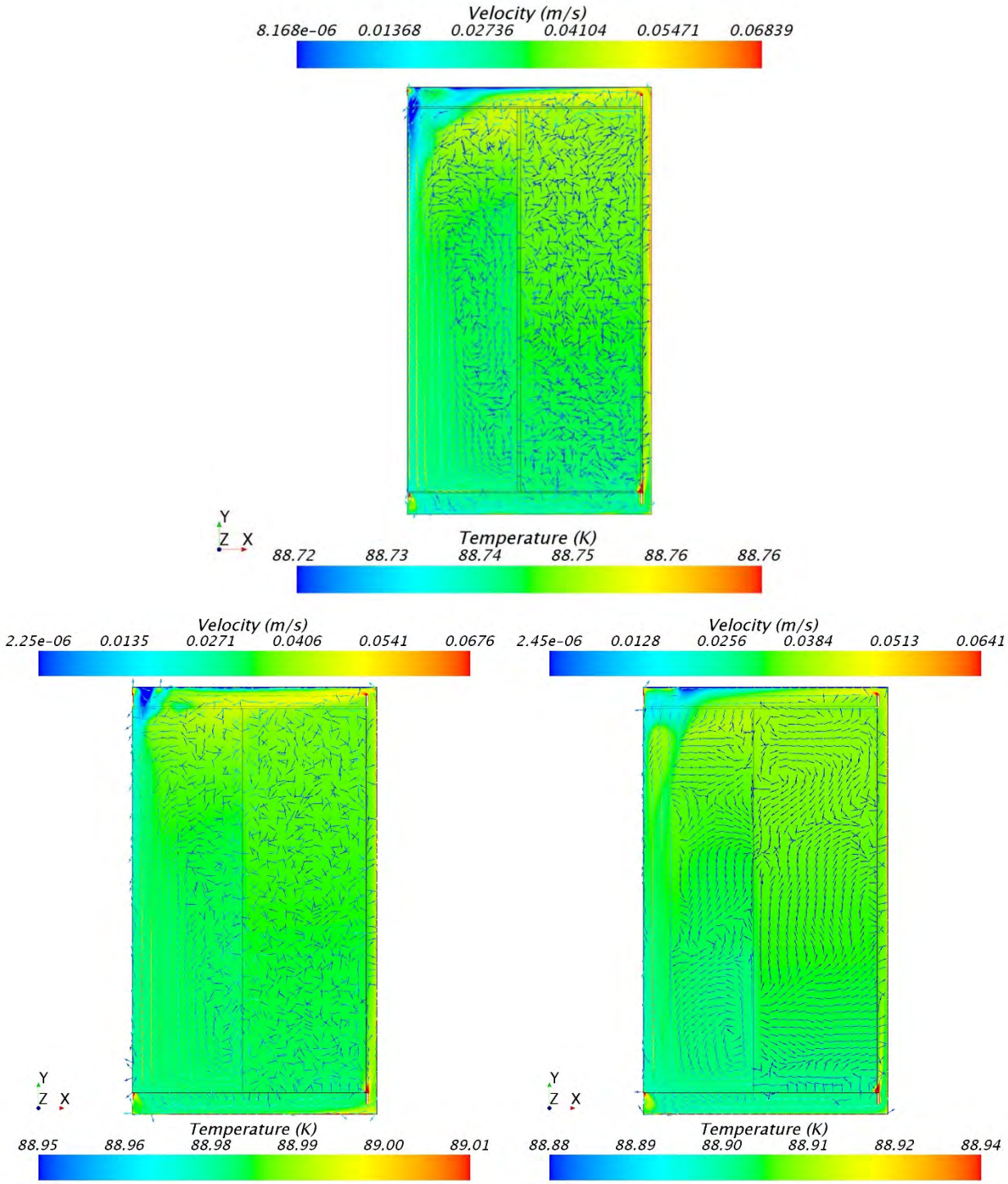

Figure 60. Temperature and velocity vectors at z = 10 m for latest design with original poly, new poly, and new trimmed meshes.

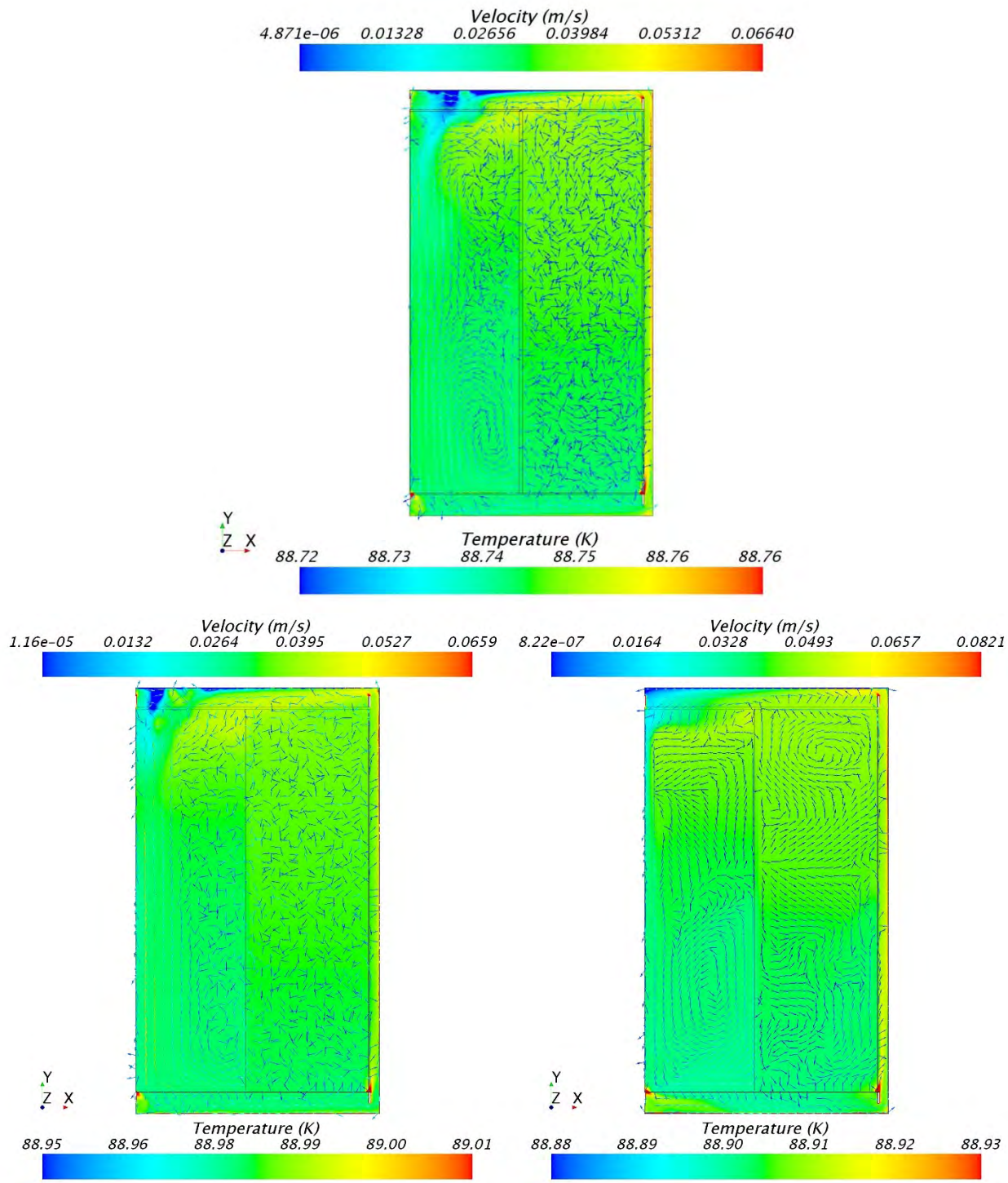

Figure 61. Temperature and velocity vectors at z = 20 m for latest design with original poly, new poly, and new trimmed meshes.

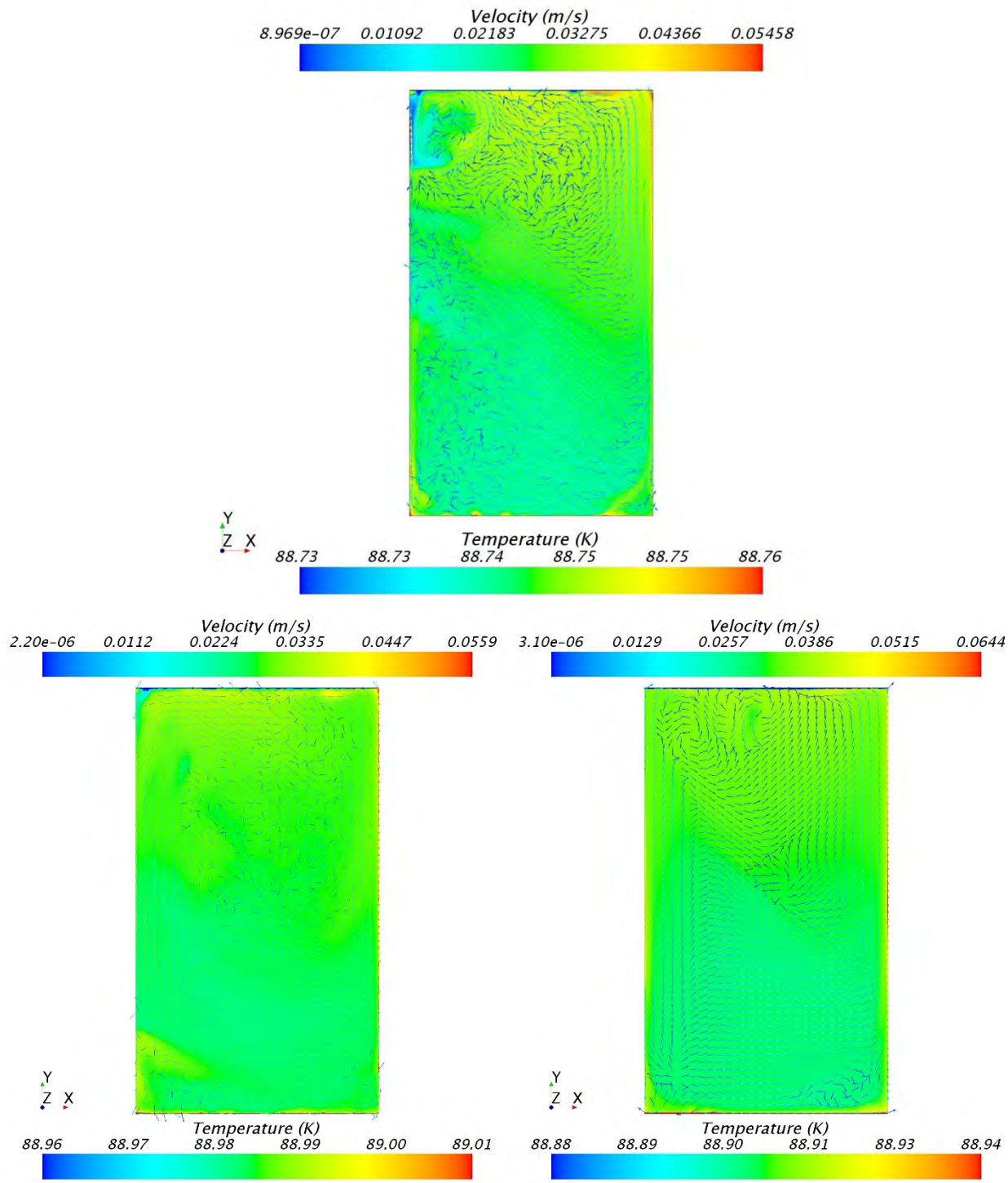

Figure 62. Temperature and velocity vectors at z = 30.5 m for latest design with original poly, new poly, and new trimmed meshes.

Streamlines

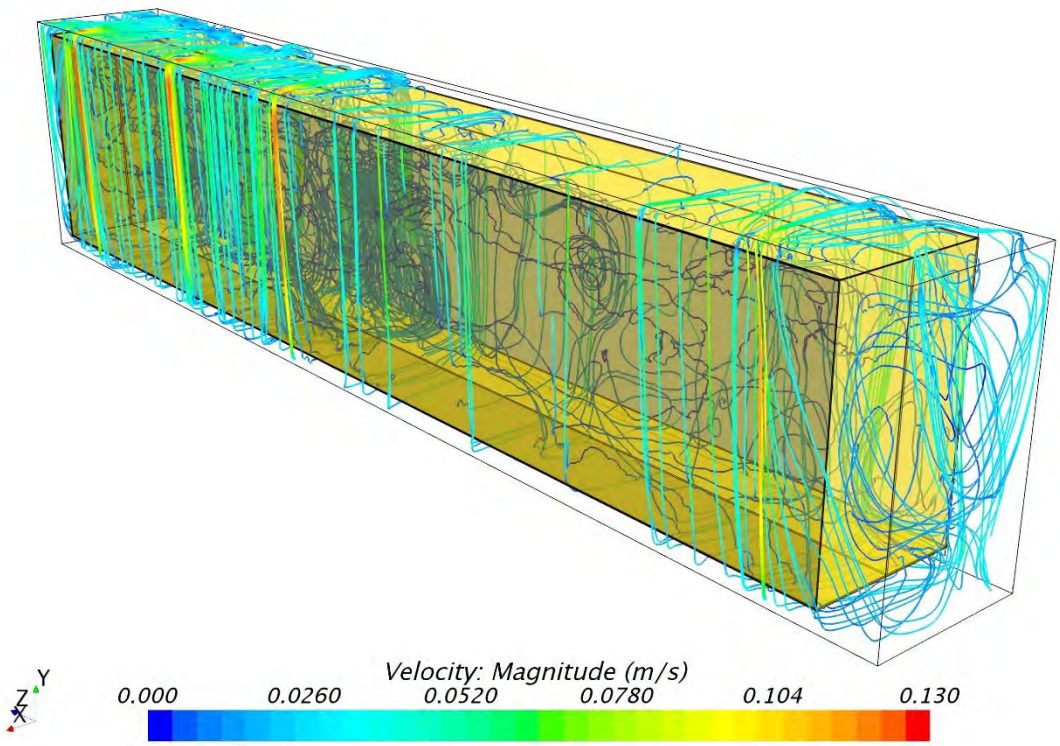

Figure 63. Streamline view 1 for latest design with original polyhedral mesh.

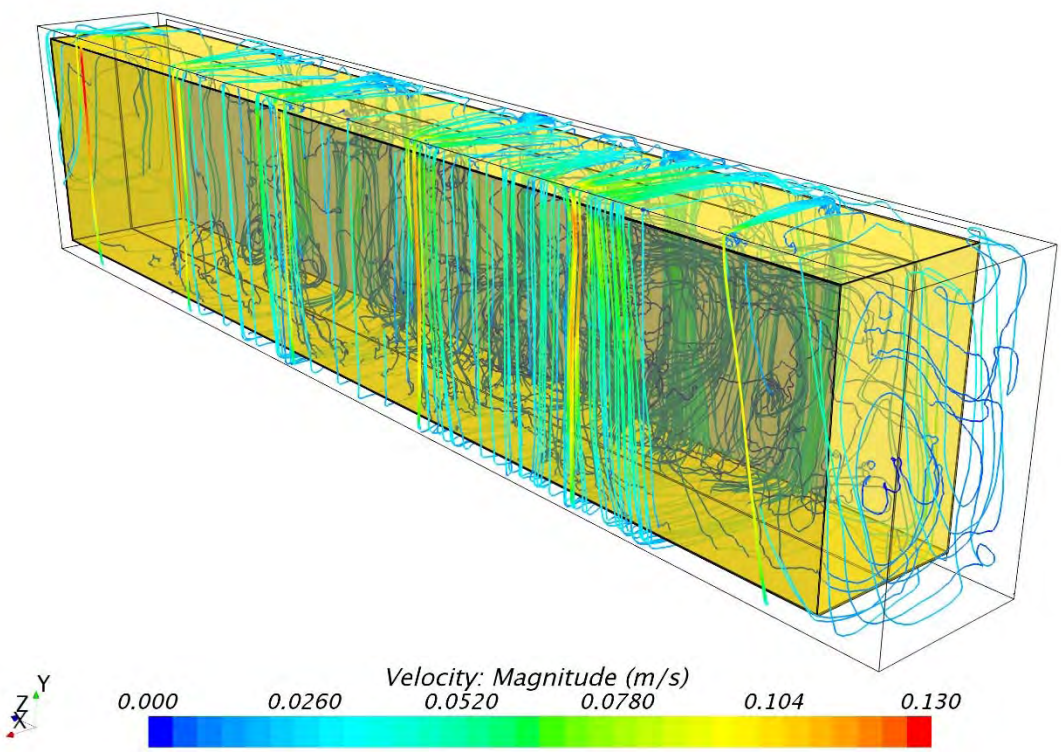

Figure 64. Streamline view 1 for latest design with new polyhedral mesh.

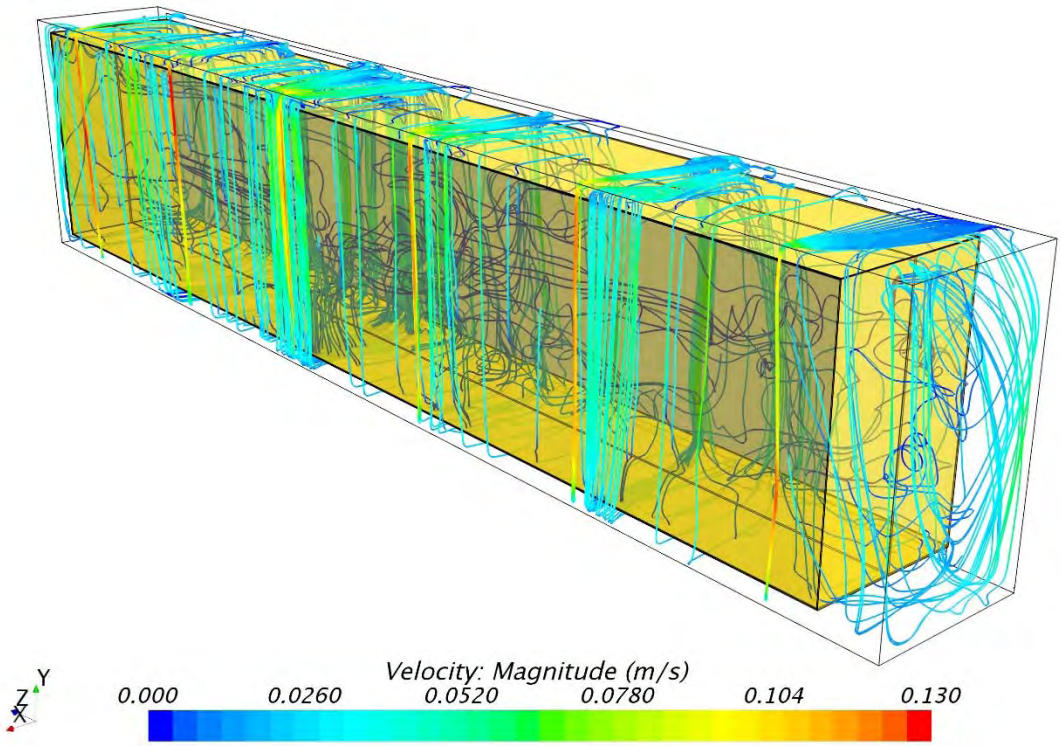

Figure 65. Streamline view 1 for latest design with new trimmed mesh.

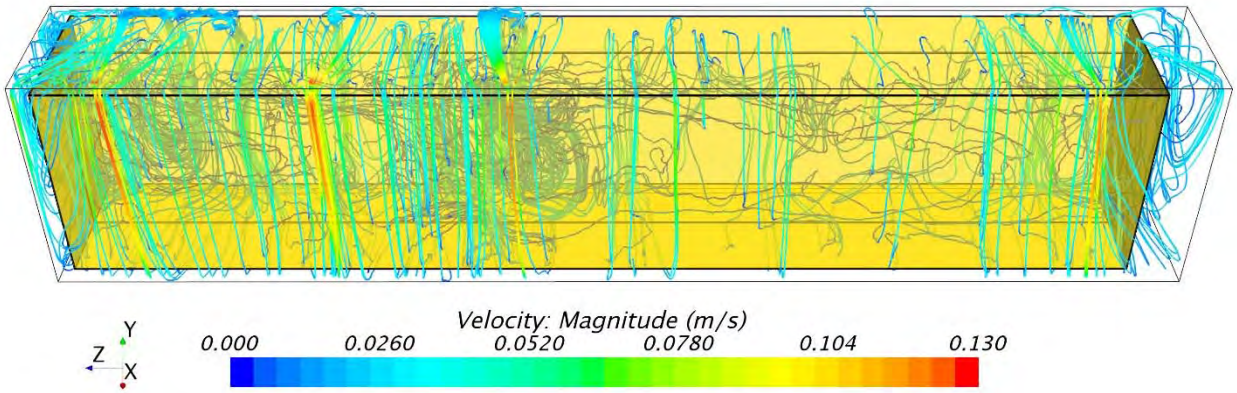

Figure 66. Streamline view 2 for latest design with original polyhedral mesh.

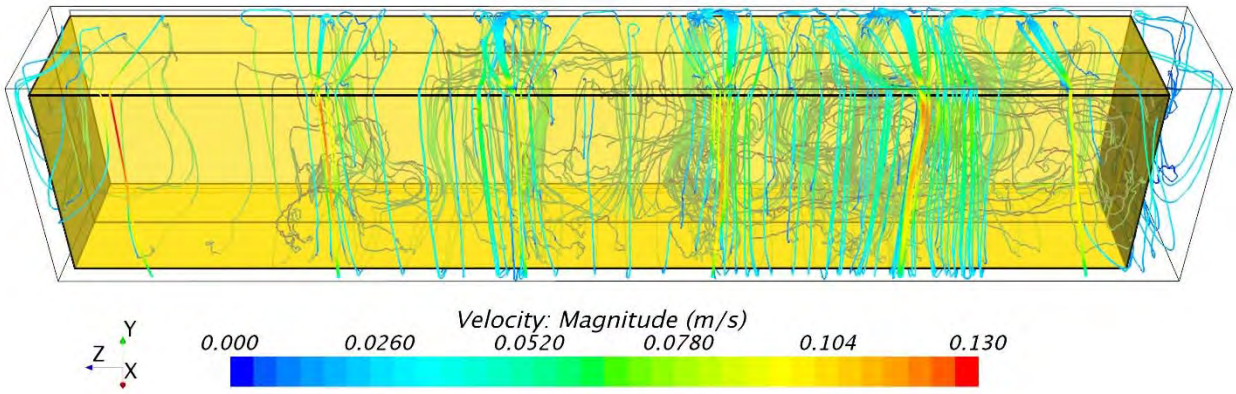

Figure 67. Streamline view 2 for latest design with new polyhedral mesh.

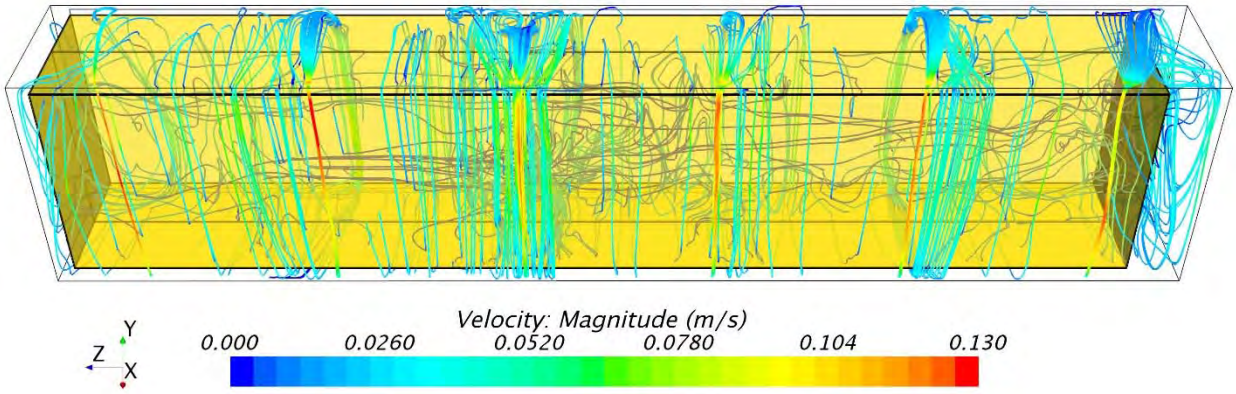

Figure 68. Streamline view 2 for latest design with new trimmed mesh.

Latest Design with Electronics Turned Off

The average temperature of the cryostat decreased by about 0.2 K when the electronics were turned off. Considering how small the range of temperatures in the cryostat is, this change is quite significant. The plot below shows the change in temperature when the electronics were turned off.

Figure 69. Plot of average temperature with the electronics shut off at 100,000 iterations.

Impurity and Temperature with Velocity Vectors

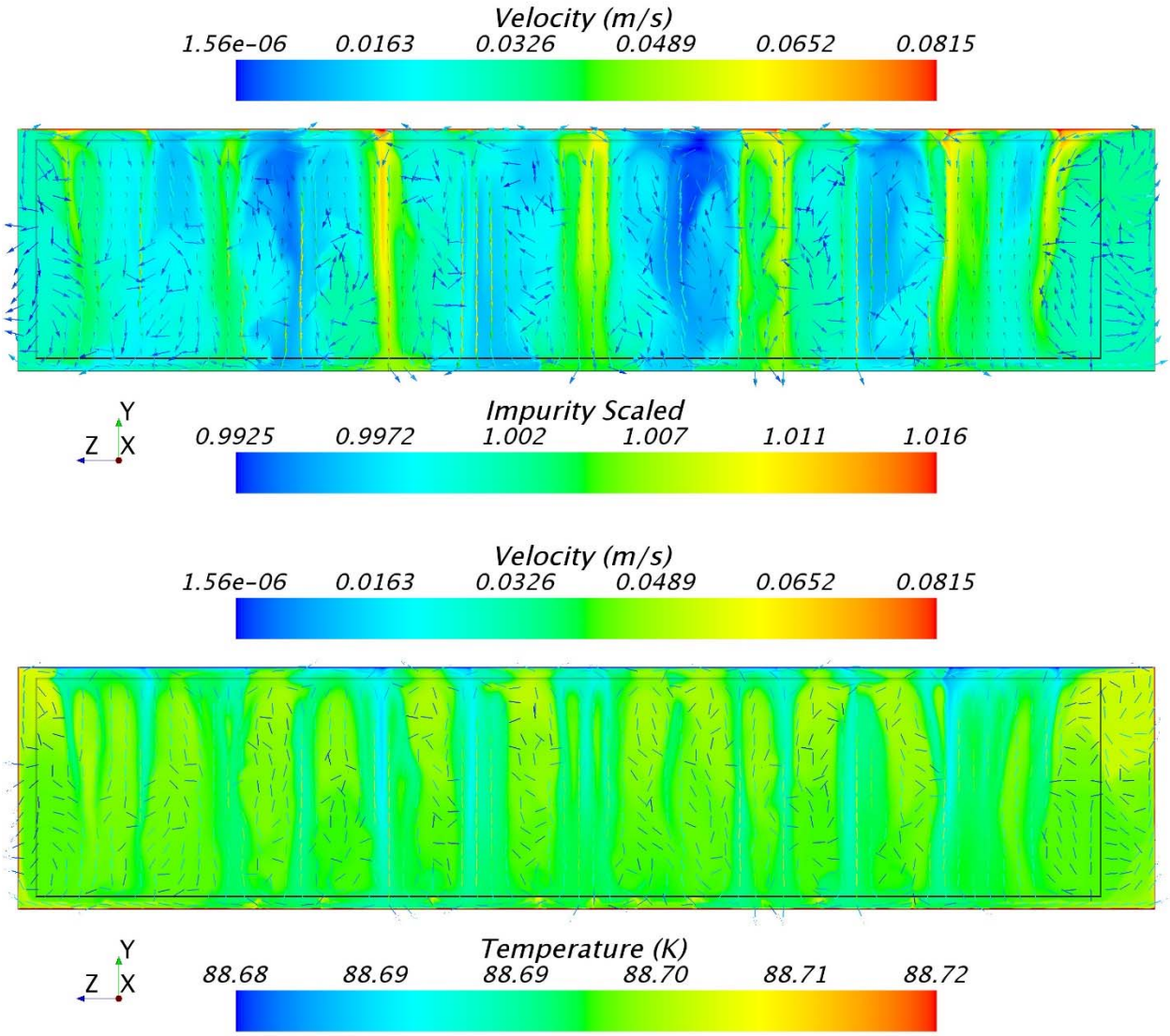

Figure 70. Impurity and temperature with velocity vectors at x = 0.1 m for latest design with electronics turned off (trimmed mesh).

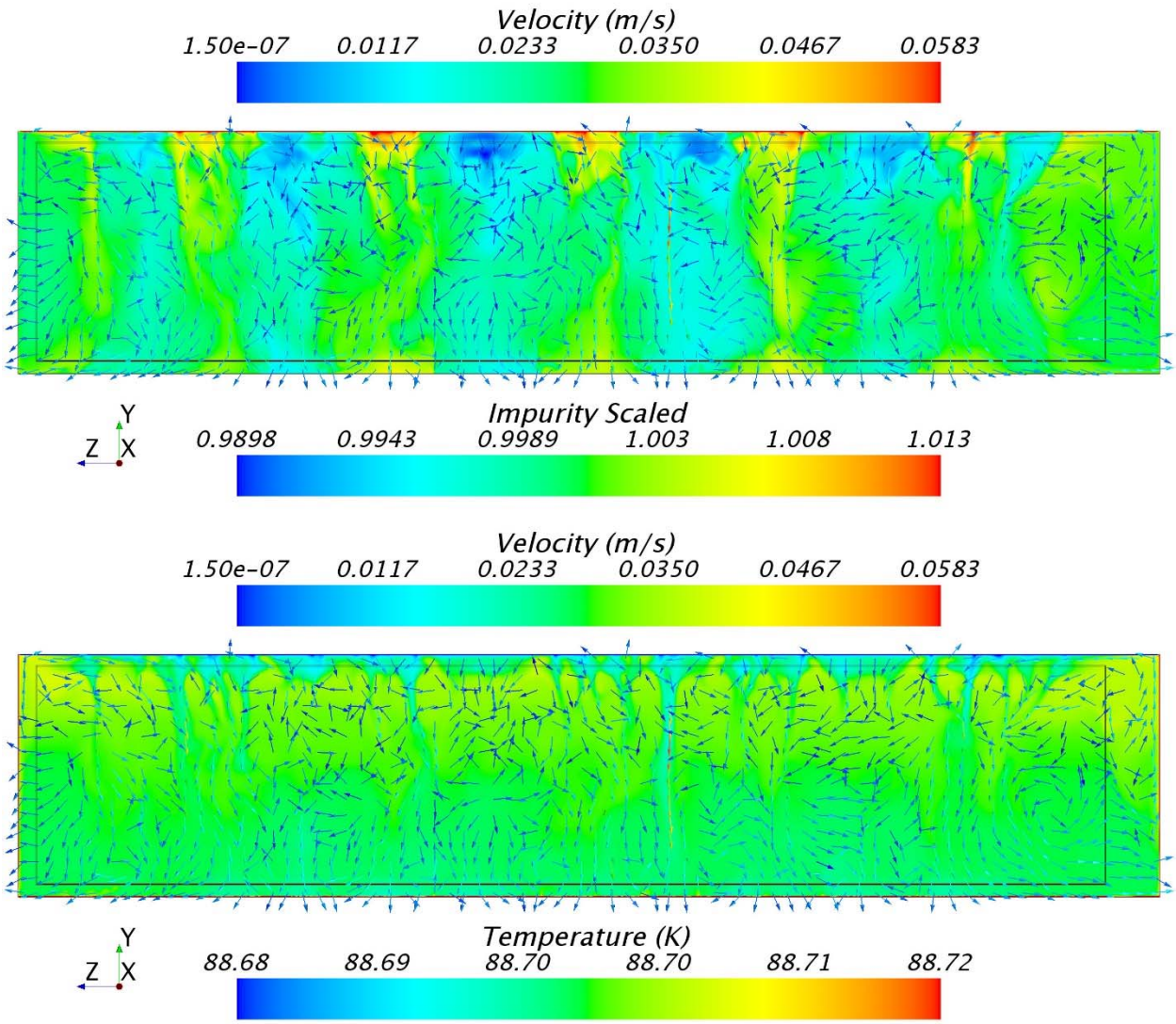

Figure 71. Impurity and temperature with velocity vectors at x = 1 m for latest design with electronics turned off (trimmed mesh).

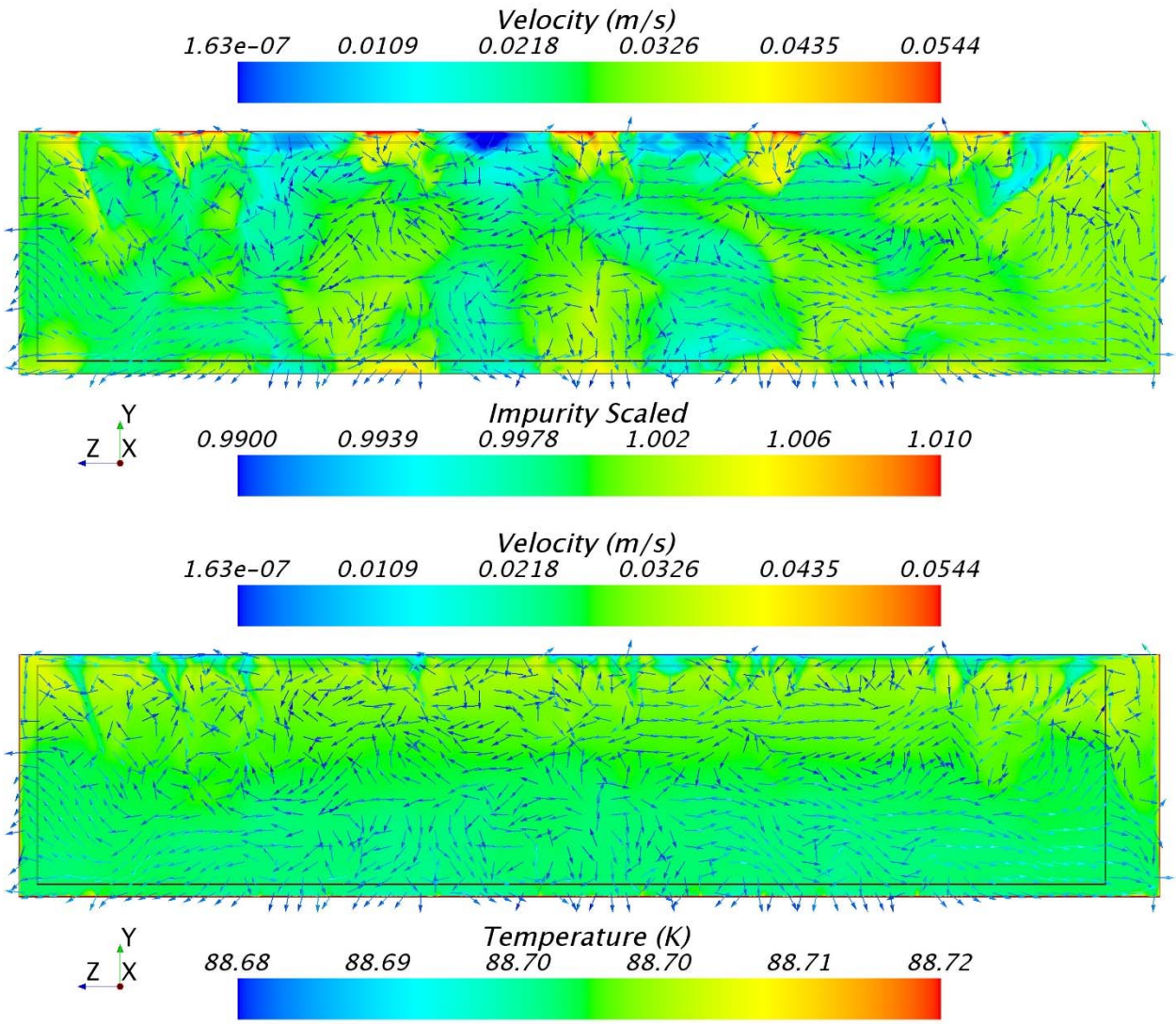

Figure 72. Impurity and temperature with velocity vectors at x = 2 m for latest design with electronics turned off (trimmed mesh).

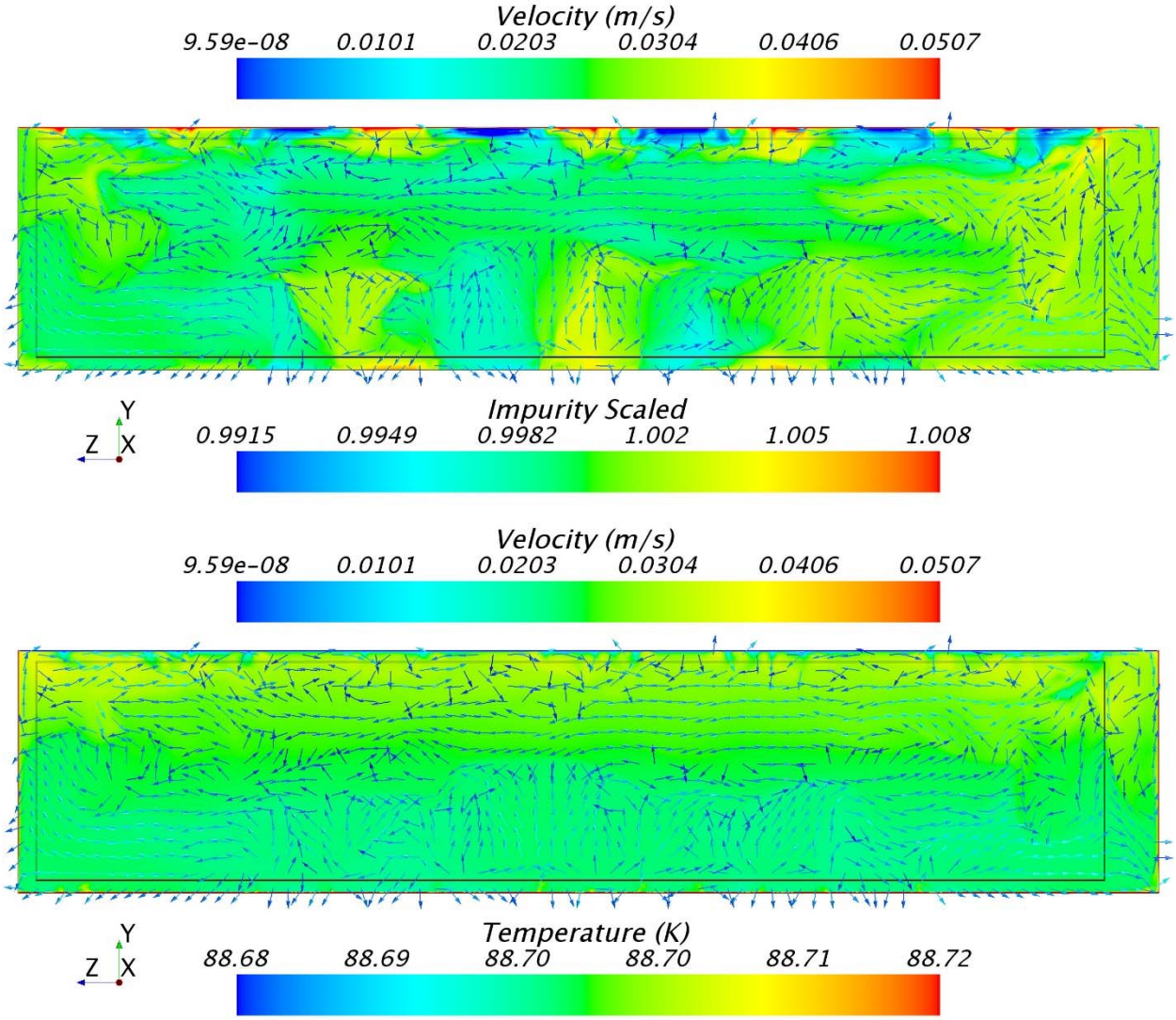

Figure 73. Impurity and temperature with velocity vectors at x = 3 m for latest design with electronics turned off (trimmed mesh).

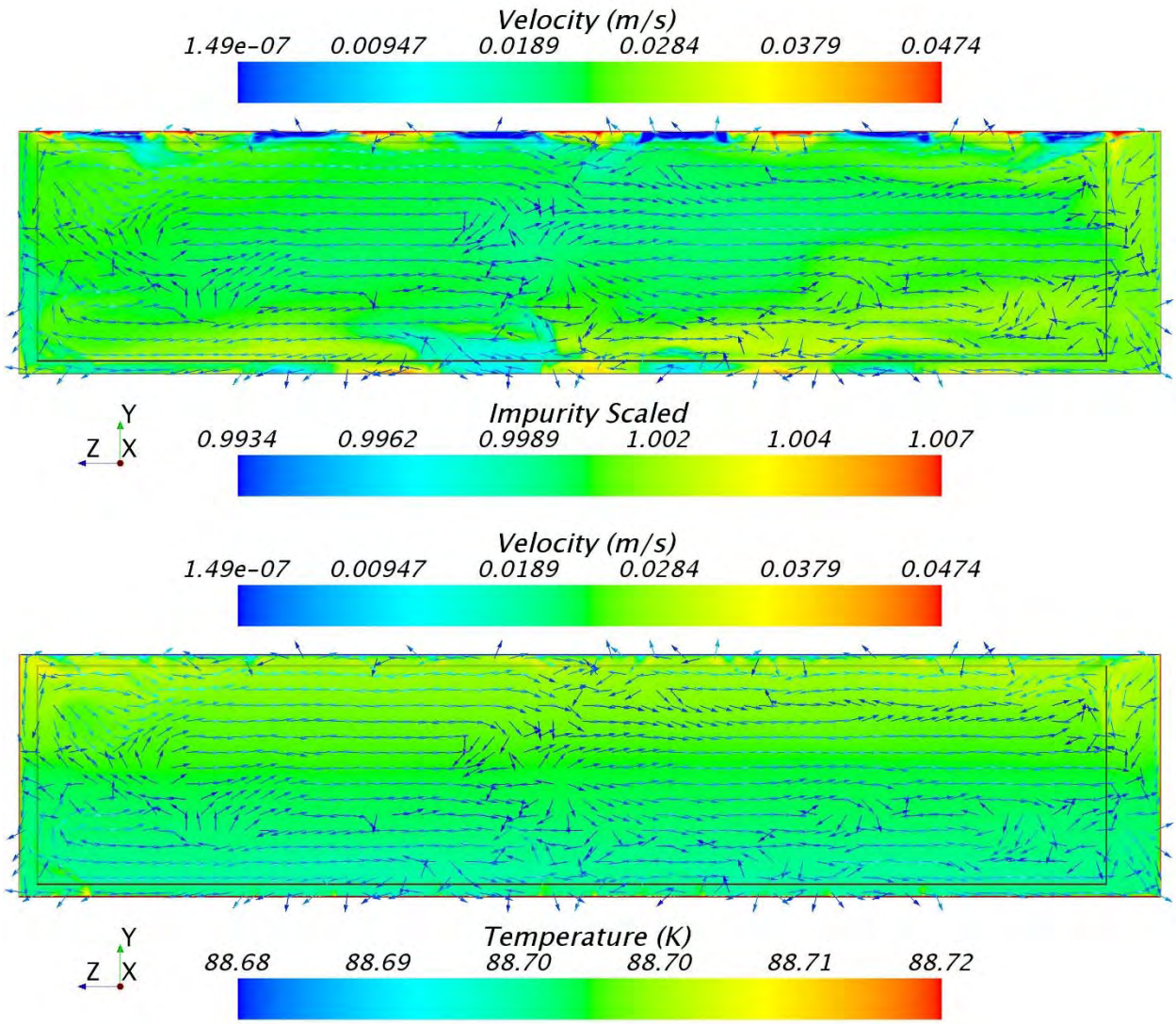

Figure 74. Impurity and temperature with velocity vectors at x = 4 m for latest design with electronics turned off (trimmed mesh).

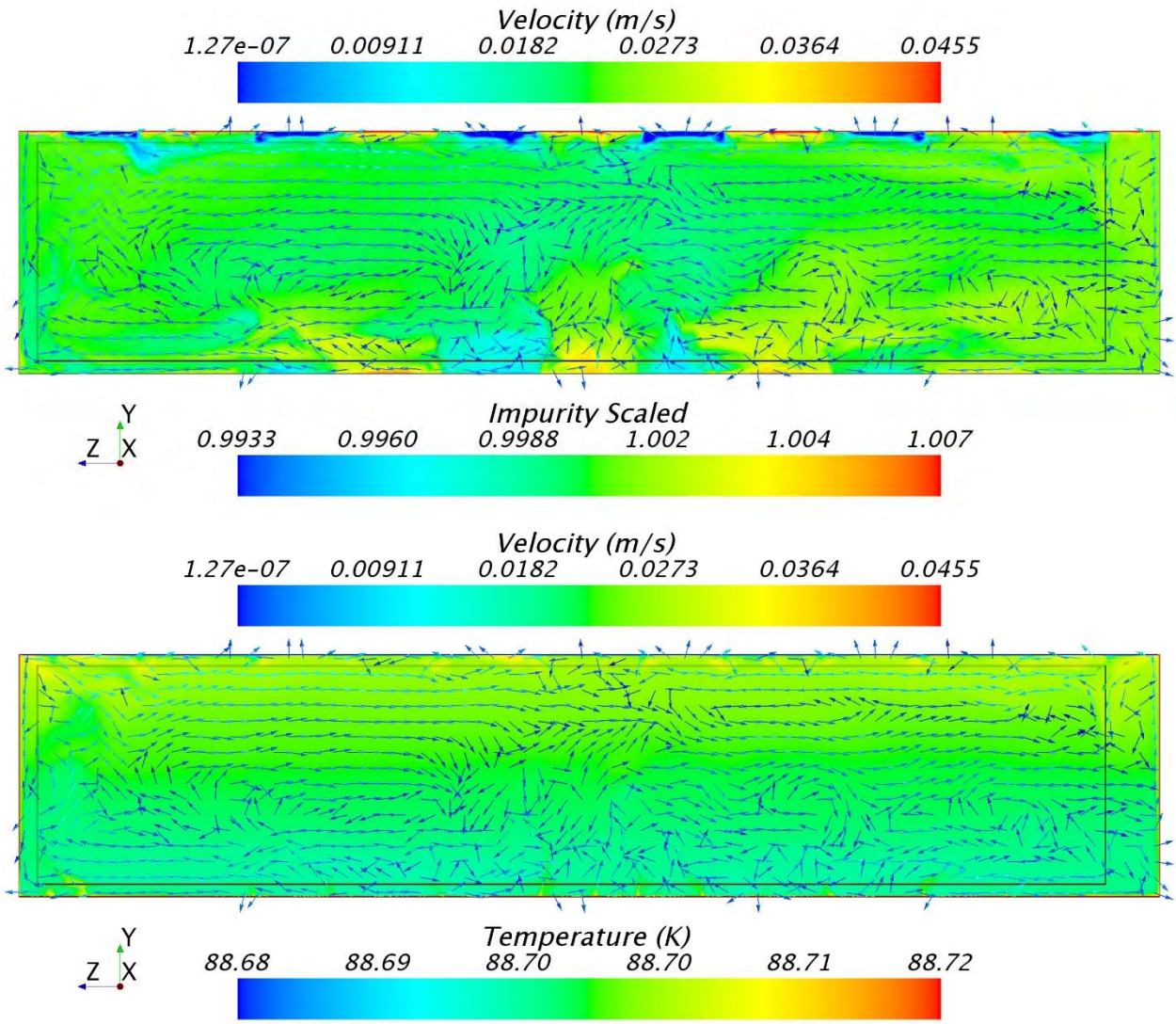

Figure 75. Impurity and temperature with velocity vectors at x = 5 m for latest design with electronics turned off (trimmed mesh).

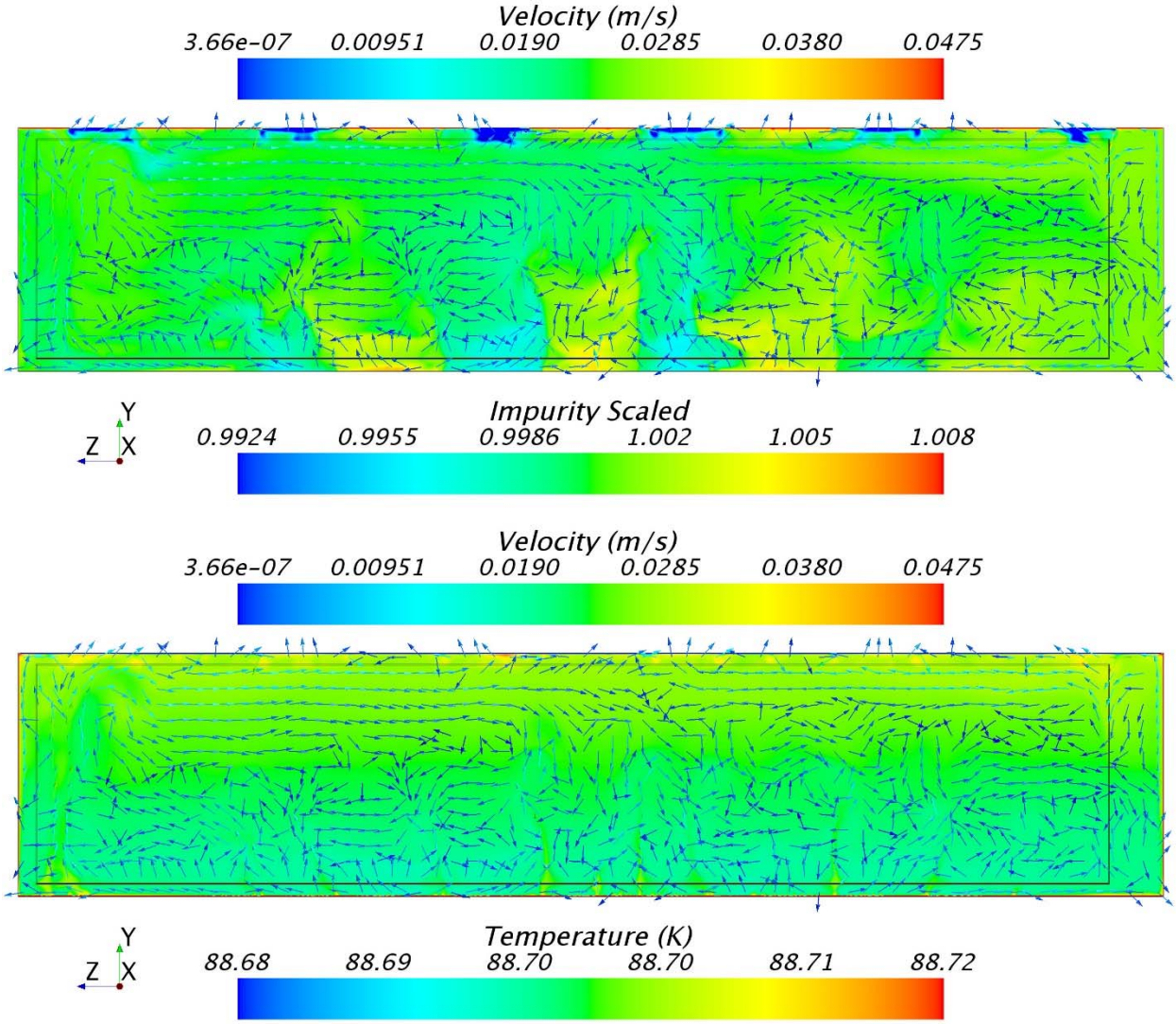

Figure 76. Impurity and temperature with velocity vectors at x = 6 m for latest design with electronics turned off (trimmed mesh).

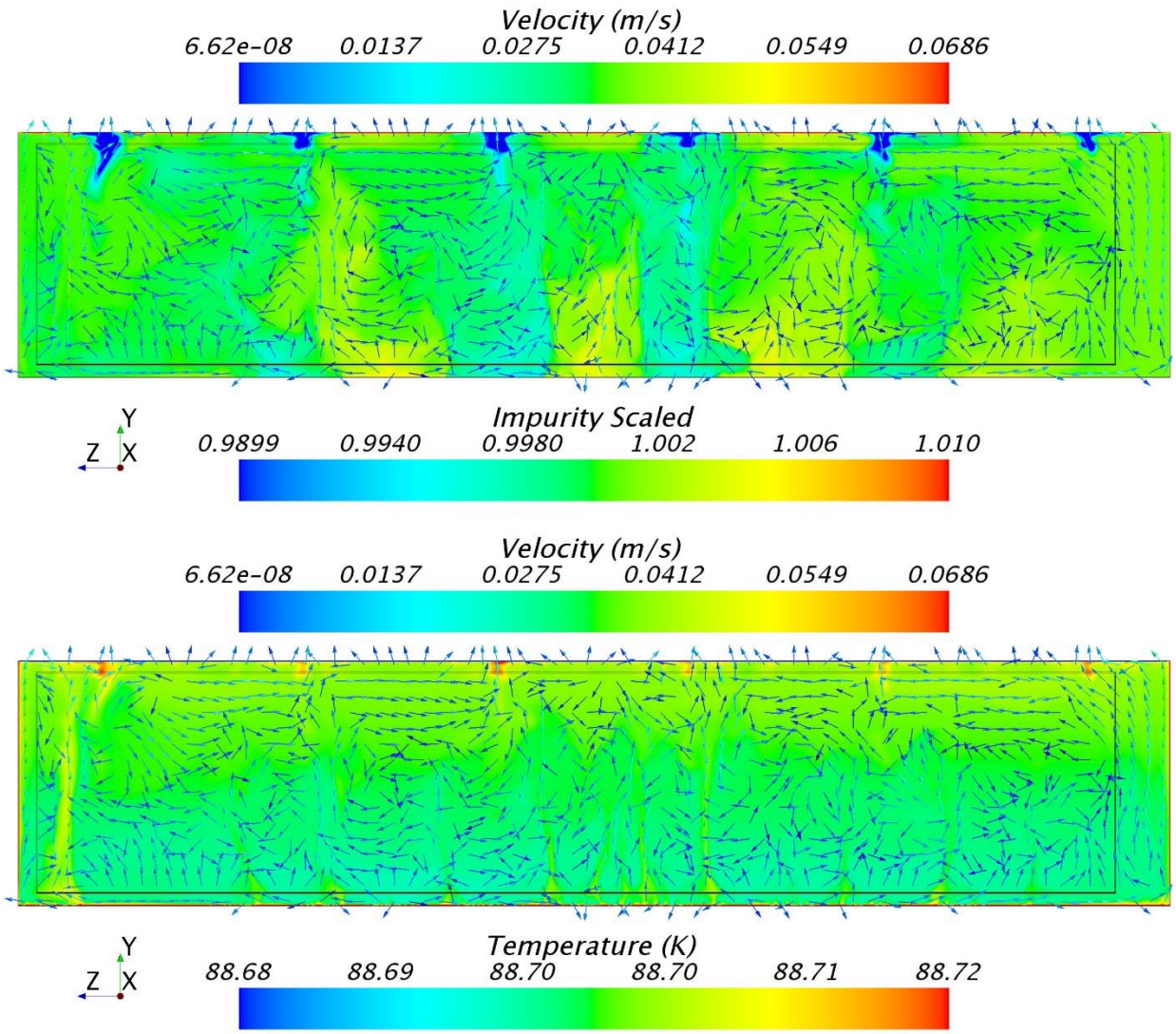

Figure 77. Impurity and temperature with velocity vectors at x = 7 m for latest design with electronics turned off (trimmed mesh).

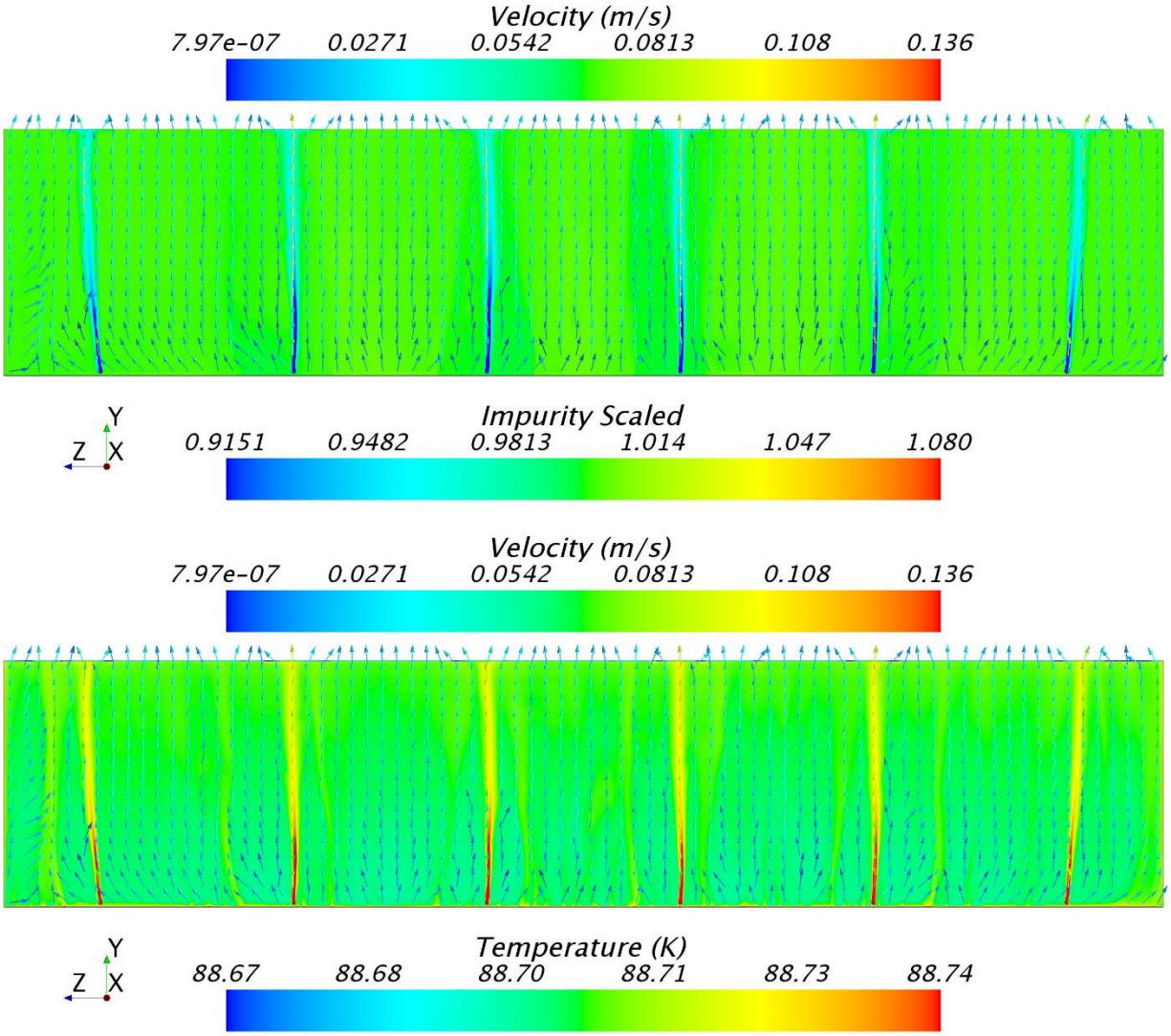

Figure 78. Impurity and temperature with velocity vectors at x = 7.4 m for latest design with electronics turned off (trimmed mesh).

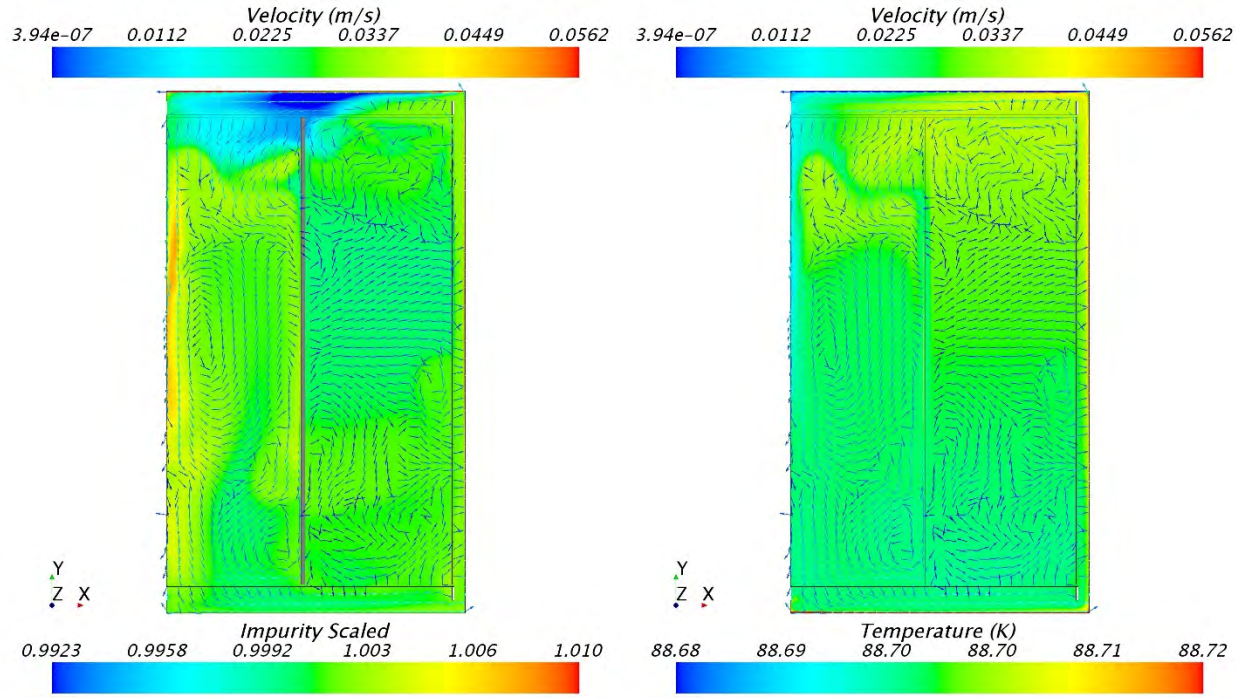

Figure 79. Impurity and temperature with velocity vectors at z = -25 m for latest design with electronics turned off (trimmed mesh).

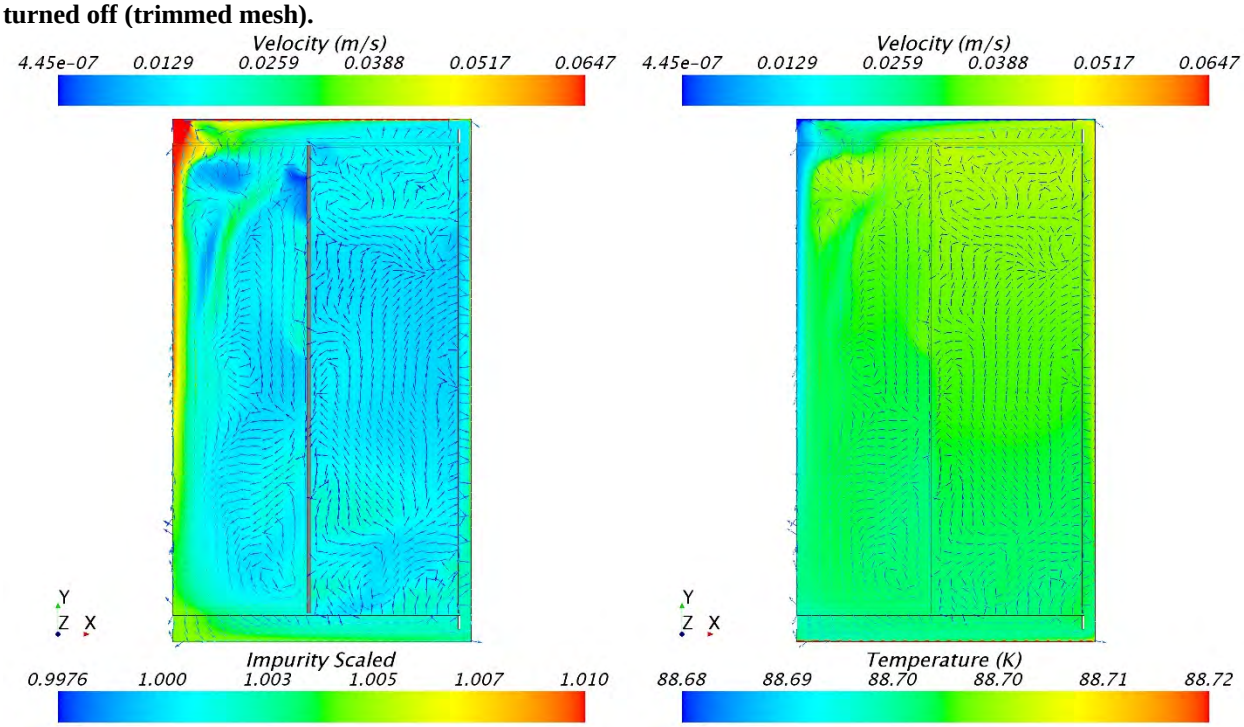

Figure 80. Impurity and temperature with velocity vectors at z = -20 m for latest design with electronics turned off (trimmed mesh).

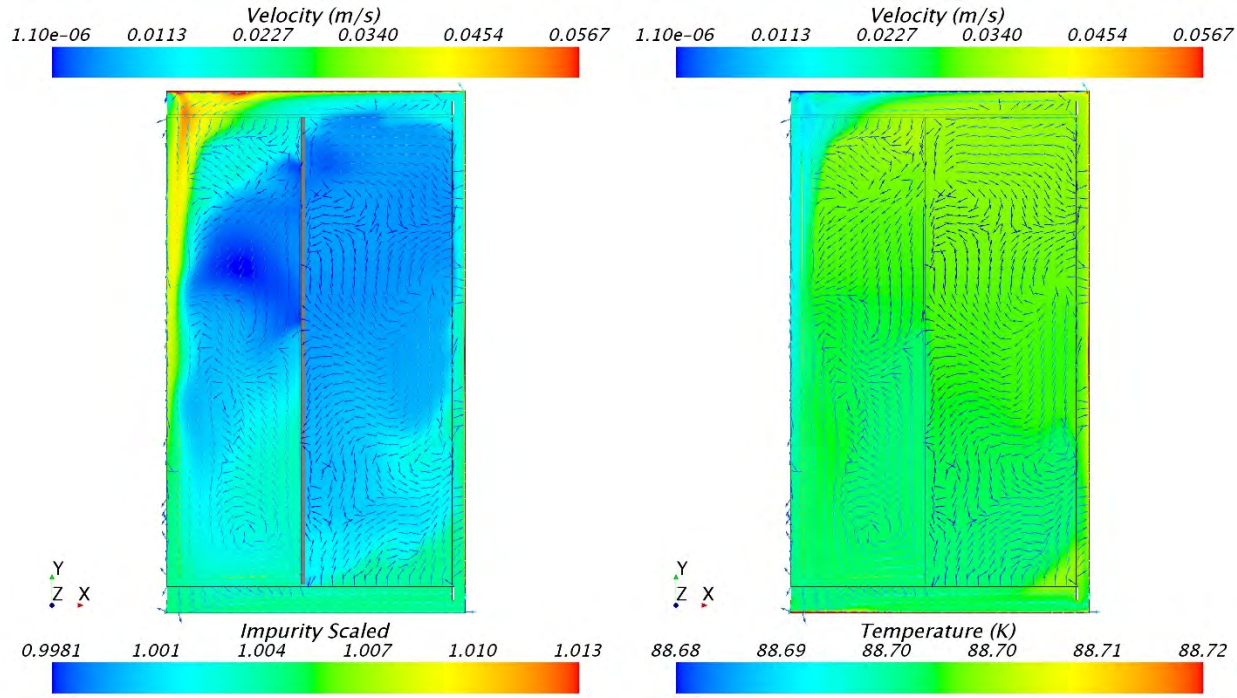

Figure 81. Impurity and temperature with velocity vectors at z = 0.0 m for latest design with electronics turned off (trimmed mesh).

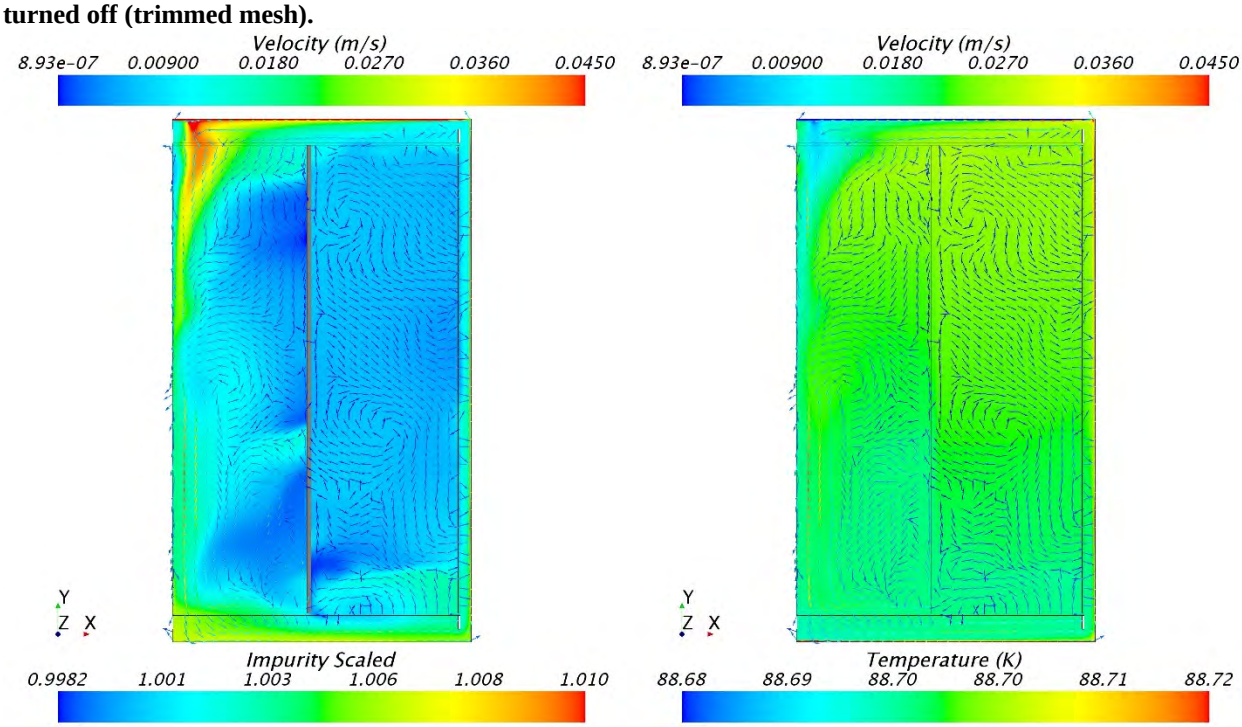

Figure 82. Impurity and temperature with velocity vectors at z = 10 m for latest design with electronics turned off (trimmed mesh).

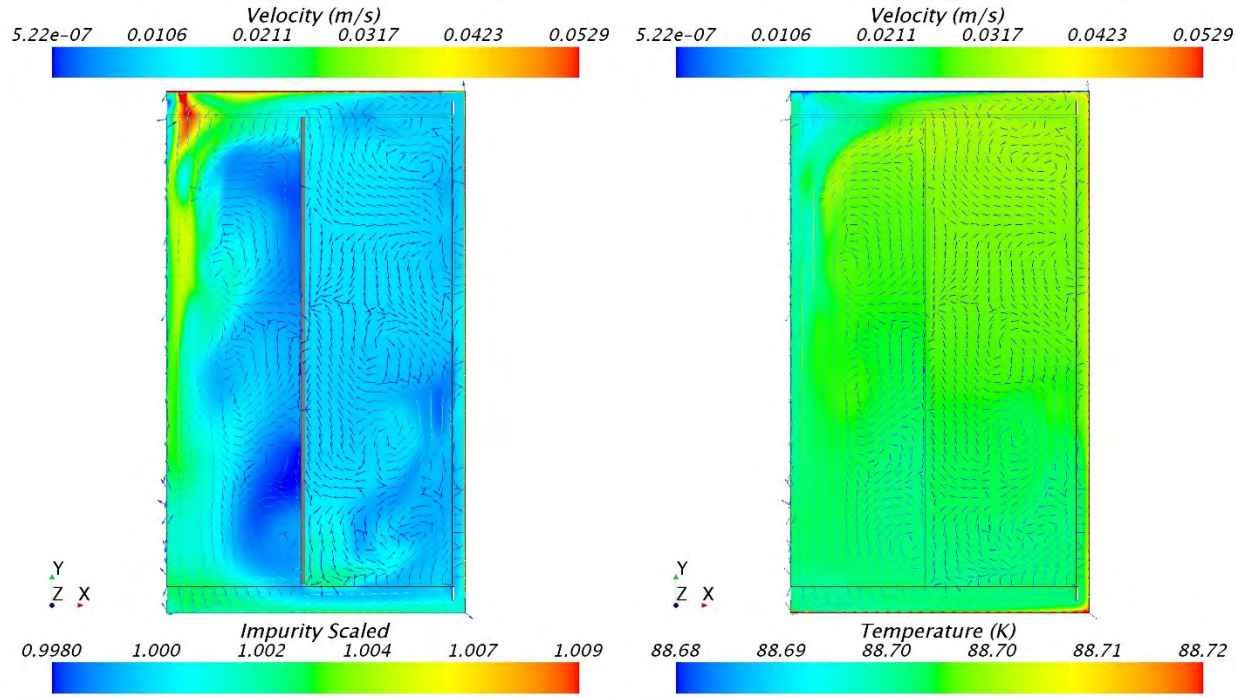

Figure 83. Impurity and temperature with velocity vectors at z = 20 m for latest design with electronics turned off (trimmed mesh).

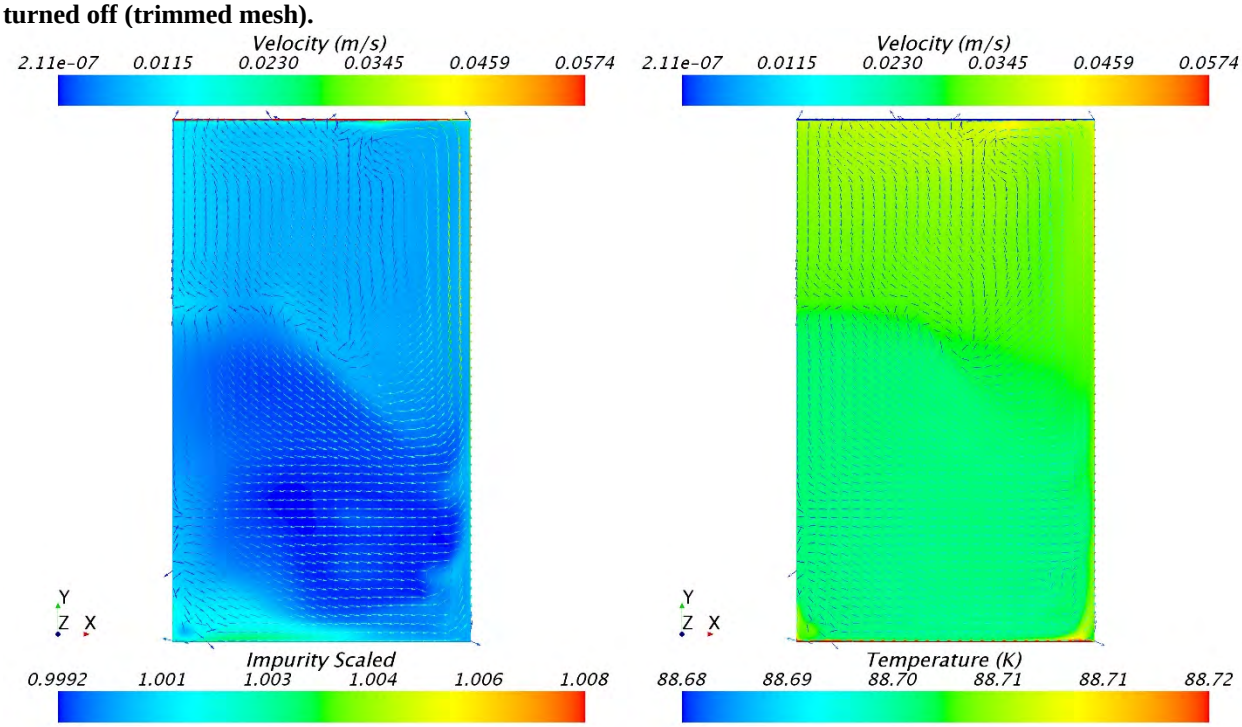

Figure 84. Impurity and temperature with velocity vectors at z = 30.5 m for latest design with electronics turned off (trimmed mesh).

Streamlines

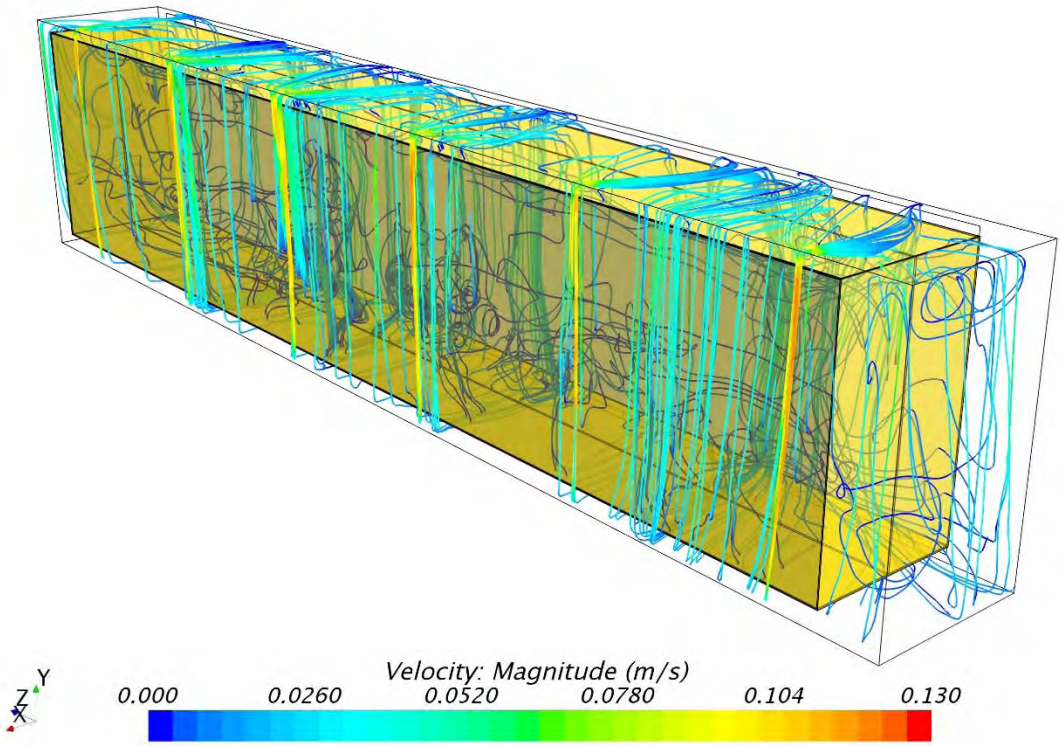

Figure 85. Streamline view 1 for latest design with electronics turned off.

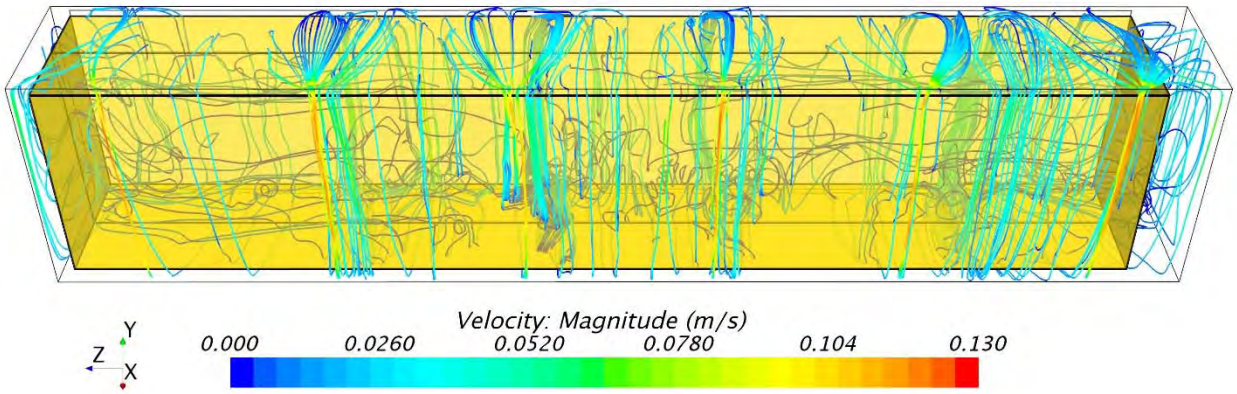

Figure 86. Streamline view 2 for latest design with electronics turned off.

Latest Design with 50% LAr Flow Rate (NOT UPDATED)

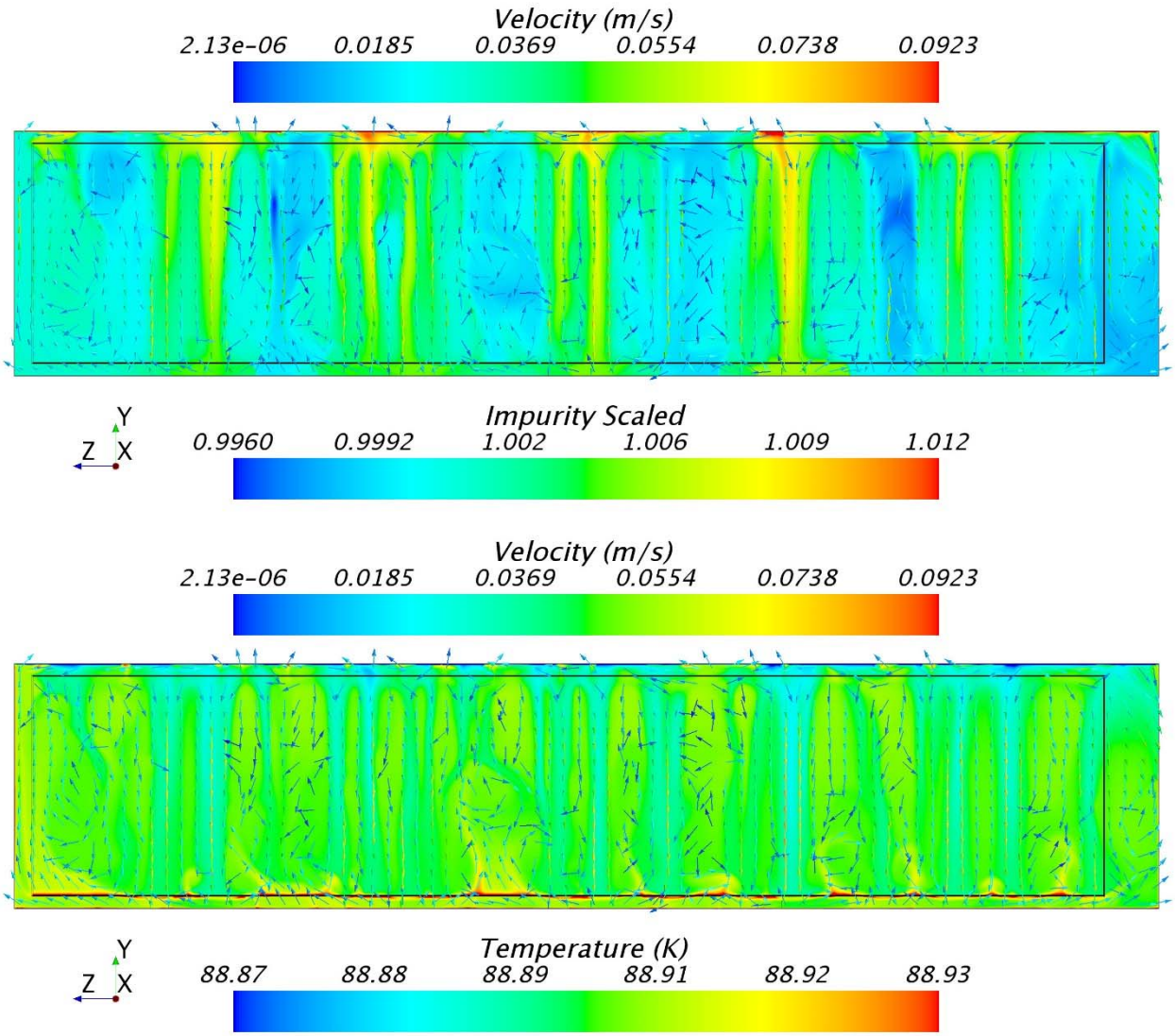

Figure 87. Impurity and temperature with velocity vectors at x = 0.1 m for latest design with 50% LAr flow rate (trimmed mesh).

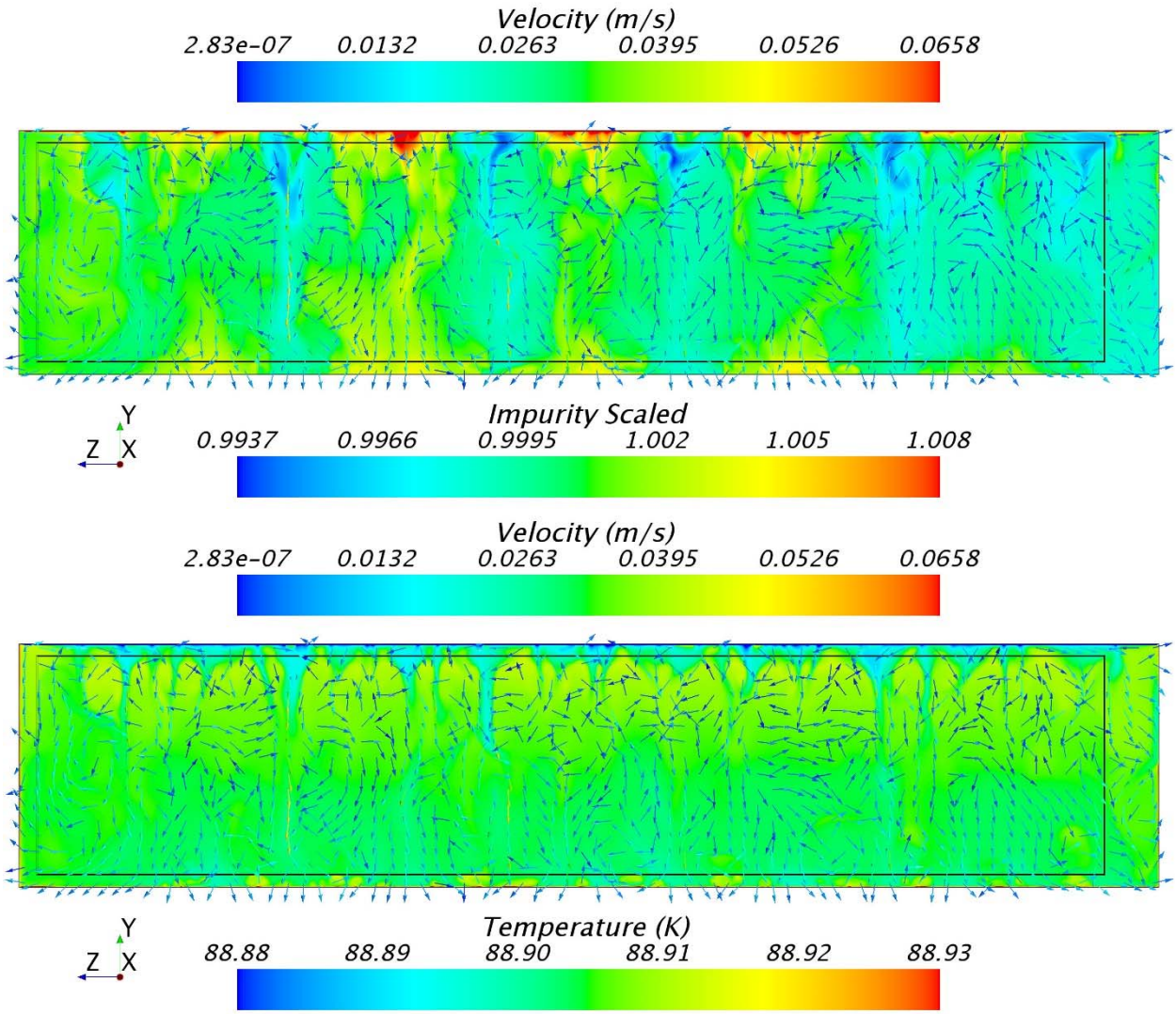

Figure 88. Impurity and temperature with velocity vectors at x = 1 m for latest design with 50% LAr flow rate (trimmed mesh).

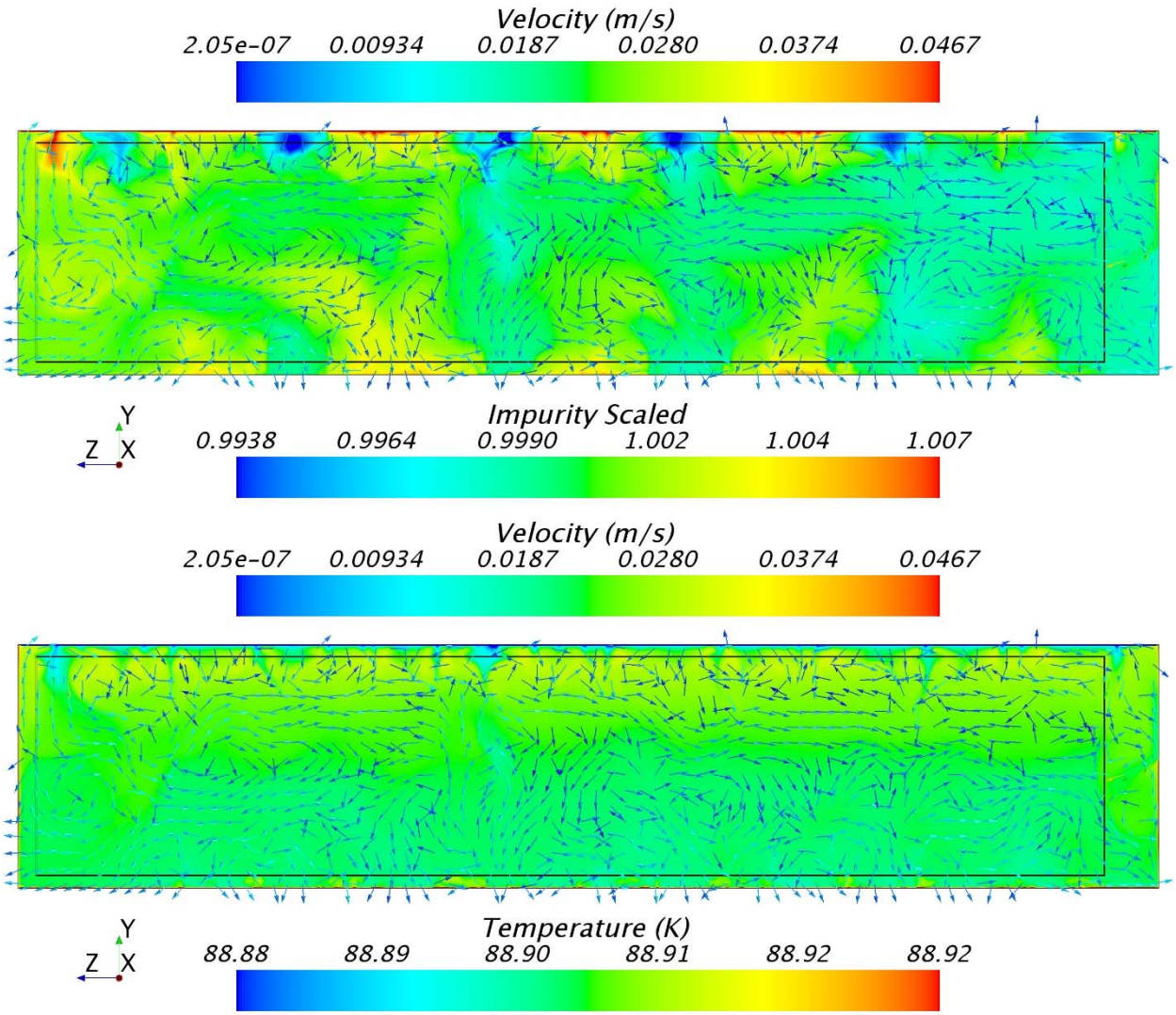

Figure 89. Impurity and temperature with velocity vectors at x = 2 m for latest design with 50% LAr flow rate (trimmed mesh).

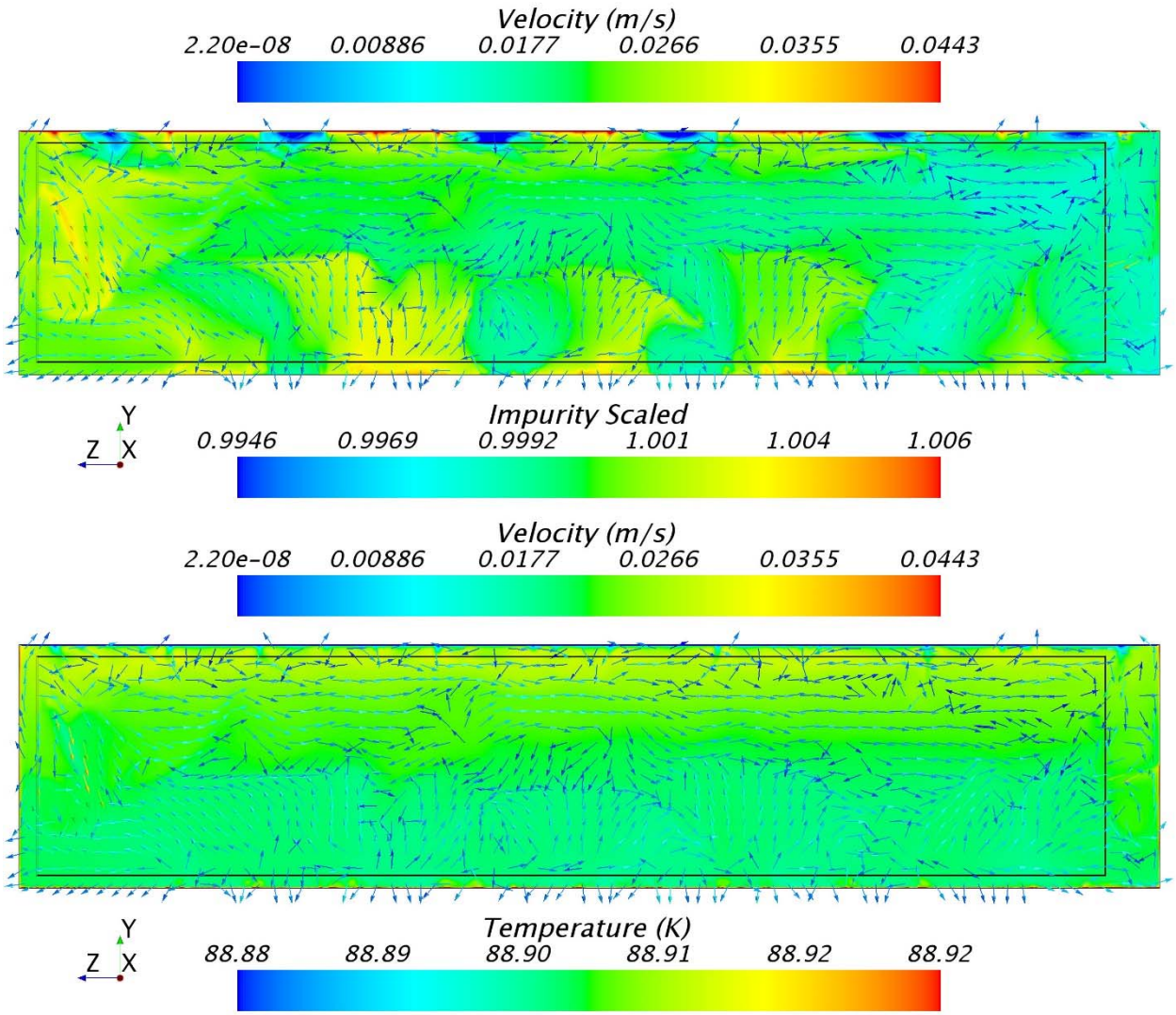

Figure 90. Impurity and temperature with velocity vectors at x = 3 m for latest design with 50% LAr flow rate (trimmed mesh).

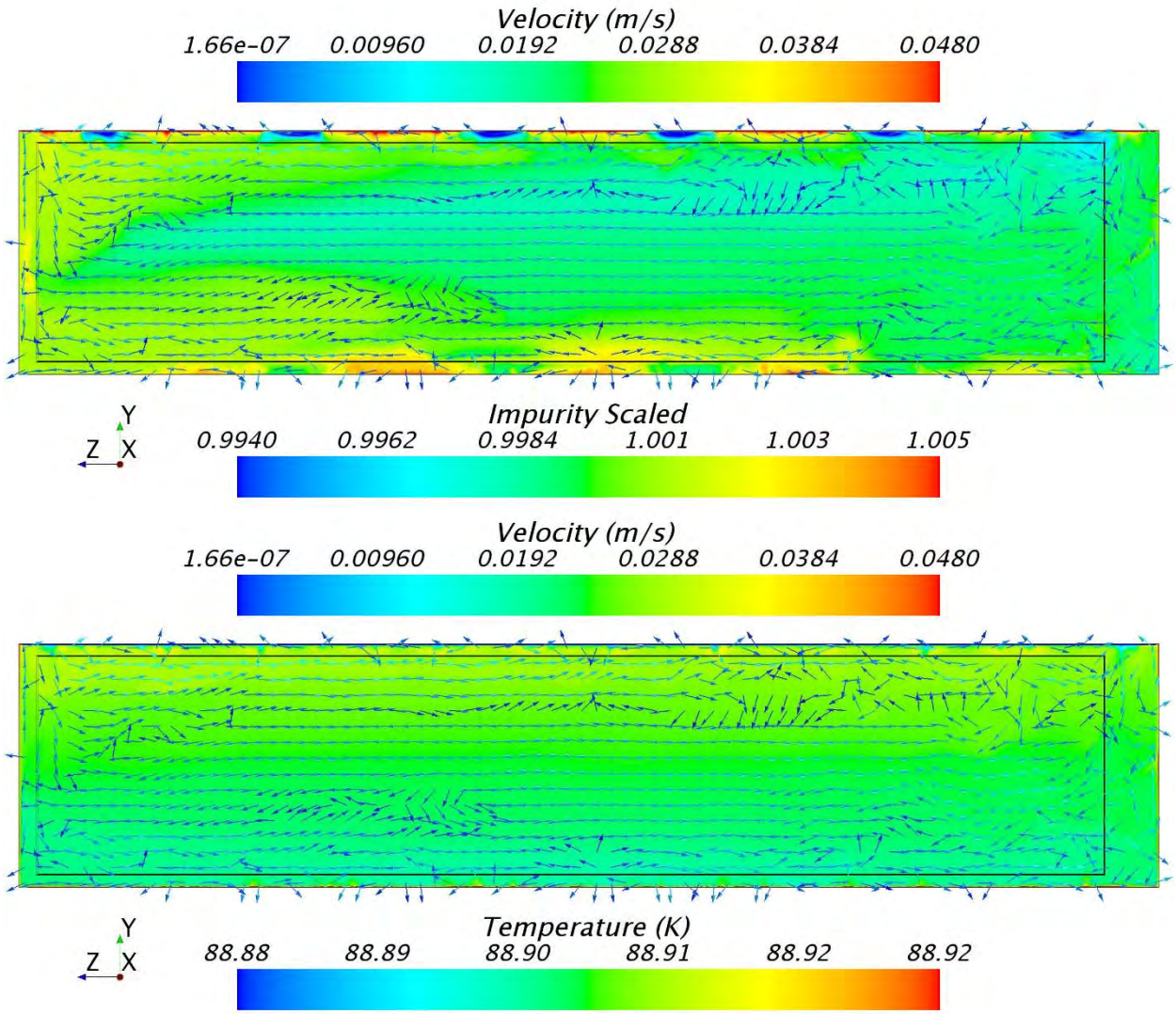

Figure 91. Impurity and temperature with velocity vectors at x = 4 m for latest design with 50% LAr flow rate (trimmed mesh).

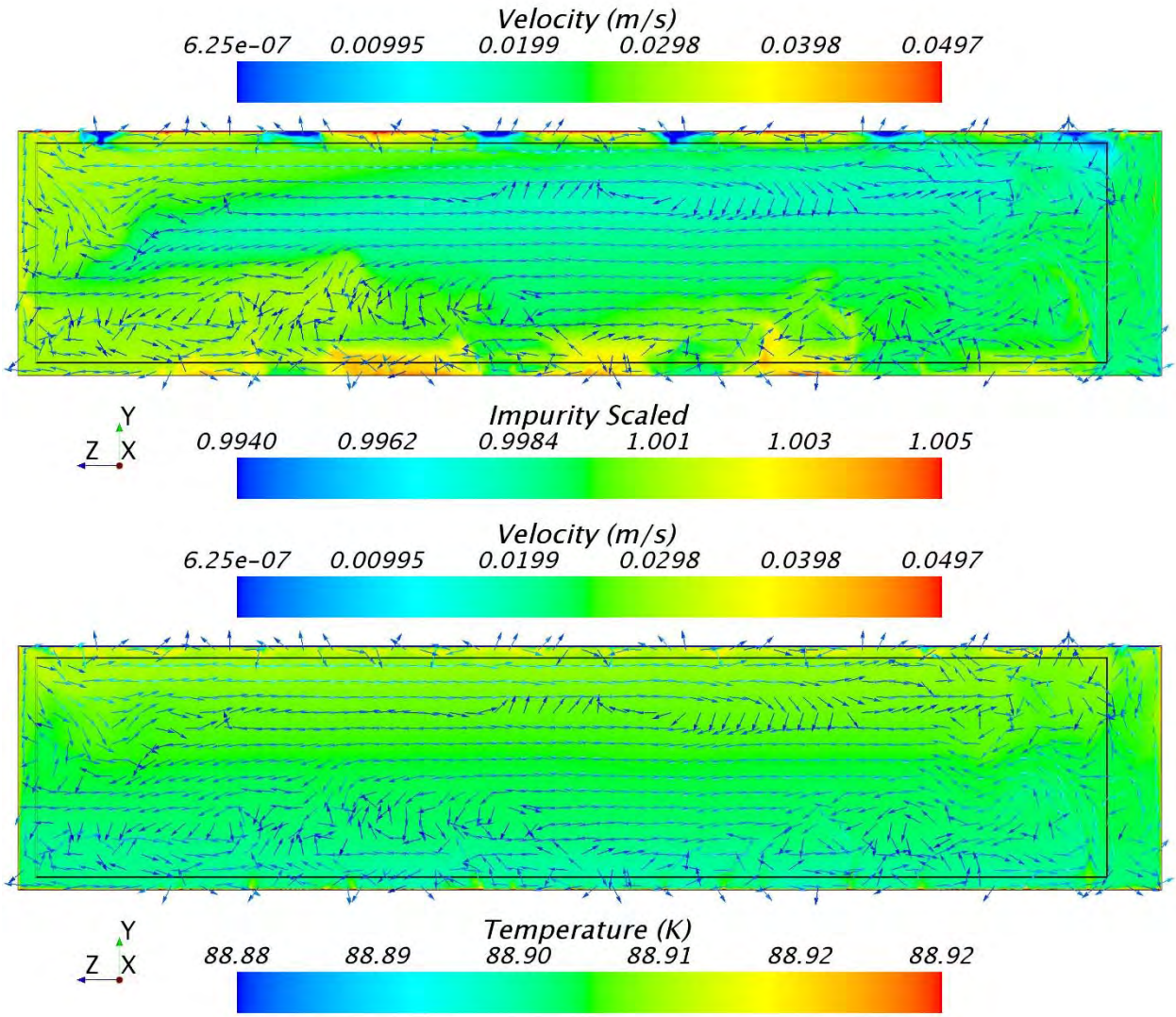

Figure 92. Impurity and temperature with velocity vectors at x = 5 m for latest design with 50% LAr flow rate (trimmed mesh).

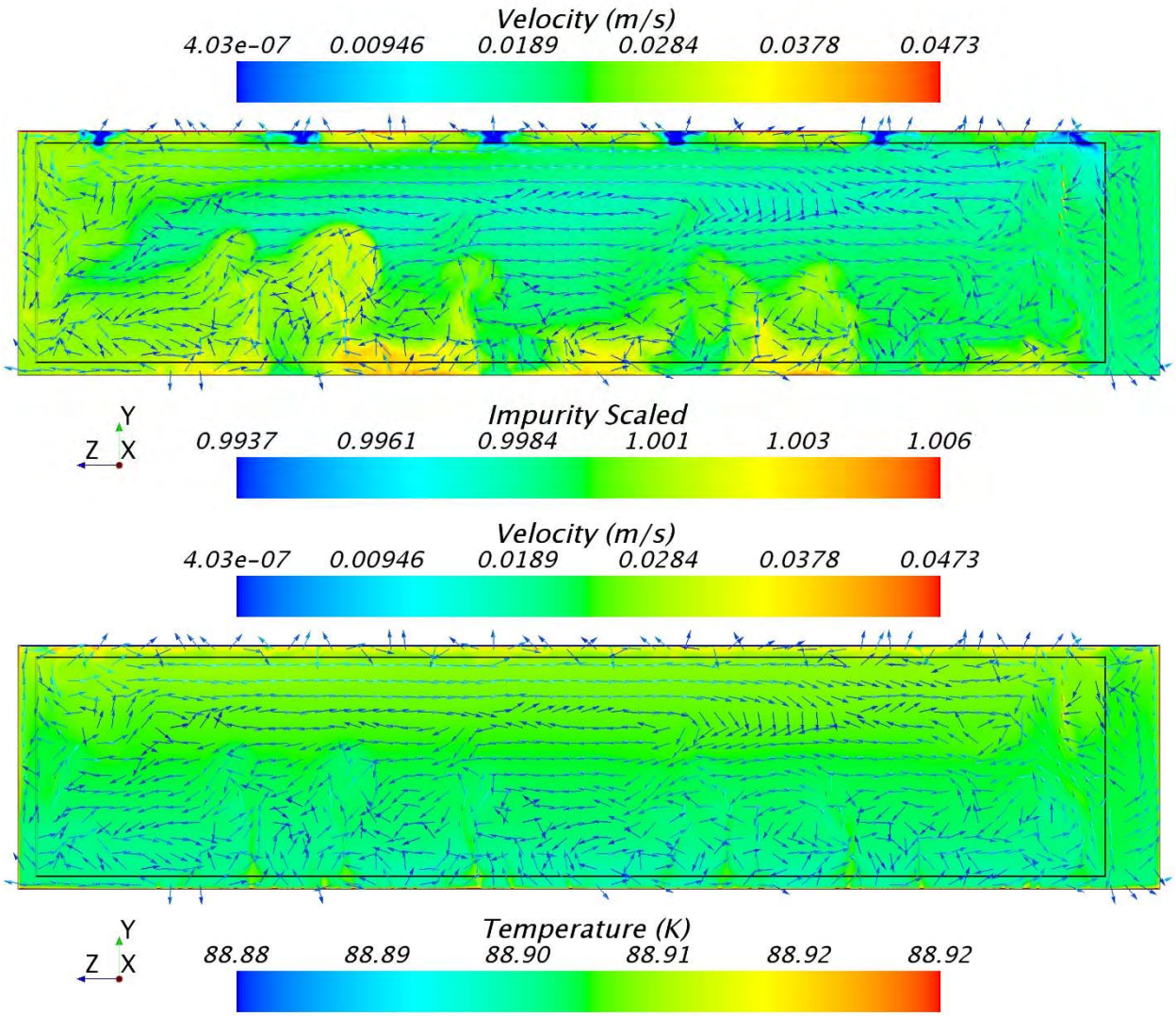

Figure 93. Impurity and temperature with velocity vectors at x = 6 m for latest design with 50% LAr flow rate (trimmed mesh).

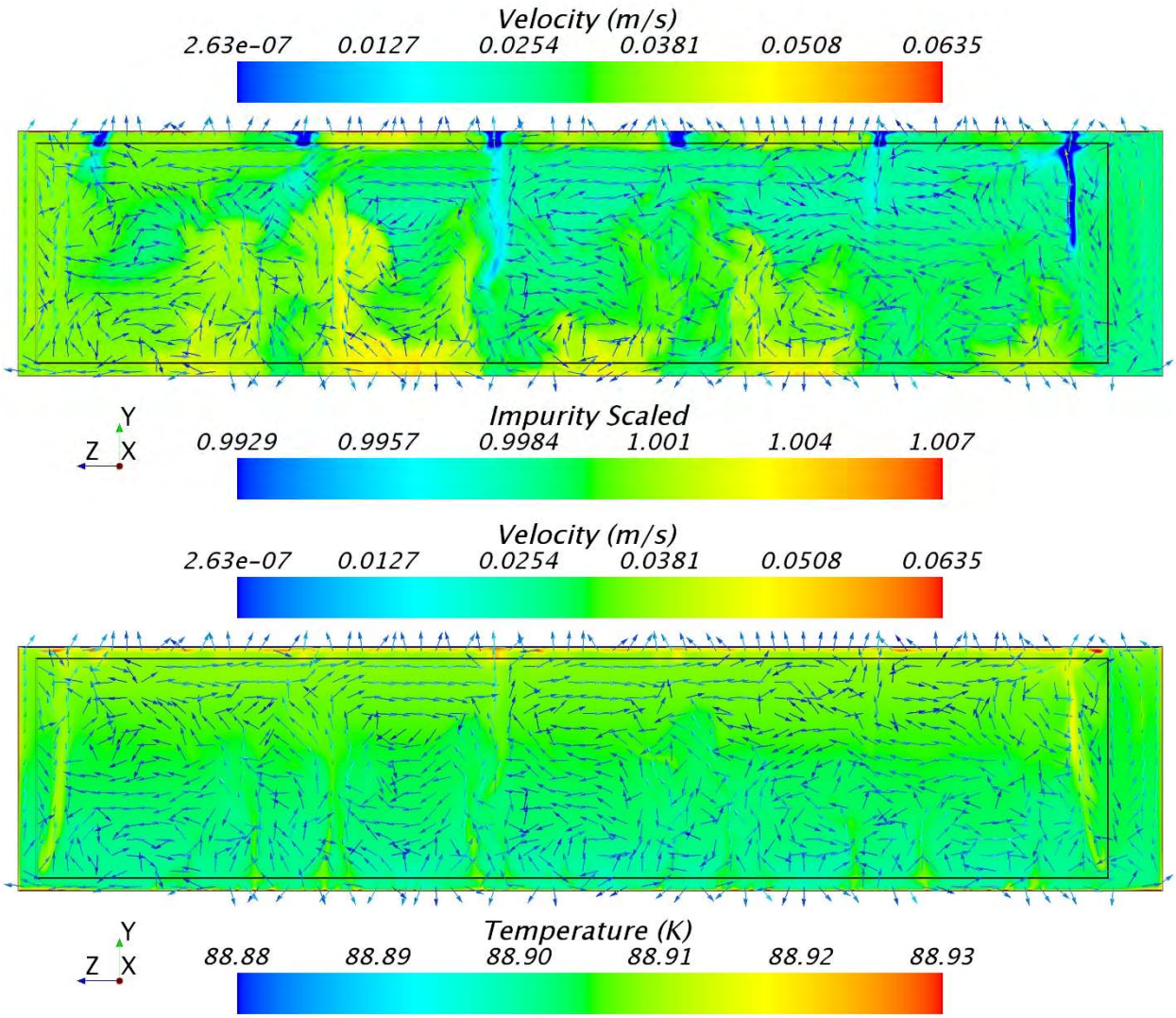

Figure 94. Impurity and temperature with velocity vectors at x = 7 m for latest design with 50% LAr flow rate (trimmed mesh).

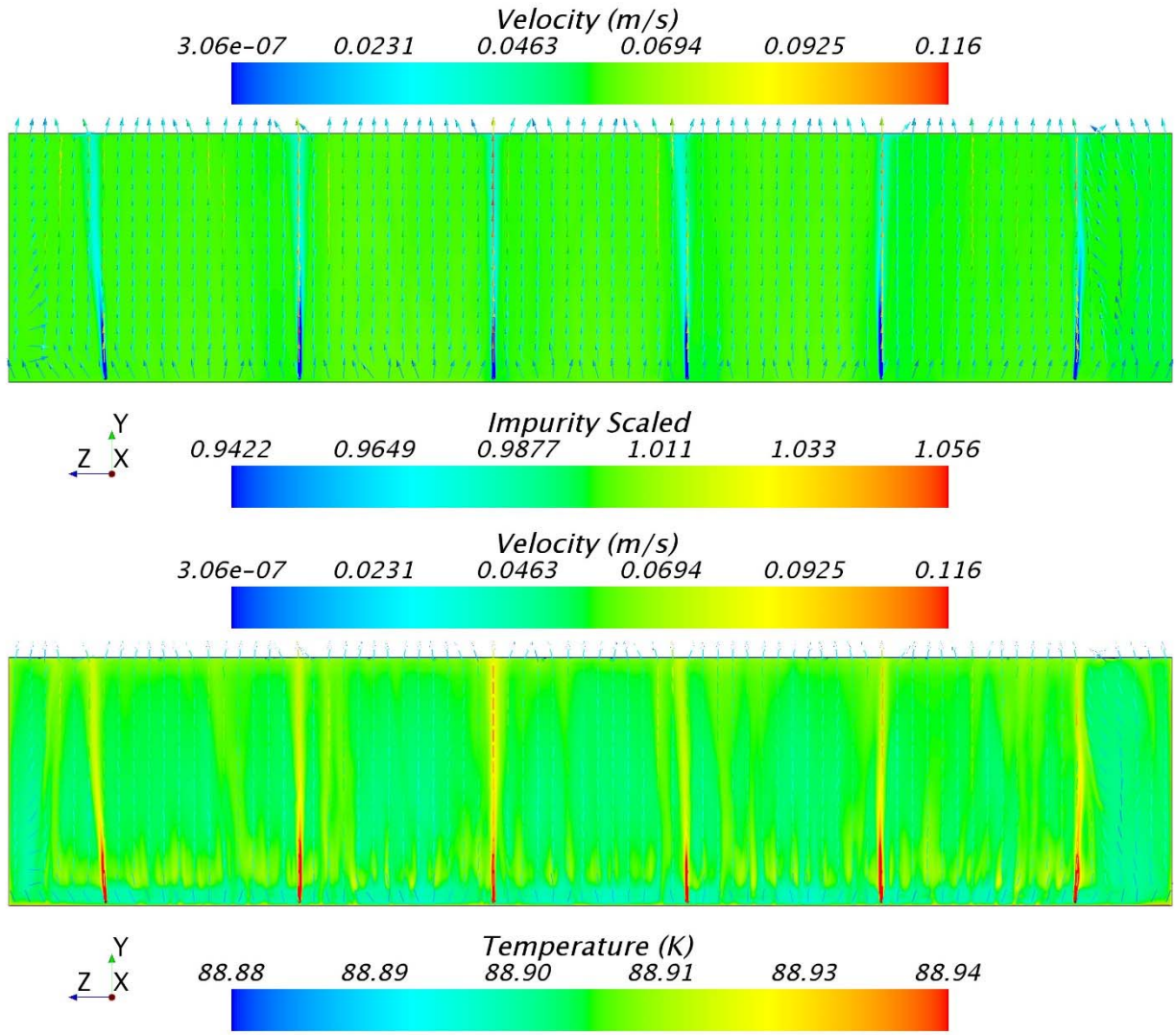

Figure 95. Impurity and temperature with velocity vectors at x = 7.4 m for latest design with 50% LAr flow rate (trimmed mesh).

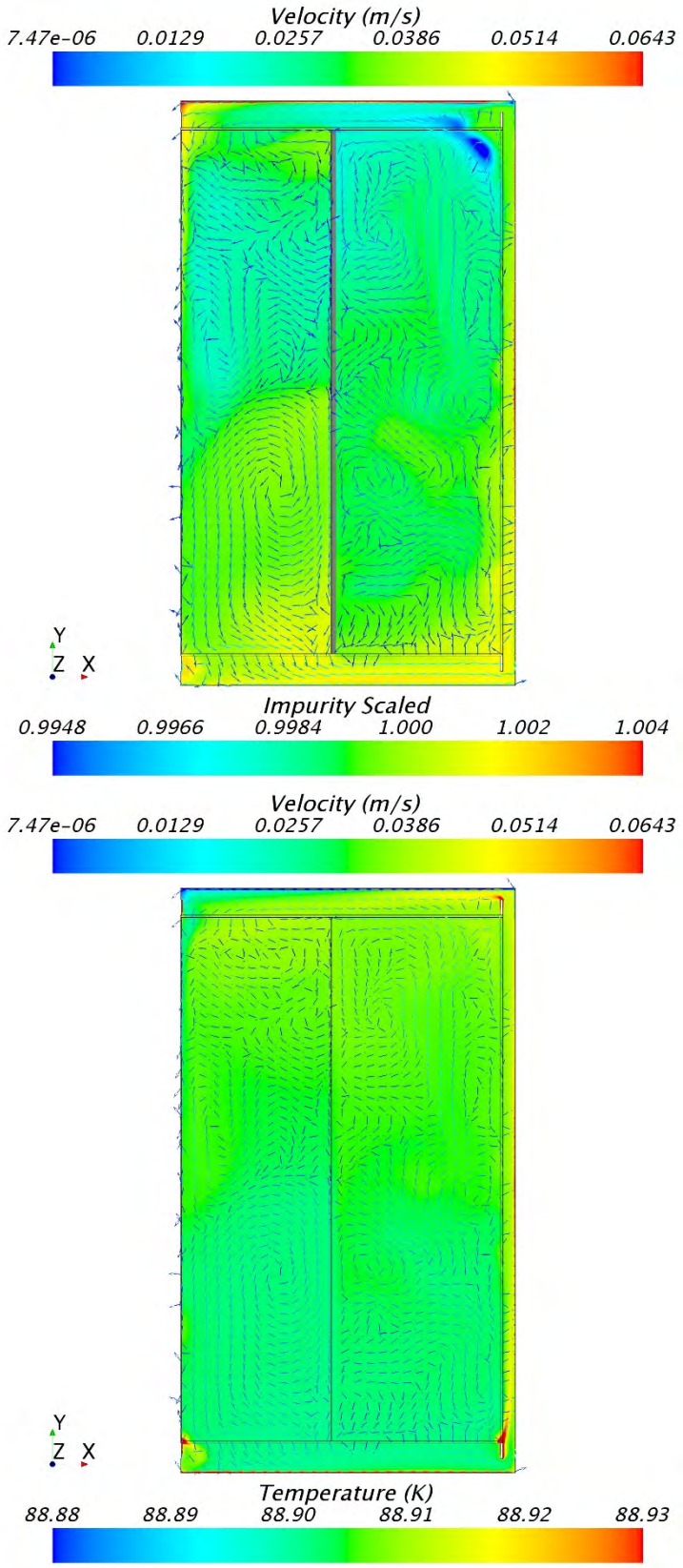

Figure 96. Impurity and temperature with velocity vectors at z = -25 m for latest design with 50% LAr flow rate (trimmed mesh).

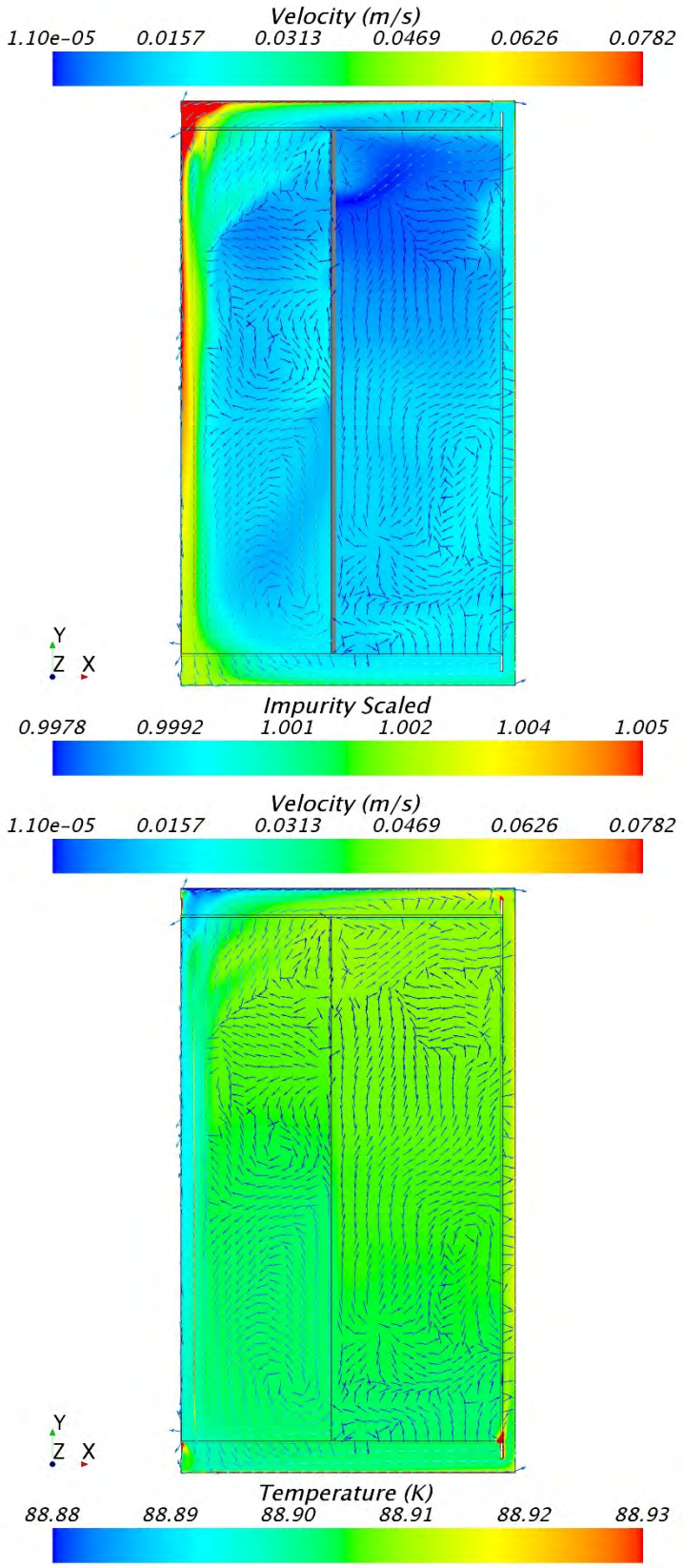

Figure 97. Impurity and temperature with velocity vectors at z = -20 m for latest design with 50% LAr flow rate (trimmed mesh).

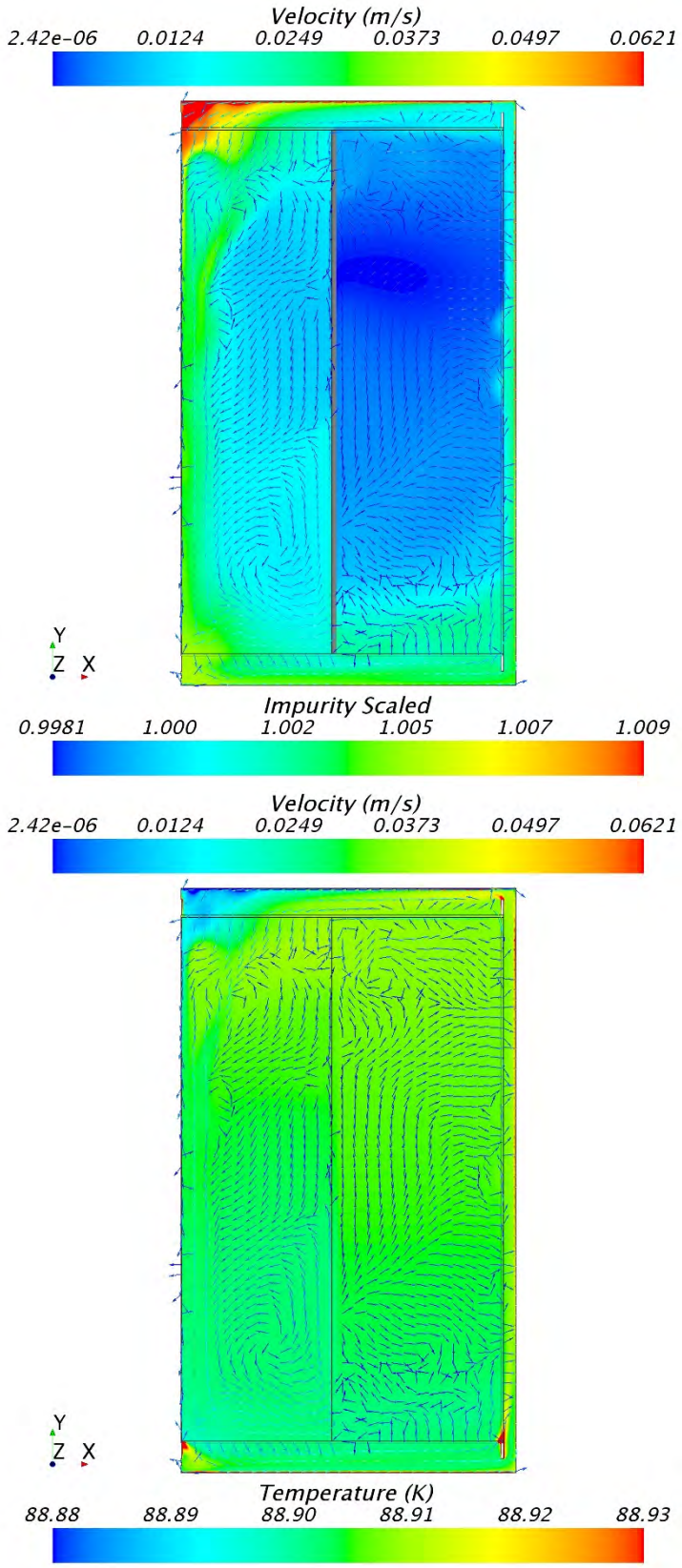

Figure 98. Impurity and temperature with velocity vectors at z = 0.0 m for latest design with 50% LAr flow rate (trimmed mesh).

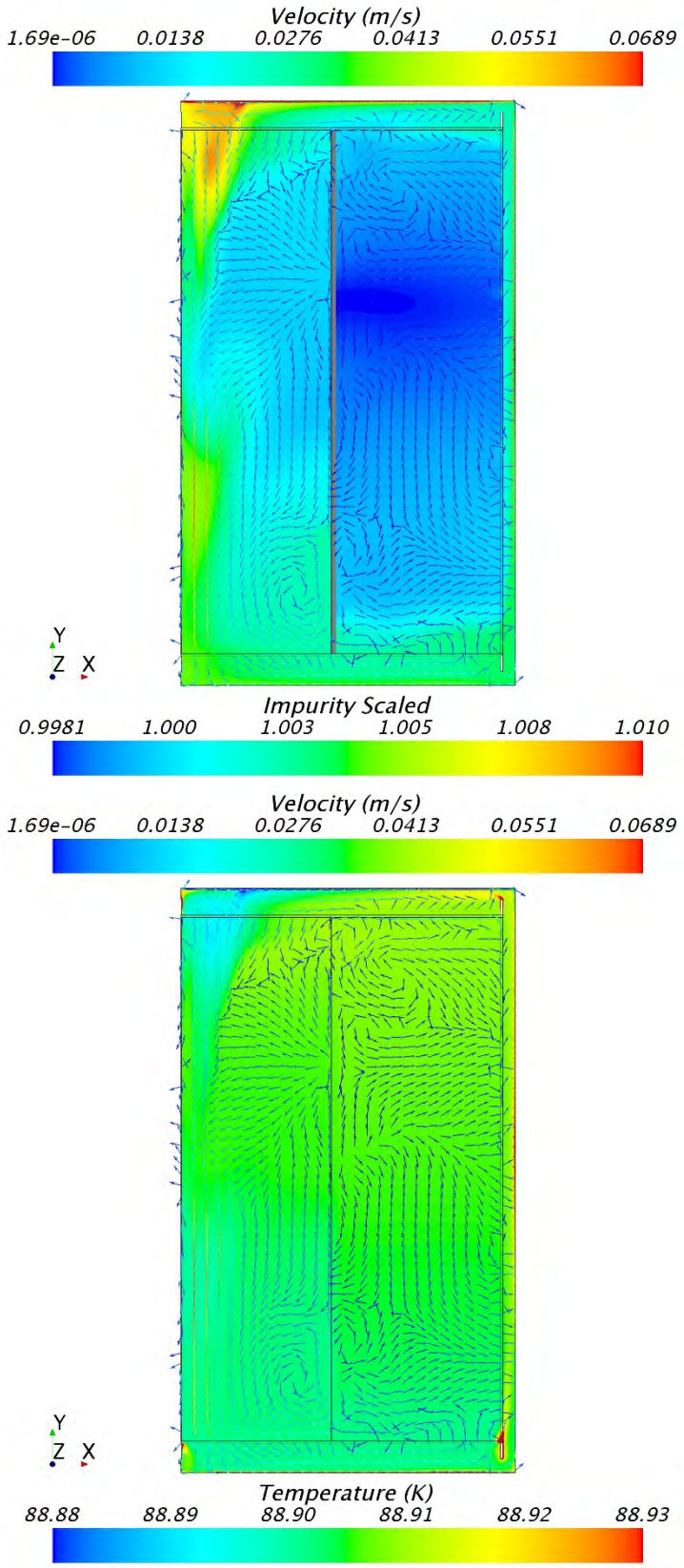

Figure 99. Impurity and temperature with velocity vectors at z = 10 m for latest design with 50% LAr flow rate (trimmed mesh).

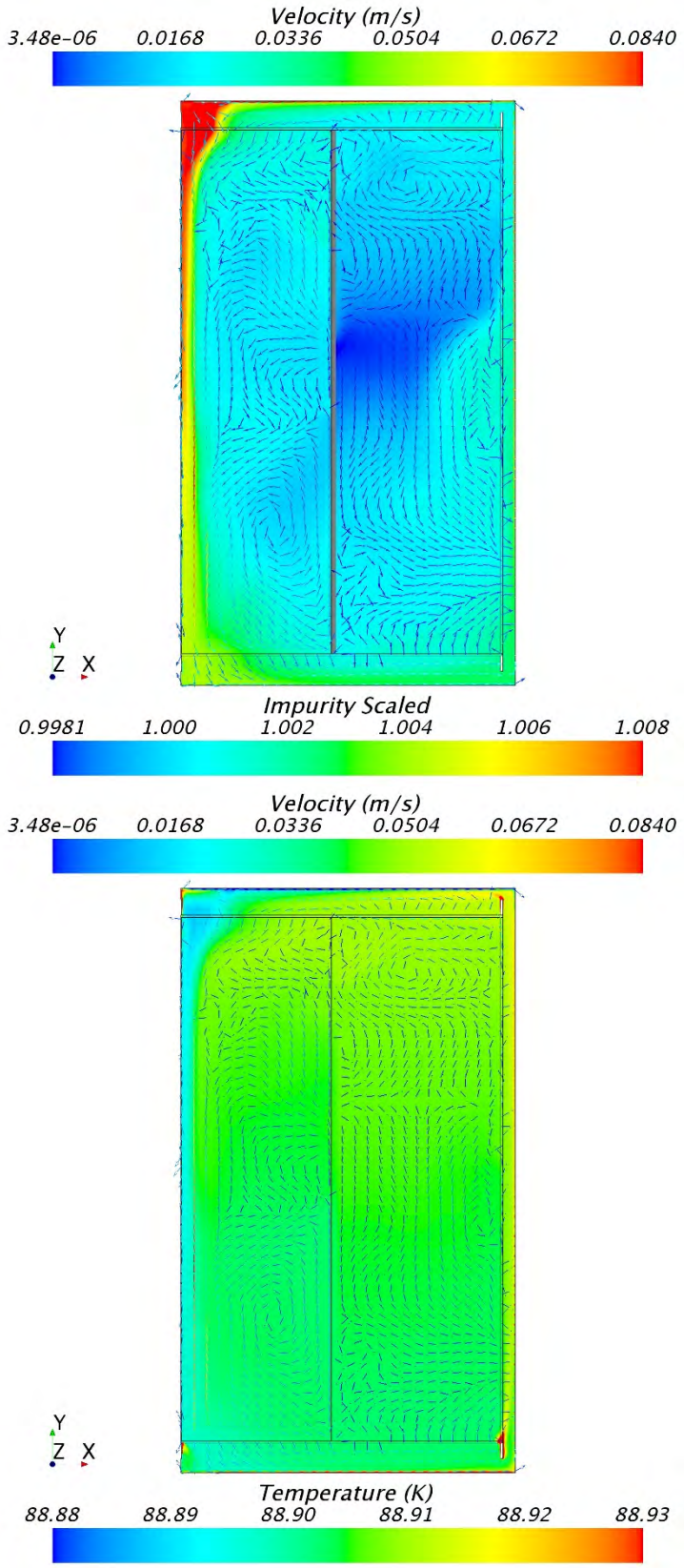

Figure 100. Impurity and temperature with velocity vectors at z = 20 m for latest design with 50% LAr flow rate (trimmed mesh).

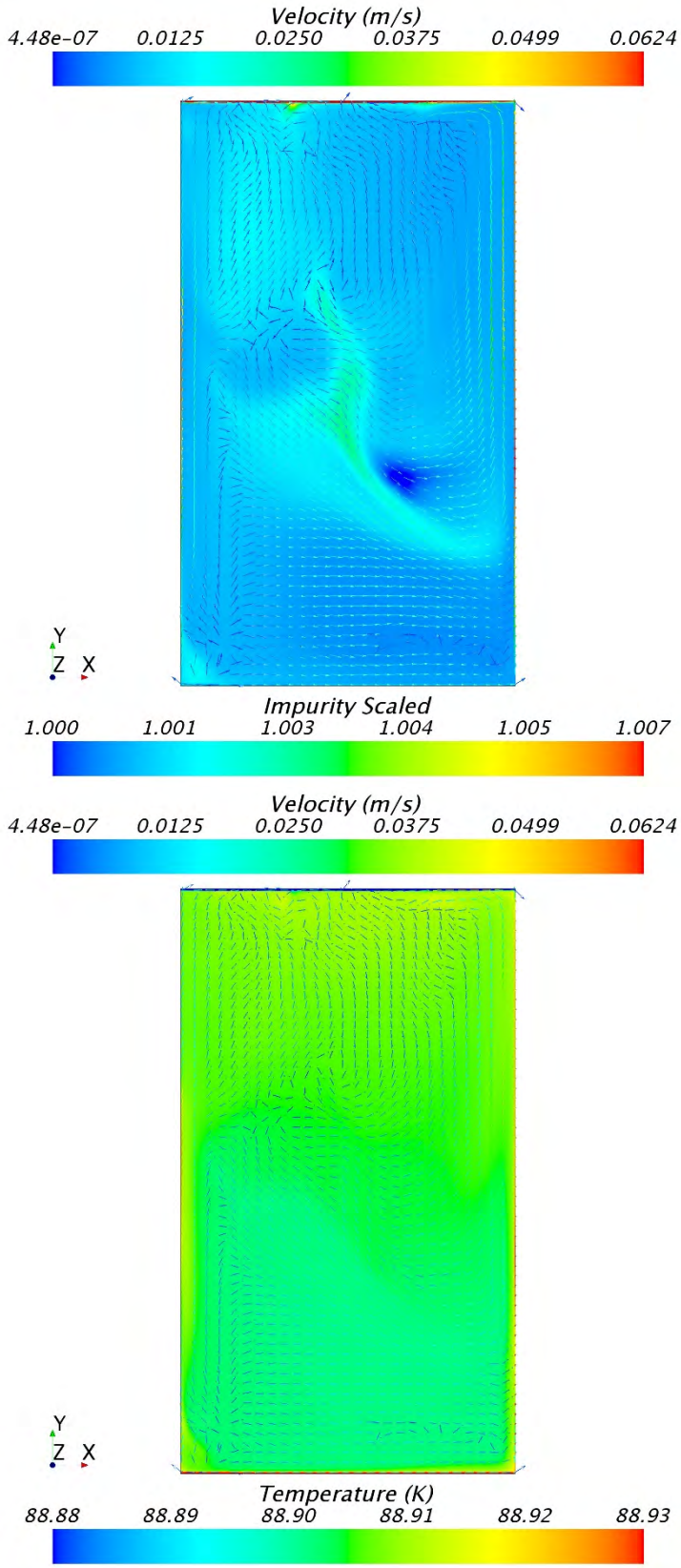

Figure 101. Impurity and temperature with velocity vectors at z = 30.5 m for latest design with 50% LAr flow rate (trimmed mesh).

Streamlines

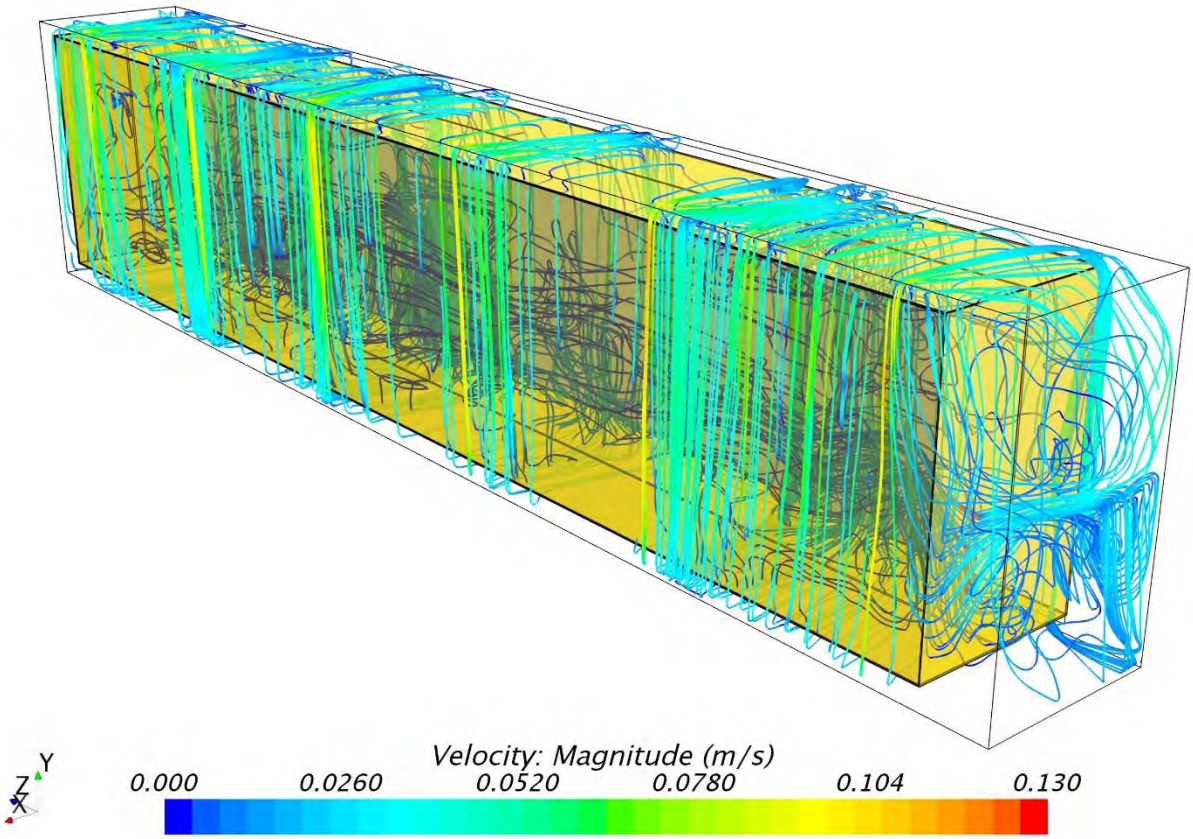

Figure 102. Streamline view 1 for latest design with half flow rate.

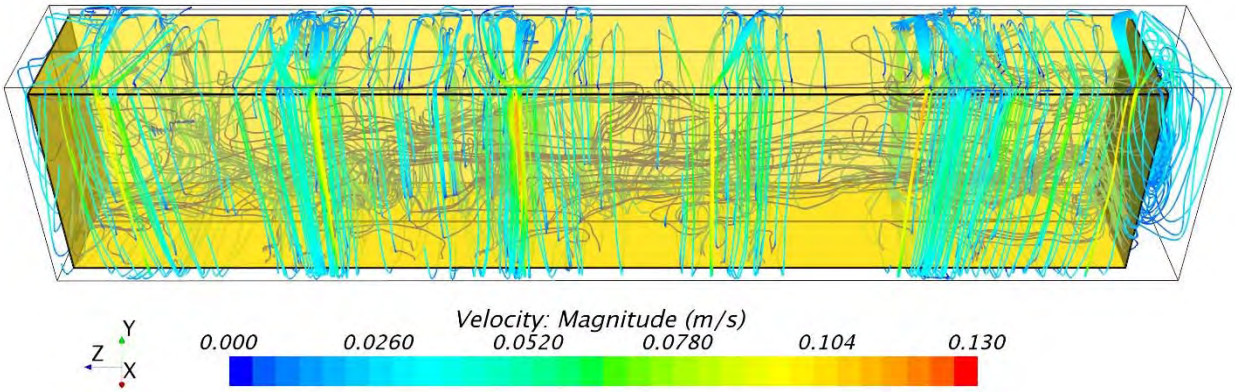

Figure 103. Streamline view 2 for latest design with half flow rate.

Impurity Level Statistics

Table 9. Impurity ranges for each mesh and operating condition.

	Poly	*New Poly*	*Trimmed*	*No Elec*	*Half Flow*
Max Value	2.13%	1.27%	1.27%	1.51%	0.75%
Min Value	-4.76%	-4.30%	-6.02%	-4.24%	-5.14%
Standard Dev.	1.41E-03	1.38E-03	1.74E-03	1.70E-03	1.06E-03

Table 10. Impurity ranges with half initial concentration for each mesh and operating condition.

	Poly	*New Poly*	*Trimmed*	*No Elec*	*Half Flow*
Max Value	2.06%	1.29%	1.28%	1.52%	N/A
Min Value	-3.86%	-4.30%	-6.02%	-4.24%	N/A
Standard Dev.	1.91E-03	1.37E-03	1.74E-03	1.70E-03	N/A

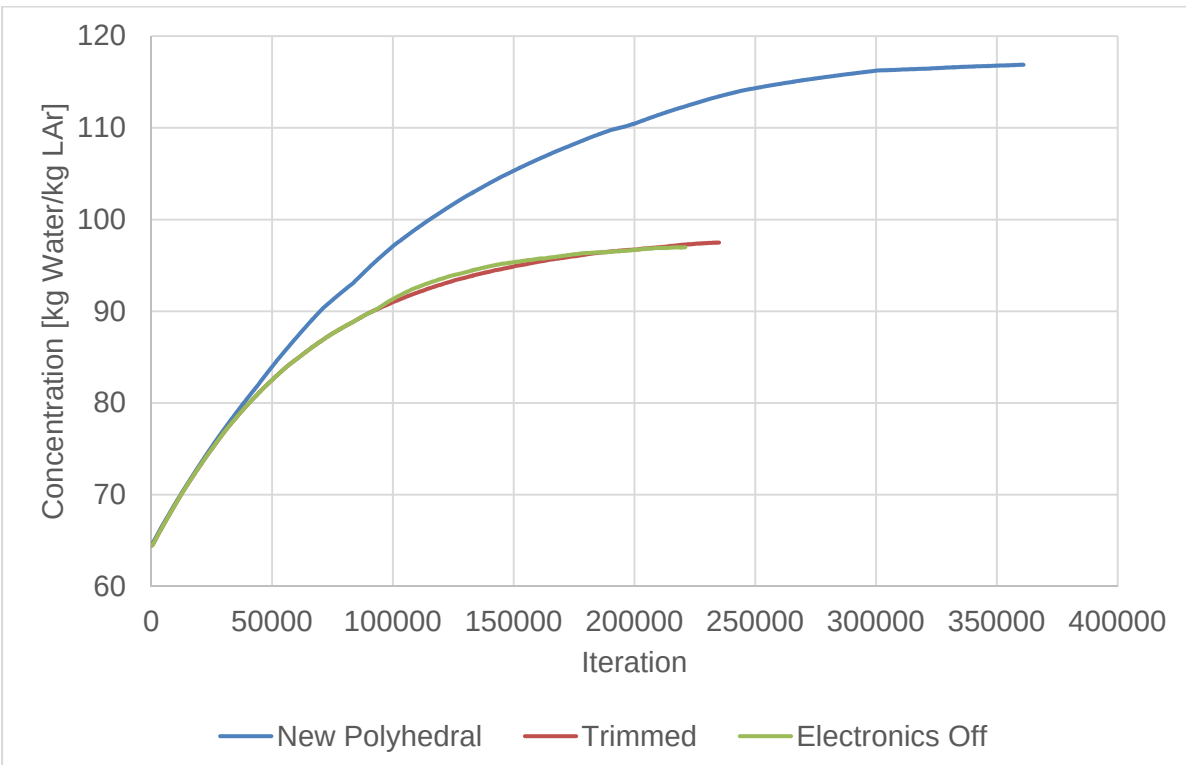

Figure 104. Average concentration at current solution.

Average Volume Temperature Comparison

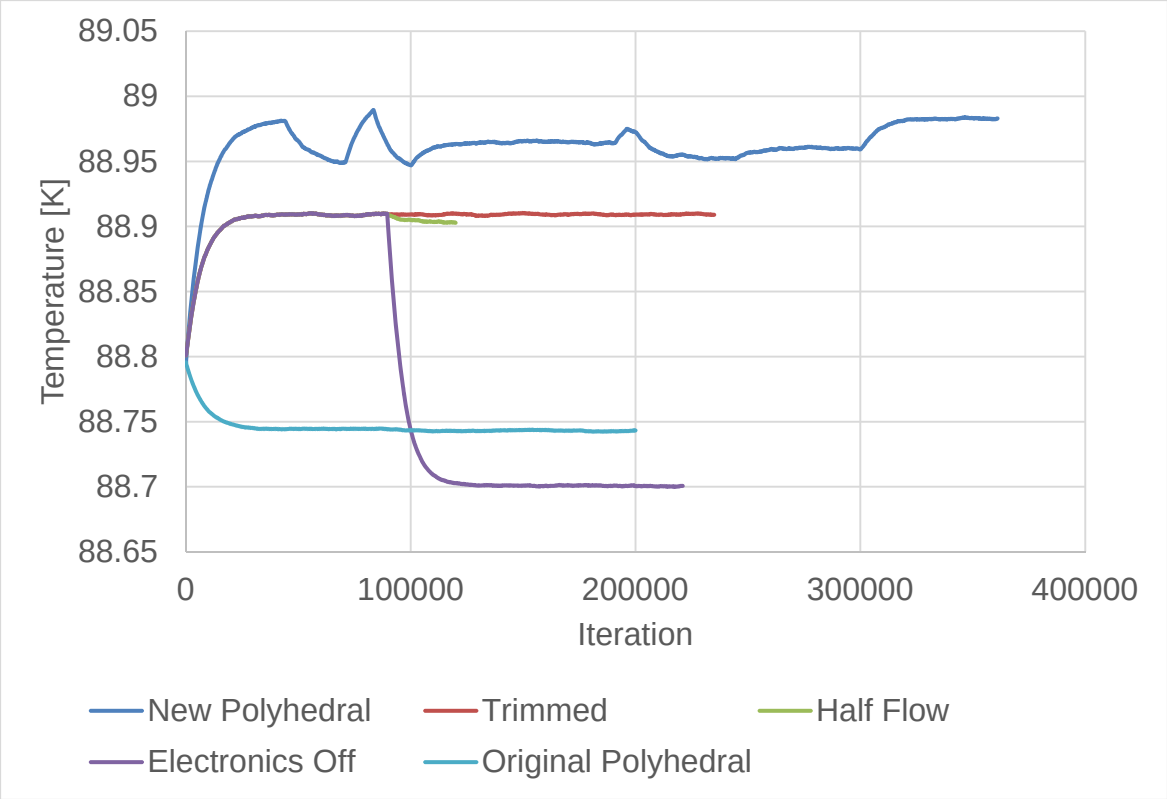

Figure 105. Plot of average volume temperature for each mesh and scenario.

REMARKS TO DATE

The South Dakota State University (SDSU) team has performed computational fluid dynamics studies to in an effort to validate and expand upon the work that has been done at the Fermi National Accelerator Laboratory (FNAL) by Erik Voirin in support of the Deep Underground Neutrino Experiment (DUNE). The primary goal of these simulations is to model the fluid, heat, and impurity flows in the 35 Ton and LBNF cryostats designs under consideration, as their performance is directly related to the purity distribution within the liquid argon. The flows being modeled are primarily buoyancy-driven, as the flow due to the heat flux through the cryostat walls drives the fluid motion to a much greater extent than the pumps that circulate fluid through the filters. The FNAL simulations have been performed using ANSYS CFX software, while the SDSU team is using Star-CCM+.

The APA planes and field cages have geometric features at scales that, if represented accurately in the computational model, would lead to unreasonably long computational times. For this reason, both the FNAL and SDSU teams have elected to represent them in the models as porous media. The properties of the porous media models have been selected such that the pressure drop for flows through the APA planes or field for a given velocity match those seen in a high fidelity model of the actual APA plane or field cage.

The SDSU team first modeled the 35 Ton cryostat, to determine best practices for simulating this type of buoyancy driven flow and to compare with available experimental and CFD data. The results obtained by the SDSU team agree with those of Erik Voirin at FNAL. The electron lifetime results also match the experimentally measured values obtained when the 35 Ton cryostat was operational. Once the original configuration of the 35 Ton cryostat had been simulated, an alternate configuration, with placement for the fluid inlet moved closer to the top liquid surface, was investigated. The concentration of impurities throughout the bulk of the cryostat was significantly reduced, and the uniformity of the impurity concentration was increased.

Next, the SDSU team created both a full model and a half model of the V1 flow arrangement (single inlet at one end, four outlets at other end) LBNF cryostat. The FNAL model that has been

used thus far is a half model of the LBNF cryostat, which assumes symmetry of the flow, temperature, and impurity distributions. Determining whether this is an appropriate assumption is important, since the half model significantly reduces computation time and allows for a greater parameter space to be investigated with the same computational resources. Except for a small region near the single inlet where the symmetric model predicts lower impurity concentration than the full model, very little difference in flow structures, temperatures, or impurity concentrations was seen between the two models. The continued use of the symmetry condition is therefore recommended.

The latest LBNF Cryostat design, which has a total of 12 pump discharge ports evenly spaced along the bottom corner of each side of the cryostat and a total of seven pump suction ports evenly spaced along the bottom centerline of the cryostat running lengthwise, provides a much more uniformly distributed impurity concentration over the V1 design, with a standard deviation of normalized impurity concentration an order of magnitude smaller.

REFERENCES

APPENDIX A

APPENDIX B